

# Important Notice

This copy may be used only for the purposes of research and private study, and any use of the copy for a purpose other than research or private study may require the authorization of the copyright owner of the work in question. Responsibility regarding questions of copyright that may arise in the use of this copy is assumed by the recipient.

UNIVERSITY OF CALGARY

A Multicomponent Seismic Investigation of Natural and Induced Fracturing,  
Saskatchewan, Canada

by

Edward Andrew Nicol

A THESIS

SUBMITTED TO THE FACULTY OF GRADUATE STUDIES  
IN PARTIAL FULFILMENT OF THE REQUIREMENTS FOR THE  
DEGREE OF MASTER OF SCIENCE

DEPARTMENT OF GEOSCIENCE

CALGARY, ALBERTA

APRIL, 2013

© Andrew Nicol 2013

## **Abstract**

Fractures in the subsurface are known to impact seismic imaging. This study focuses on multicomponent, time-lapse analysis of fracture-induced anisotropy in the Devonian Dawson Bay Formation in southern Saskatchewan. The baseline and monitor, PP and PS seismic volumes were divided into 4 sub-volumes consisting of a 45 degree stack of source-receiver ray paths.

Weak azimuthal anisotropy was observed through the interpretation of these volumes. Travel-time analysis located areas which are interpreted to exhibit a higher density of preferential fracturing which appears to be related to mining operations.  $V_p/V_s$  analysis, through the registration of PP and PS horizons, confirmed the presence of a high  $V_p/V_s$  anomaly which is interpreted to be caused by fractures networks without a preferential orientation within the Dawson Bay Formation in the centre of the survey area. Seismic attribute analysis was used to determine that fractures extend vertically from the Dawson Bay Formation to the top of the Souris River Formation.

## Acknowledgements

First, I would like to thank Dr. Don Lawton for giving me the opportunity to work on this project. Without his guidance, knowledge, patience and support over the last three years this thesis would not have been possible.

Thank you to the faculty and staff of the Consortium for Research in Elastic Wave Exploration Seismology (CREWES). Specifically, I would like to thank Dr. Larry Lines for his discussions about multicomponent seismology and his encouraging words throughout my research. Thank you to Laura Baird for her administrative support, ensuring that all deadlines were met and the annual CREWES conferences were well organized; to Kevin Hall for his technical support and sarcastic sense of humour which made the frustrations of printer malfunctions, software bugs and licensing problems more bearable; to Kevin Bertram for taking days to print off my research posters for presentation at the Geoconvention, SEG and CREWES annual conferences.

I would like to acknowledge the contributions of John Boyd, Ron Larson, Phillip Keith, and Sterling Hansen at RPS Boyd Petrosearch who provided the dataset and many useful discussions about local geology which aided with my interpretation. I am grateful to the CREWES Sponsors for their financial contributions to this research and to CREWES.

Thank you to my friends and colleagues at CREWES, many of whom started this adventure with me in September 2010: Steve Kim, Heather Lloyd, Chris Bird, Peter Gagliardi, Melissa Hernandez, Virginia Vera, thank you for your patience and support. Thank you to David Cho for his useful discussions surrounding seismic anisotropy, rock properties and fracture detection; to my officemates Jessie Arthur and Patricia Gavotti for sharing their experience, their insight, and for helping make finishing this dissertation more enjoyable.

I must also extend my deepest thanks to my teammates, colleagues and friends: Rachael Acker, Adam Fraser, Maureen Hill and Byron Kelly. You have all contributed more than you will ever know to my development as a geoscientist, and more importantly, as an individual.

Finally, and most importantly, my heartfelt thanks go to my Mom and Dad. You have supported me unconditionally in all of my endeavours over the years. Words cannot express how grateful I am to have you in my life.

*To my Mom and Dad, Ed and Irene Nicol, for without their love, patience, and support, I would not have the courage to follow my heart and chase my dreams.*

## Table of Contents

Abstract.....	ii
Acknowledgements.....	iii
Table of Contents.....	vi
List of Figures.....	viii
List of Symbols, Abbreviations and Nomenclature.....	xix
CHAPTER ONE: INTRODUCTION AND THEORY.....	1
1.1 Introduction.....	1
1.2 Geology.....	2
1.2.1 Stratigraphy and Depositional Setting.....	5
1.3 Seismic Anisotropy.....	8
1.3.1 Transverse Isotropy.....	10
1.3.1.1 Fracture Detection.....	11
1.4 Multicomponent Seismology.....	15
1.4.1 Converted Wave Seismology.....	22
1.5 Thesis Objectives.....	23
1.6 Summary of Software Used.....	24
CHAPTER TWO: TRAVEL-TIME ANALYSIS.....	27
2.1 Introduction.....	27
2.2 Horizon Interpretation.....	30
2.3 PP Travel-time Analysis.....	34
2.4 PS Travel-time Analysis.....	39
2.5 Summary.....	43
CHAPTER THREE: VELOCITY ANALYSIS.....	46
3.1 Introduction.....	46
3.2 Vp/Vs Analysis.....	46
3.3 Effect of Horizon Placement on Vp/Vs.....	61
3.4 Summary.....	63
CHAPTER FOUR: SEISMIC ATTRIBUTE ANALYSIS.....	68
4.1 Introduction.....	68
4.1.1 Complex Seismic Trace Analysis.....	69
4.1.2 Semblance Attribute.....	70
4.2 Seismic Attribute Interpretation.....	72
4.2.1 Baseline PP Seismic Attribute Analysis.....	72
4.2.2 Baseline PS Seismic Attribute Analysis.....	78
4.2.3 Time-Lapse Seismic Attribute Analysis.....	87
4.2.3.1 PP Seismic Attribute Analysis.....	87
4.2.3.2 PS Seismic Attribute Analysis.....	88
4.3 Summary.....	94
CHAPTER FIVE: DISCUSSION AND CONCLUSIONS.....	104
5.1 Discussion.....	104

5.2 Conclusions.....108

REFERENCES .....111

APPENDIX A: ADDITIONAL RESULTS FOR TRAVEL-TIME ANALYSIS .....121

APPENDIX B: ADDITIONAL RESULTS FOR SEISMIC ATTRIBUTE ANALYSIS124

    B.1. Monitor PP Seismic Attribute Interpretation .....124

    B.2. Time-Lapse PP Seismic Attribute Difference Analysis.....130

    B.3. Monitor PS Seismic Attribute Interpretation .....134

    B.4. Time-Lapse PS Seismic Attribute Difference Analysis.....135

## List of Figures

Figure 1.1 – Distribution of potash-bearing rocks in the Prairie Evaporite Formation. The highlighted region covers the extent of the Elk Point Embayment and the dashed line surrounds the area of potash bearing rocks. (from Fuzesy, 1982) .....	1
Figure 1.2 – Processing flow. ....	3
Figure 1.3 – Map showing the extent of the Elk Point Group through the Western Canada Sedimentary Basin (WCSB). (from Mossop & Shetsen, 1993).....	4
Figure 1.4 – A stratigraphic column showing the Devonian and Mississippian stratigraphy of interest for this study. (modified from Saskatchewan Ministry of Energy and Resources, 2011) .....	5
Figure 1.5 – Cartoon showing a VTI model of horizontally layered stratigraphy. (from Tsvankin, 1997) .....	12
Figure 1.6 – Cartoon showing a HTI model of vertically layered stratigraphy or an isotropic matrix with vertically oriented fractures. (from Tsvankin, 1997) .....	13
Figure 1.7 – S-wave polarization into a slow S-wave and a fast S-wave due to the presence of east-west oriented fractures. (modified from Crampin et al., 1989).....	17
Figure 1.8 – Larger time differences between P-S1 and P-S2 associated with anisotropy (hot colors) have a good correlation with three month total fluid production from wells. (from Sandanayake & Bale, 2011) .....	17
Figure 1.9 – Experimental results showing the relationship between S-wave slowness and porosity while under different levels of stress in dolomite. (from Pickett, 1963) .	18
Figure 1.10 – Comparison of reciprocal P- and S-wave velocities for different lithologies. The lines are indicative of specific $V_p/V_s$ values. (from Pickett, 1963) ...	20
Figure 1.11 – Velocity/porosity relationship. (from Gardner & Harris, 1968) .....	20
Figure 1.12 – Diagram showing a full multicomponent seismic wavefield propagating through a medium. For these three modes the direction of wave propagation is the same, but the particle displacement vectors are different. (modified from Sheriff, 2011) .....	21
Figure 1.13 – A P-wave shot record showing 4 major stratigraphic events, A through D (left). Converted wave shot record corresponding to the section in Figure 1.5 showing the seismic events A through D for the PS and SS modes (right). Note the travel time differences between the events for the different mode converted data. (from Fertig & Krajewski, 1989) .....	25

Figure 1.14 – A P-wave and PS wave reflection in a single homogeneous, isotropic layer. Note the converted wave reflects at its conversion point (CP) and the conventional P-wave reflects at a midpoint (MP). The arrows show direction of particle motion for each downgoing and upgoing wave mode. (from Stewart, 2002) .26

Figure 1.15 – The conversion point of a P-S reflection approaches the asymptotic conversion point (ACP), away from the receiver, as depth increases. The ACP is generally between the receiver and the midpoint (MP) of a conventional P-wave reflection profile. (from Stewart, 2002).....26

Figure 2.1 – Schematic diagram showing the fast and slow directions of seismic wave propagation with respect to fractures in the subsurface. The vertical fractures induce a reduction in seismic velocity perpendicular to the orientation of fracturing, whereas the seismic velocity parallel to fracturing is unchanged. ....28

Figure 2.2 – Distribution of source-receiver ray paths used to make up the four azimuthally sectorized seismic volumes. The volumes are labeled corresponding to the reciprocal azimuths in the middle of the stacked aperture.....29

Figure 2.3 – Residual NMO from the sectorized receiver gathers and stacks corresponding to the directions of fast (green) and slow (red) seismic wave propagation, as well as the travel-times associated with those azimuthally sectorized stacks.....30

Figure 2.4 - Blocked wireline logs acquired from one of the wells in the study area. The P-wave sonic is in blue, S-wave sonic in red and Vp/Vs calculated from both sonic logs in magenta. The geological tops are in black. ....31

Figure 2.5 – PP synthetic seismogram (blue seismic traces) constructed using the P-wave sonic (blue log) and is correlated with the baseline PP seismic volume (red/black seismic traces).....32

Figure 2.6 – PS synthetic seismogram (blue seismic traces) constructed using the P-wave sonic (blue log), the S-wave sonic (red log) and the Vp/Vs (magenta log) is used to apply a velocity stretch before the synthetic is tied with the baseline PS seismic volume (red/black seismic traces).....33

Figure 2.7 – Time structure maps showing the Winnipegosis Formation from the baseline PP seismic volume (left) and baseline PS seismic volume (right). The large blue-purple anomaly in the centre of the map shows a travel-time “push down” which is thought to be attributed to the presence of fractures in the carbonate layers above the Prairie Evaporite Formation. The red circle in the Northeast corresponds with an interpreted pinnacle reef, and the yellow-red in the Southeast shows the outline of an interpreted carbonate mound. ....34

Figure 2.8 – An inline and crossline from the baseline PP volume displaying the low amplitude, low velocity anomaly at the centre of the study area (red circle). The

anomaly propagates below the Souris River Formation to the bottom of the section. ....	35
Figure 2.9 – Chair display showing an inline through the baseline PP volume (right) and the baseline PS volume (left). This figure emphasizes the travel-time differences between the PP and PS volumes, as well as the lower frequency content and higher noise levels in the PS volume. ....	36
Figure 2.10 – PP time difference plots for the Souris River Formation calculated by subtracting the A-C azimuths for the baseline (left) and monitor (right) seismic volumes. ....	36
Figure 2.11 – PP time difference plots, for the Souris River Formation, calculated by subtracting the B-D azimuths for the baseline (left) and monitor (right) seismic volumes. ....	37
Figure 2.12 – The baseline (left) and monitor (right) A-C azimuth PP time difference plots for the Prairie Evaporite Formation, showing mine workings in the southeast corner of the map (black ellipses). ....	38
Figure 2.13 – The baseline (left) and monitor (right) B-D azimuth PP time difference plots for the Prairie Evaporite Formation. ....	38
Figure 2.14 – The baseline (left) and monitor (right) A-C azimuth PP time difference plots for the Winnipegosis Formation. ....	39
Figure 2.15 – The baseline (left) and monitor (right) B-D azimuth PP time difference plots for the Winnipegosis Formation. ....	40
Figure 2.16 – The baseline (left) and monitor (right) A-C azimuth PS time difference plots for the Souris River Formation. ....	40
Figure 2.17 – The baseline (left) and monitor (right) B-D azimuth PS time difference plots for the Souris River Formation. ....	41
Figure 2.18 – The baseline (left) and monitor (right) A-C azimuth PS time difference plots for the Prairie Evaporite Formation. The black circle indicates a large negative travel-time difference in the monitor volume, not present in the baseline. ....	42
Figure 2.19 – The baseline (left) and monitor (right) B-D azimuth PS time difference plots for the Prairie Evaporite Formation. The black circle indicates a large negative travel-time difference in the monitor volume, not present in the baseline. ....	42
Figure 2.20 – The baseline (left) and monitor (right) A-C azimuth PS time difference plots for the Winnipegosis Formation. ....	43
Figure 2.21 – The baseline (left) and monitor (right) B-D azimuth PS time difference plots for the Winnipegosis Formation. ....	44

Figure 3.1 – Crossline showing five major horizons picked in the PP (left) and PS (right) seismic volumes through the low velocity, low amplitude anomaly in the centre of the dataset. The PS volume is compressed using a Vp/Vs of 2.0 to best match the placement of each horizon with their PP counterpart. ....47

Figure 3.2 – Crossline from the baseline seismic volume through one of the wells containing a dipole sonic log. Vp/Vs, shown in color, is set to the background Vp/Vs of 2.0 determined from the registration process. The horizons from top to bottom are the Birdbear Formation (yellow), Souris River Formation (green), Prairie Evaporite Formation (red) and Winnipegosis Formation (blue). ....48

Figure 3.3 – Crossline from the baseline seismic volume through a well with dipole sonic log. The Birdbear PP and PS horizon matching has been applied generating the high Vp/Vs at the top of the section. This increased Vp/Vs at the top of the section is due to the high Vp/Vs of the overburden. ....49

Figure 3.4 – Crossline from the baseline volume showing a line through a well with dipole sonic log (upper) and a line through the low velocity, low amplitude anomaly in the centre of the dataset (lower). Notice the higher average Vp/Vs in the Birdbear interval on the line outside of the seismic anomaly. The top of the Birdbear Formation is the yellow horizon, the Souris River Formation is green, the Prairie Evaporite Formation is red and the Winnipegosis Formation is blue. ....51

Figure 3.5 – Crossline from the baseline volume showing a line through a well with dipole sonic log (upper) and a line through the low velocity, low amplitude anomaly in the centre of the dataset (lower). Notice the higher average Vp/Vs in the Souris River interval on the line in the seismic anomaly. The top of the Birdbear Formation is the yellow horizon, the Souris River Formation is green, the Prairie Evaporite Formation is red and the Winnipegosis Formation is blue. ....52

Figure 3.6 – Crossline from the baseline volume showing a line through a well with dipole sonic log (upper) and a line through the low velocity, low amplitude anomaly in the centre of the dataset (lower). Notice the higher average Vp/Vs in the Prairie Evaporite interval on the line in the seismic anomaly. The top of the Birdbear Formation is the yellow horizon, the Souris River Formation is green, the Prairie Evaporite Formation is red and the Winnipegosis Formation is blue. ....53

Figure 3.7 – Crossline from the baseline volume which goes through a well with dipole sonic, where Vp/Vs log has been calculated (log on cross section). There is a significant increase in Vp/Vs at the bottom of the Souris River Formation (green horizon) within the Dawson Bay Formation when the well control is incorporated into the horizon matching process (purple on the east end of the line). The Vp/Vs increases from 2.0 to 2.5, an increase interpreted to be the result of fracturing in the lower regions of the Dawson Bay Formation, just above the top of the Prairie Evaporite Formation (red horizon). ....54

Figure 3.8 – Crossline from the baseline volume which goes through low velocity, low amplitude seismic anomaly in the centre of the volume. There is a significant

increase in  $V_p/V_s$  at the bottom of the Souris River Formation (green horizon) within the Dawson Bay Formation when the well control is incorporated into the horizon matching process (purple above the red horizon). The  $V_p/V_s$  increases from 2.0 to 2.5, an increase interpreted to be the result of fracturing in the lower regions of the Dawson Bay Formation, just above the top of the Prairie Evaporite Formation (red horizon). The increased thickness of the fractured area through the centre of the section is interpreted to be an increase in the extent of vertical fracturing. ....55

Figure 3.9 - Crossline from the monitor volume showing a line through a well with dipole sonic log (upper) and a line through the low velocity, low amplitude anomaly in the centre of the dataset (lower). Notice that in general the crossline through the seismic anomaly in the centre of the dataset (lower) has a higher  $V_p/V_s$  than the line outside of the anomaly, specifically in the Souris River and Prairie Evaporite intervals. The Birdbear Formation has a lower  $V_p/V_s$  in the area of the seismic anomaly. These trends are unchained from the baseline to the monitor surveys. The top of the Birdbear Formation is the yellow horizon, the Souris River Formation is green, the Prairie Evaporite Formation is red and the Winnipegosis Formation is blue. ....56

Figure 3.10 - Crossline from the monitor volume, through a well with dipole sonic, where  $V_p/V_s$  log has been calculated (log on cross section). There is a significant increase in  $V_p/V_s$  at the bottom of the Souris River Formation (green horizon) within the Dawson Bay Formation when the well control is incorporated into the horizon matching process (purple on the east end of the line). The  $V_p/V_s$  increases from 2.0 to 2.5, an increase interpreted to be the result of fracturing in the lower regions of the Dawson Bay Formation, just above the top of the Prairie Evaporite Formation (red horizon). ....57

Figure 3.11 - Crossline from the monitor volume which goes through low velocity, low amplitude seismic anomaly in the centre of the seismic volume. There is a significant increase in  $V_p/V_s$  at the bottom of the Souris River interval (green horizon) within the Dawson Bay Formation when the well control is incorporated into the horizon matching process (purple above the red horizon). The  $V_p/V_s$  increases from 2.0 to 2.5, an increase interpreted to be the result of fracturing in the lower regions of the Dawson Bay Formation, just above the top of the Prairie Evaporite Formation (red horizon). The increased thickness of the fractured area through the centre of the section is interpreted to be an increase in vertical extent of fracturing. ....58

Figure 3.12 – Interval  $V_p/V_s$  for the baseline (left) and monitor (right) from the Birdbear to Souris River formations. ....59

Figure 3.13 – Interval  $V_p/V_s$  for the baseline (left) and monitor (right) from the Souris River to Prairie Evaporite formations. ....59

Figure 3.14 – Interval Vp/Vs for the baseline (left) and monitor (right) surveys from the Prairie Evaporite to Winnipegosis formations. The black circles show an area of significant increase in Vp/Vs between surveys, and the black rectangle shows the location of a carbonate reef structure in the Winnipegosis Formation. ....	60
Figure 3.15 – Seismic crossline showing the difference in frequency content between the PP (left) and PS (right) volumes for intervals of identical thickness. The frequency spectrum associated with each interval is directly below the seismic section. ....	62
Figure 3.16 – PP synthetic seismogram (blue seismic trace) tied to the 2004 full azimuth stack PP seismic volume (red and black seismic). The logs on the left are the P-sonic (blue), S-sonic (red) and calculated Vp/Vs (pink). ....	64
Figure 3.17 – PS synthetic seismogram (blue seismic trace) tied to the 2004 full azimuth stack PS seismic volume (red and black seismic). The logs on the left are the P-sonic (blue), S-sonic (red) and calculated Vp/Vs (pink). ....	64
Figure 3.18 – Crossline through the well (same as Figure 3.7) which shows the difference in Vp/Vs in the Birdbear – Souris River and Souris River – Prairie Evaporite intervals for the baseline seismic volume A. This difference is due to the time shift (-38 ms) applied to the Souris River horizon from the PS volume, orientation A. ....	65
Figure 3.19 – Crossline through the well (same as Figure 3.7) with an adjusted time shift (-45 ms) applied to the Souris River Formation of the baseline A PP and PS seismic volumes. ....	66
Figure 3.20 – Comparison between the interval Vp/Vs from the Birdbear Formation to Souris River Formation for the seismic volumes of orientation A. On the left, the same time shift is applied to the Souris River Formation as was in the full azimuth volume (-38 ms). On the right, a reassessed time shift of -45 ms is applied in order to better position the horizon on the seismic section. ....	66
Figure 3.21 – Comparison between the interval Vp/Vs from the Souris River Formation to the Prairie Evaporite Formation for the seismic volumes of orientation A. On the left, the same time shift is applied to the Souris River Formation as was in the full azimuth volume. On the right, a reassessed time shift of -45 ms is applied in order to better position the horizon on the seismic section. ....	67
Figure 4.1 – (a) A time-slice through a PP seismic volume in which many of the faults in the coherence time-slice (b) at the same level are difficult to see. (from Bahorich & Farmer, 1995).....	71
Figure 4.2 – Baseline PP semblance (a) and amplitude envelope (b) time slice through the top of the Souris River Formation (710 ms). The eastern edge of the survey shows a lower semblance value (red box) than the western edge. The lowest	

amplitude envelope values on the eastern edge of the survey correspond to low semblance values in the corresponding semblance slice. ....	74
Figure 4.3 – Baseline PP semblance (a) and amplitude envelope (b) time slices through the middle of the Souris River Formation (720 ms). In general the semblance is high across the slice except in the centre of the volume where a low semblance anomaly exists. This anomaly corresponds to the high Vp/Vs anomaly described in Figure 3.14. The lowest amplitude envelope values, found in the centre of the dataset, correspond directly to the area of low semblance from Figure 4.2. ....	76
Figure 4.4 - Baseline PP semblance (a) and amplitude envelope (b) time slices just above the top of the Dawson Bay Formation (748 ms). The semblance time slice shows two anomalies with relatively low semblance: one in the centre of the dataset where a low amplitude, low velocity anomaly with high Vp/Vs is located and another where a carbonate mound is interpreted to be located in the Winnipegosis Formation below. The amplitude envelope time slice (b) shows amplitudes between 1.0 and 1.5 throughout the slice except around the edges of the survey area and where the low semblance anomalies are located. ....	77
Figure 4.5 – Baseline PP semblance (a) and amplitude envelope (b) time slices through the top of the Prairie Evaporite Formation (774 ms) show the same correlation between low semblance and low amplitude envelope values. There is a low semblance area which surrounds the area interpreted to contain randomly oriented fractures seen in Figure 4.3 and Figure 4.4.....	79
Figure 4.6 - Baseline PP semblance (a) and amplitude envelope (b) time slices through the Prairie Evaporite Formation (792 ms) clearly show the mine rooms. In the centre of the slice through the amplitude envelope volume, there is a low value anomaly which is significantly lower than that of the rest of the area. This anomaly has been interpreted to be the result of subsurface fracturing which does not have a preferential orientation.....	80
Figure 4.7 - Baseline PP semblance (a) and amplitude envelope (b) time slices through the Prairie Evaporite Formation (836 ms) shows two carbonate reefs (red circles) on the eastern side of the survey. The slice through the amplitude envelope volume (b) outlines a carbonate mound (green box) with amplitudes between 1.0 and 2.5. The western side of the survey, to the west of the carbonate mound, has a lower average amplitude envelope value between 0.0 and 0.5.....	82
Figure 4.8 - Baseline PP semblance (a) and amplitude envelope (b) time slices through the top of the Winnipegosis Formation (848 ms) shows the outline of one of the reefs from the slices in Figure 4.7 (red circle). There is no correlation between amplitude envelope and semblance at this level, but the semblance time slice (a) still shows the outline of the low amplitude, low velocity anomaly in the centre of the dataset (triangle) and the outline of the carbonate mound feature (green box). ....	83
Figure 4.9 – Baseline PS semblance (a) and amplitude envelope (b) time slices just below the top of the Souris River Formation (1350 ms) shows the presence of a	

high semblance, high amplitude envelope anomaly in the same stratigraphic location as the zone of high fracture density from Figure 4.3. ....	85
Figure 4.10 – Baseline PS semblance (a) and amplitude envelope (b) time slices at the top of the Prairie Evaporite Formation (1426 ms) shows the presence of a high semblance, high amplitude envelope anomaly in the same stratigraphic location as the zone of high fracture density from Figure 4.5. The amplitude envelope slice also displays high value anomalies associated with areas with a higher density of mining operations.....	86
Figure 4.11 – Baseline PS semblance (a) and amplitude envelope (b) time slices through the Prairie Evaporite Formation (1474 ms) does not show the same amplitude envelope anomalies seen at the top of the Prairie Evaporite Formation (red ellipse). The semblance time slice shows one of the two carbonate reefs in the Winnipegosis Formation, but both carbonate reefs are not visible in the amplitude envelope time slice (two red circles). ....	89
Figure 4.12 – Baseline PS semblance (a) and amplitude envelope (b) time slices at the top of the Winnipegosis Formation (1496 ms). The semblance time slice shows the presence of a high semblance, high amplitude envelope anomaly previously interpreted as a zone of high fracture density seen in the above figures. The amplitude envelope time slice does not show the same anomaly.....	90
Figure 4.13 – Monitor PP semblance (a) and amplitude envelope (b) time slices through the Prairie Evaporite Formation (792 ms) clearly show the mine rooms. In the centre of the slice through the amplitude envelope volume, there is a low value anomaly which is significantly lower than that of the rest of the area. There is little difference between the anomaly in the baseline and monitor volumes. The mine workings to the southeast (red box) are highlighted in both vintages where the mine workings to the north (green box) do not show mine workings in the semblance volume.....	92
Figure 4.14 – Semblance (a) and amplitude envelope (b) difference between the PP baseline-monitor surveys at the top of the Prairie Evaporite Formation (792 ms). The red box highlights the time-lapse difference between the semblance and amplitude envelope volumes. The green box highlights mine workings which were not visible in either semblance vintage.....	93
Figure 4.15 – Semblance (a) and amplitude envelope (b) difference between the PP baseline-monitor surveys through the Prairie Evaporite Formation (836 ms). The red ellipse encompasses the area where the low amplitude, low velocity is found in the true semblance and amplitude envelope volumes. Note there is very little time-lapse difference in this area at this level, however, the amplitude envelope shows a high difference value to the southeast of the area.....	95
Figure 4.16 – Semblance (a) and amplitude envelope (b) difference between the PP baseline-monitor surveys at the top of the Winnipegosis Formation (848 ms). The red ellipse shows the area where a low amplitude, low velocity anomaly was	

interpreted. There is little difference between vintages in the semblance time slice, where the amplitude envelope shows a high value difference between the baseline and monitor volumes.....	98
Figure 4.17 – Monitor PS semblance (a) and amplitude envelope (b) time slices through the top of the Prairie Evaporite Formation (1426 ms). The red ellipse encompasses the area where a low velocity anomaly was interpreted. There is a small semblance anomaly, and a high amplitude envelope value associated with this anomaly at this level. The amplitude envelope slice also highlights the mine trends which are located in the areas of high values (amplitude envelope of 3.0-4.0). ....	99
Figure 4.18 – Monitor PS semblance (a) and amplitude envelope (b) time slices through the Prairie Evaporite Formation (1474 ms). The red ellipse shows the area where the previously interpreted low velocity anomaly is located. The semblance and amplitude envelope time slices at this level do not have an anomaly associated with this anomaly. The semblance time slice does not image the reef complexes which were seen in the baseline time slice at this level (Figure 4.11).....	100
Figure 4.19 – Monitor PS semblance (a) and amplitude envelope (b) at the top of the Winnipegosis Formation (1496 ms). The monitor semblance time slice shows an increase in size of the low velocity anomaly seen in Figure 4.12. The amplitude envelope time slice has a significantly increased value through the central low velocity anomaly (value of 4.0) which is not present in the baseline time slice at this level. ....	101
Figure 4.20 – Semblance (a) and amplitude envelope (b) difference between the PS baseline-monitor surveys through the Prairie Evaporite Formation (1474 ms). The semblance time slice shows a low semblance where the low velocity anomaly is located in the centre of the study area (red ellipse) and the carbonate mound feature previously interpreted to be present in the southeast of the study area (green triangle). The amplitude envelope time slice has a low value anomaly associated with the low velocity anomaly in the centre of the study area. ....	102
Figure 4.21 – Semblance (a) and amplitude envelope (b) difference between the PS baseline-monitor surveys at the top of the Winnipegosis Formation (1496 ms). The semblance difference shows the same low velocity anomaly in the centre of the study area where the amplitude envelope has a high value anomaly to the east of the same low velocity anomaly (red ellipse).....	103
A. 1 – The baseline (left) and monitor (right) PP, A-C azimuth PP time difference plots for the Birdbear Formation. ....	121
A. 2 – The baseline (left) and monitor (right) PP, B-D azimuth PP time difference plots for the Birdbear Formation. ....	121
A. 3 – The baseline (left) and monitor (right) PP, A-C azimuth PP time difference plots for the Dawson Bay Formation.....	121

A. 4 – The baseline (left) and monitor (right) PP, B-D azimuth PP time difference plots for the Dawson Bay Formation.....	122
A. 5 – The baseline (left) and monitor (right) PS, A-C azimuth PS time difference plots for the Birdbear Formation. ....	122
A. 6 – The baseline (left) and monitor (right) PS, B-D azimuth PS time difference plots for the Birdbear Formation. ....	122
A. 7 – The baseline (left) and monitor (right) PS, A-C azimuth PS time difference plots for the Dawson Bay Formation.....	123
A. 8 – The baseline (left) and monitor (right) PS, B-D azimuth PS time difference plots for the Dawson Bay Formation.....	123
B. 1 – Monitor PP semblance (a) and amplitude envelope (b) at the top of the Souris River Formation (710 ms).....	124
B. 2 – Monitor PP semblance (a) and amplitude envelope (b) just below the top of the Souris River Formation (720 ms). The red ellipse shows the area where the low amplitude, low velocity anomaly has been interpreted to be located. The green triangle highlights the area where a carbonate mound has been interpreted. ....	125
B. 3 – Monitor PP semblance (a) and amplitude envelope (b) just above the top of the Dawson Bay Formation (748 ms). The semblance and amplitude envelope time slices show anomalies in the area of the low velocity anomaly (red ellipses) and where the carbonate mound is located (green triangle). ....	126
B. 4 – Monitor PP semblance (a) and amplitude envelope (b) time slices at the top of the Prairie Evaporite Formation (774 ms). No significant anomalies can be seen on either of these slices. ....	127
B. 5 – Monitor PP semblance (a) and amplitude envelope (b) time slices through the Prairie Evaporite Formation (836 ms). The two reef complexes (red circles) are clearly visible in both the semblance and amplitude envelope time slices and the carbonate mound is highlighted in the amplitude envelope time slice with values between 1.0 and 3.0. ....	128
B. 6 – Monitor PP semblance (a) and amplitude envelope (b) time slices through the top of the Winnipegosis Formation (848 ms). The semblance and amplitude envelope time slices indicate that the northern reef complex is still present at the level, however, the second is not visible. In the semblance time slice, the low amplitude, low velocity anomaly in the centre of the study area is also visible (red ellipse).....	129
B. 7 – Semblance (a) and amplitude envelope (b) difference of the PP baseline-monitor surveys at the top of the Souris River Formation (710 ms). ....	130

B. 8 – Semblance (a) and amplitude envelope (b) difference of the PP baseline-monitor surveys just below the top of the Souris River Formation (720 ms). .....	131
B. 9 – Semblance (a) and amplitude envelope (b) difference of the PP baseline-monitor surveys at the top of the Dawson Bay Formation (748 ms).....	132
B. 10 – Semblance (a) and amplitude envelope (b) difference of the PP baseline-monitor surveys at the top of the Prairie Evaporite Formation (774 ms). .....	133
B. 11 – Monitor PS semblance (a) and amplitude envelope (b) time slices just below the top of the Souris River Formation (1350 ms). .....	134
B. 12 – Semblance (a) and amplitude envelope (b) difference of the PS baseline-monitor surveys through the Souris River Formation (1350 ms). .....	135
B. 13 – Semblance (a) and amplitude envelope (b) difference of the PS baseline-monitor surveys through the Prairie Evaporite Formation (1426 ms). .....	136

## List of Symbols, Abbreviations and Nomenclature

Symbol	Definition
$\sigma_{ij}$	Stress Component
$C_{ijkl}$	Elastic Tensor Modulus
$\varepsilon_{kl}$	Strain Component
$\varepsilon$	Anisotropy of a Rock (Thomsen)
$\gamma$	SH Anisotropy (Thomsen)
$\delta$	Reflection Moveout for P-wave (Thomsen)
$\lambda$	Lamé's First Parameter
$\mu$	Lamé's Second Parameter and Shear Modulus
$\theta$	P-wave Incidence Angle
$\phi$	S-wave Reflection Angle
$\alpha$	P-wave Velocity
$\beta$	S-wave Velocity
$\Delta t_{PP}$	PP Travel-Time
$\Delta t_{PS}$	PS Travel-Time
K	Bulk Modulus
Z	P-wave Impedance
3C	Multi-component
3D	Three-Dimension
ACP	Asymptotic Conversion Point
AVO	Amplitude Variation with Offset
AVOA	Azimuthal Amplitude Variation with Offset
CP	Conversion Point
CCP	Common Conversion Point
CMP	Common MidPoint
HTI	Horizontal Transverse Isotropy
MP	MidPoint
NMO	Normal MoveOut
P-wave	Compressional Wave
PP	Incident P-wave to Reflected P-wave
PS	Incident P-wave to Reflected S-wave
S-wave	Shear Wave
S1	Fast Shear Wave
S2	Slow Shear Wave
SH	Shear Wave with Horizontal Particle Motion
SS	Incident S-wave to Reflected S-wave
SV	Shear Wave with Vertical Particle Motion
VTI	Vertical Transverse Isotropy
Vp	P-wave Velocity
Vp/Vs	Ratio of P-wave Velocity to S-wave Velocity
Vs	S-wave Velocity
VVAZ	Velocity Variation with Azimuth
WCSB	Western Canada Sedimentary Basin

## Chapter One: INTRODUCTION AND THEORY

### 1.1 Introduction

The Devonian aged, Elk Point Group hosts one of the largest potash deposits in the world (Douglas, 1970; Mossop & Shetsen, 1993; Warren, 2006). These deposits extend across the majority of southern Saskatchewan, Canada, south into northwestern North Dakota, U.S.A. (Figure 1.1) and are within a regional salt layer known as the Prairie Evaporite Formation.



**Figure 1.1 – Distribution of potash-bearing rocks in the Prairie Evaporite Formation. The highlighted region covers the extent of the Elk Point Embayment and the dashed line surrounds the area of potash bearing rocks. (from Fuzesy, 1982)**

The potash in this region is of high quality, containing concentrations up to 20-30%  $K_2O$  within the salt deposits in the top 60-70 m of the top of the Prairie Evaporite Formation. The potash layer is approximately 30 m thick, 1000 m below the surface (Mossop & Shetsen, 1993; Zhang, 2010) and is being extracted using a so-called post room and pillar

method (Hustrulid & Bullock, 2001). This type of mining has the potential to induce changes in the subsurface stress field, which can create natural fracturing in the region (Zhang, 2010). These changes have been monitored for several years through the acquisition of several vintages of three-dimensional (3D), multicomponent (3C) seismic data volumes.

Zhang (2010) integrated geophysical analysis with petrophysical data and created models to determine the possible effects of fracturing on the acquired seismic data. Throughout the study, he found that a small amount of fractures can have a significant effect on seismic velocity and that rock properties associated with fractured rocks depend largely on the shape of the fractures. He also showed that aligned fractures would induce azimuthal anisotropy and shear-wave splitting in seismic data which would allow geophysicists to determine the orientation and possible intensity of fracturing in the carbonates surrounding the mine. To detect and monitor the extent of fracturing in the subsurface, he recommended that time-lapse 3D-3C seismic volumes be acquired, as the velocity reduction of shear-waves (S-waves) across a fracture is larger compared to the velocity of P-waves (O'Connell & Budiansky, 1974; Zhang, 2010) resulting in an increase in  $V_p/V_s$ . The two surveys used in this study are approximately 6.5 km<sup>2</sup> in area and the acquisition parameters along with the processing flow that was followed is shown in the EBCDIC header in Figure 1.2.

## **1.2 Geology**

The Elk Point Embayment extends for 1900 km from northeastern British Columbia towards the southeast where it merges with the Williston Basin in southeastern

Saskatchewan, Manitoba, Canada and North Dakota, U.S.A. (Figure 1.3). A major transgression, followed by a large scale regression at the end of the Middle Devonian resulted in the deposition of a thick package of carbonates separated by thin layers of Eolian red beds and one thick salt package called the Prairie Evaporite Formation (Mossop & Shetsen, 1993).

```

Amplifier:I/O 4,1540 chan,IEEE SEG-Y, Out-3/4 Nyq Min Phase,Notch OUT
Record Length: 5.0 s Sample Interval: 1 ms
Source: Dyn, single hole, 0.5 Kg at 9 m, N-S 125 m lines, 30 m source int
Sensors: VectorSeis, single 3-comp, 0 degrees, E-W 180 m lines, 25 m int
Typical Patch: 14 lines x 110 stations, 2340 m x 2725 m
UNFILTERED RADIAL 2004 MIGRATION
*** Processing History ***
Processed by: Sensor Geophysical Ltd., August, 2010
Reformat: Record length 3.5 s, Sample interval 1.0 ms
Geometry Assignment, Asymptotic 3D Binning, CDP Bin size 12.5 m x 15 m
H1/H2 to Radial/Transverse Rotation: 9 degrees, Trace edits, 60 Hz removal
SVD Filter: to remove groundroll
Amplitude Recovery: Spherical divergence correction, Additional gain 4 dB/s
Surface-Consistent Deconvolution
Resolved: Source, Receiver, Offset Applied: Source, Receiver
Operator Type Spiking, Operator length 100 ms, Prewhitening 0.01%
Design window 120-2300 ms at 0 m, 1000-2500 ms at 2170 m offset
Lateral Receiver Statics, Refraction Statics: Datum 620 m Repl vel 2000 m/s
Surface-Consistent Statics: Max shift 32 ms, window 500-2200 ms
Surface Consistent Amplitude Scaling: SHOT, REC
T-F Adaptive Noise Suppression, Offset Consistent Gain Control
Time Variant Whitening: 500 ms, 6 panels, 2/6-60/80 Hz
CDP Trim Statics: F-XY Filtered model, 6 ms max shift, 400-2200 ms
Anisotropic NMO: eta 0.1
Front-End Muting: (ms) 0 400 650 1100 2300 Offset (m) 350 400 512 762
2000
Automatic Gain Contral: mean, 500 ms, 5/10-30/40 Hz band
Common Conversion Point Stack: 60% GammaEff, 0 ms bulk
Time Variant Whitening: 500 ms, 6 panels, 2/6-60/80 Hz
F-XY Filter, 5 x 5 pt oper,100 ms window,50 ms taper
Anisotropic Diffusion Filter
Implicit FD Time: Aperture 65 deg,95% smoothed stacking velocities
Time Variant Scaling: mean, centre-to-centre, multiple gates

```

**Figure 1.2 – Processing flow.**

Figure 1.4 shows a stratigraphic column from southern Saskatchewan. The Prairie Evaporite Formation contains a world-class potash deposit, with an estimated 56 billion tonnes of extractable  $K_2O$  making up 30% of the world's supply of potash (Douglas, 1970; Mossop & Shetsen, 1993; Warren, 2006). The Frasnian-Famnenian, Saskatchewan Group stratigraphy were deposited in a shallow marine to lagoonal environment capping the zone of interest for this study (Cen & Hersi, 2006).

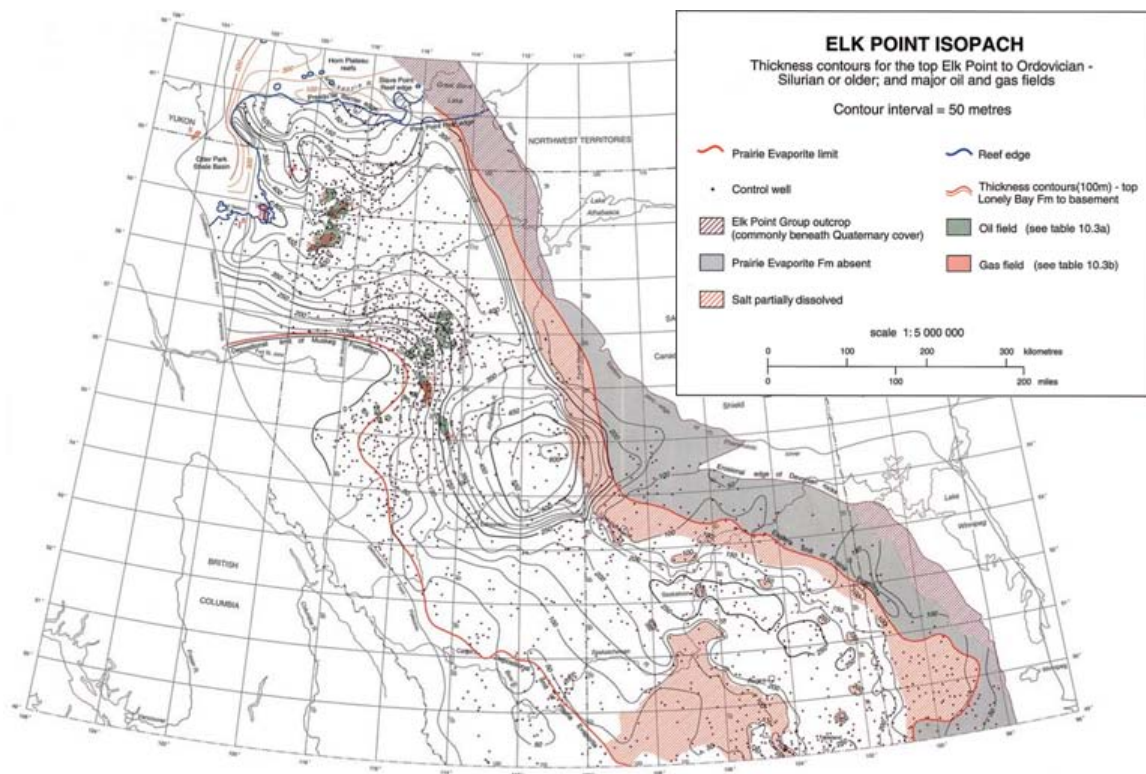


**Figure 1.3 – Map showing the extent of the Elk Point Group through the Western Canada Sedimentary Basin (WCSB). (from Mossop & Shetsen, 1993)**

The Saskatchewan Group is conformably overlain by the Three Forks Group which consists of a carbonate succession unconformably overlain by the Bakken sand and the Madison Group of carbonates, topped by a large scale erosional event which removed the stratigraphy from the top of the Mississippian to the Triassic (Figure 1.4).

### 1.2.1 Stratigraphy and Depositional Setting

During the third major transgression in Middle Devonian times, an ancient sea reached southeastern Saskatchewan where the Ashern Formation, a red to grey, unfossiliferous, microcrystalline dolostone to limestone was deposited (Lodbell, 1982). The regressive part of this sequence deposited a fossiliferous, shallow-marine carbonate known as the Winnipegosis Formation.

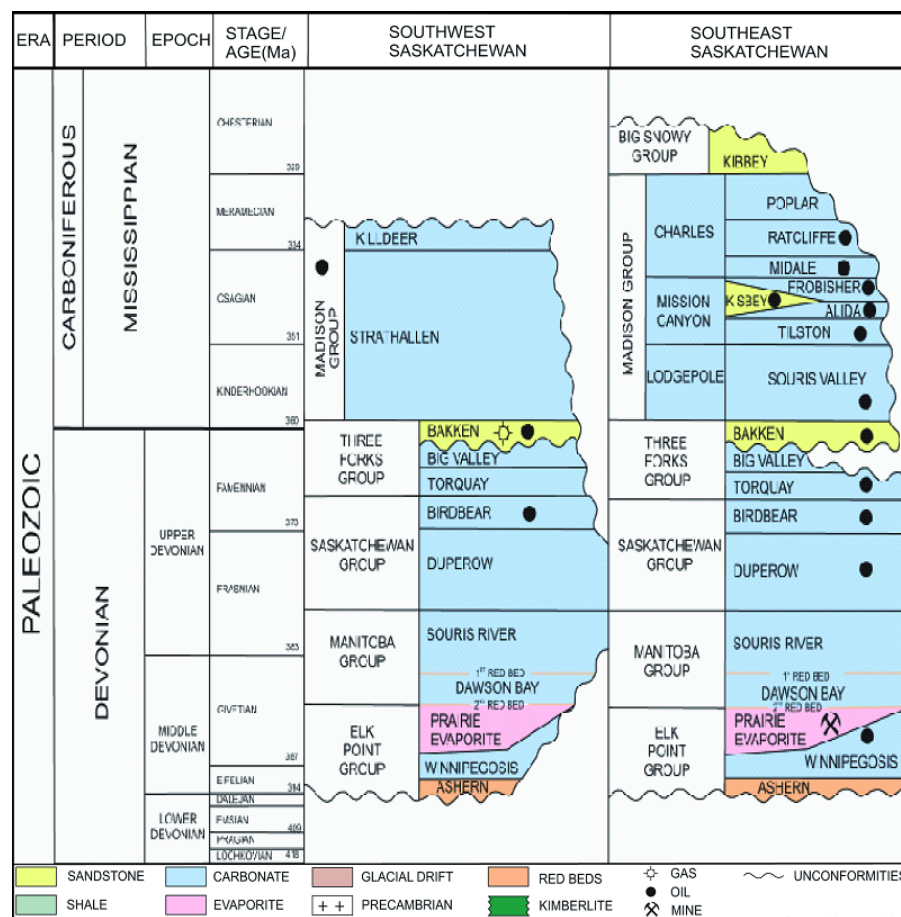


Figure 1.4 – A stratigraphic column showing the Devonian and Mississippian stratigraphy of interest for this study. (modified from Saskatchewan Ministry of Energy and Resources, 2011)

An increase in subsidence or rise in sea level is attributed to have created vertical reef growth in the Winnipegosis Formation, which can have carbonate reefs reach thicknesses between 70 m and 100 m (Gendzwill, 1978; Mossop & Shetsen, 1993). The relief of the carbonate mounds controls the thickness of the overlying Prairie Evaporite Formation, and acts as an excellent feature to ensure proper placement of the Winnipegosis Formation horizon during seismic interpretation.

The Prairie Evaporite Formation was deposited after a mid-Givetian transgression, generated by increased subsidence, creating a barrier reef to the northwest of the study area. The reef limited the flow of sea water into the Elk Point Embayment allowing salt water to be trapped. This facilitated the deposition of the 150m thick evaporate sequence (Mossop & Shetsen, 1993; Zhang, 2010). Potash can be found in the upper 60-70m of the formation, which consists of four potash bearing units, the Esterhazy, White Bear, Belle Plaine and Patience Lake members (Mossop & Shetsen, 1993; Warren, 2006). These four members contain some of the richest potash deposits in the world, with  $K_2O$  concentrations averaging between 20-30% (Douglas, 1970; Mossop & Shetsen, 1993; Warren, 2006). In the study area, the potash located in the Esterhazy member is the target of mining operations, situated 20-30 m below the top of the Prairie Evaporite Formation, where the ore is being extracted via room and pillar method (Zhang, 2010).

The Manitoba Group unconformably overlies the Prairie Evaporite Formation, and begins with a 9 m to 12 m thick, red-greenish shale called the Second Red Bed Formation, which gradually changes to dolomitic mudstones and limestones (Braun & Mathison, 1986). Above, we find the Dawson Bay Formation, a regionally extensive, comparatively fossiliferous and locally fractured limestone carbonate. This formation is between 45 m and

55 m thick throughout the study area and is capped by another thin red bed unit (Braun & Mathison, 1986; Dunn, 1982; Mossop & Shetsen, 1993). Deposition of the Manitoba Group concluded with the Souris River Formation, a dolomitic shelf carbonate deposited to the southeastern extent of the seaway during a relative decrease in sea-level caused by a lack of accommodation space for the amount of accumulating sediment (Mossop & Shetsen, 1993).

The Upper Devonian Birdbear Formation was a key stratigraphic unit used to facilitate the well tie process. The Birdbear Formation is a 45 m thick shallow-water, marine carbonate deposited on an Upper Devonian shelf throughout the course of a single transgressive-regressive cycle (Halabura, 1982; Mossop & Shetsen, 1993).

Above the Birdbear Formation sits the upper Devonian Three Forks Group which is made up of the dolomitic Torquay Formation and the Big Valley Formation a deep marine fossiliferous limestone which is 25 m in thickness (Mossop & Shetsen, 1993; Christopher, 1962). The Bakken Formation bridges the Devonian-Carboniferous boundary and is a predominantly fine-grained siliciclastic unit deposited in a shallow neritic environment. The Carboniferous Lodgepole Formation is 75 m thick and is made up of carbonate ramp, siliciclastic and poorly differentiated carbonate platforms. A major erosional unconformity has removed the upper Carboniferous, Triassic and Jurassic stratigraphy which leaves the Blairmore Group on top of the Lodgepole Formation (Mossop & Shetsen, 1993). The Blairmore Group in Saskatchewan is the equivalent to the sandstones of the Mannville Group and Viking Formation and the shales of the Joli Fou Formation in the Alberta Oil Sands (Mossop & Shetsen, 1993). The remaining stratigraphy is upper Cretaceous shales for the remaining 370 m to the surface.

### 1.3 Seismic Anisotropy

Seismic anisotropy is defined to be the variation in seismic velocity with direction of seismic wave propagation (Sheriff, 2011). The study of seismic anisotropy began in the mid-1900s when seismic waves were observed to propagate at different velocities in different directions through the upper stratigraphy in the Earth's crust (McCollum & Snell, 1932; Uhrig & Van Melle, 1955). Since then, improvements in seismic acquisition technology and computer processing power have provided seismic anisotropy with a more practical role in the interpretation of seismic data.

Seismic anisotropy in recent years has increasingly become the subject of geophysical studies. In the past, assumptions of isotropy have been used to find most of the world's known conventional hydrocarbon reservoirs (Thomsen, 2002). Although these assumptions are often valid, they are not optimal practices for the exploitation of unconventional resources; the subtleties within these reservoirs are important. The development of more accurate seismic interpretations relies on the ability to determine the extent of seismic anisotropy in the subsurface, and any deviations from the isotropic assumption can lead to the determination of the anisotropic parameters in the region of interest (Thomsen, 2002).

Anisotropic parameters for weak anisotropy were defined by Thomsen (1986) by relating stress and strain through an elastic modulus tensor (Equation 1.1). For the isotropic case, this tensor has two independent variables (Equation 1.2), whereas the transverse isotropic case (defined below) is more complicated with five independent components (Equation 1.3).

$$\sigma_{ij} = \sum_{k=1}^3 \sum_{l=1}^3 C_{ijkl} \epsilon_{kl}, i, j = 1, 2, 3 \quad (1.1)$$

where  $\sigma$  is a stress component linearly dependent on each component of strain,  $\epsilon$ . Stress and strain are related by the elastic modulus tensor,  $C$ .

$$\begin{bmatrix} C_{33} & (C_{33} - 2C_{44}) & (C_{33} - 2C_{44}) & & & & \\ & C_{33} & (C_{33} - 2C_{44}) & & & & \\ & & C_{33} & & & & \\ & & & C_{44} & & & \\ & & & & C_{44} & & \\ & & & & & C_{44} & \\ & & & & & & C_{44} \end{bmatrix} \quad (1.2)$$

$$\begin{bmatrix} C_{11} & (C_{11} - 2C_{66}) & C_{13} & & & & \\ & C_{11} & C_{13} & & & & \\ & & C_{33} & & & & \\ & & & C_{44} & & & \\ & & & & C_{44} & & \\ & & & & & C_{44} & \\ & & & & & & C_{66} \end{bmatrix} \quad (1.3)$$

Combinations of the elastic modulus tensor make up the parameters,  $\epsilon$ ,  $\gamma$  and  $\delta$  which represent weak anisotropy and are defined as:

$$\epsilon = \frac{C_{11} - C_{33}}{2C_{33}} \quad (1.4)$$

$$\gamma = \frac{C_{66} - C_{44}}{2C_{44}} \quad (1.5)$$

$$\delta = \frac{(C_{13} + C_{44})^2 - (C_{33} - C_{44})^2}{2C_{33}(C_{33} - C_{44})}, \quad (1.6)$$

where  $\epsilon$  refers to the anisotropy of a rock,  $\gamma$  corresponds to the SH anisotropy and  $\delta$  defines reflection moveout for P-waves at near-vertical incidence. In the isotropic case, the components of the elastic modulus tensor are related to the Lamé Parameters ( $\lambda$  and  $\mu$ ) and the Bulk modulus (K) by:

$$C_{33} = \lambda + 2\mu = K + \frac{3}{4}\mu \quad (1.7)$$

and

$$C_{44} = \mu. \quad (1.8)$$

In the transverse isotropic case however, three additional components ( $C_{11}$ ,  $C_{13}$  and  $C_{66}$ ) are introduced into the tensor (Thomsen, 1986).

### ***1.3.1 Transverse Isotropy***

The most commonly studied case of anisotropy is transverse isotropy (Helbig & Thomsen, 2005), which is defined to be seismic waves traveling at the same velocity in two orthogonal directions, but at a different velocity in the third (Yilmaz, 2001; Thomsen, 1986). Transverse isotropy is a very special case of seismic anisotropy and has two popular manifestations. The most studied case of which is that of vertical transverse isotropy (VTI) (Helbig & Thomsen, 2005) which is defined to be an anisotropic material with a vertical axis of symmetry, typically induced by layered isotropic sedimentary bedding, and first introduced by Rudzki (1898). This layering creates a difference between the seismic velocity of layers in the direction of bedding and the seismic velocity in the direction perpendicular to bedding (Figure 1.5) (Ruger, 1997; Tsvankin, 1997; Yilmaz, 2001; Sheriff, 2011).

The second most common type of transverse anisotropy is horizontal transverse isotropy (HTI), which is also known as azimuthal anisotropy (Hudson, 1981; Tsvankin, 1997) (Figure 1.6). In cases of HTI seismic velocity varies from one horizontal direction to another. Since horizontal bedding induces VTI, then vertical bedding, such as highly folded stratigraphy, is one way HTI is created in the subsurface (Yilmaz, 2001). Another, more

common and more practical way for HTI to be produced is the presence of vertically oriented fractures (Figure 1.6). Fractures are induced when the subsurface stresses are greater than the internal strength of the rock causing the rock to crack along a plane of weakness (Park, 2005). Seismic anisotropy is created by fractures because of the reduction in cohesion across the fractures which results in a slower seismic velocity perpendicular to fracture strike. Where seismic waves propagate parallel to a fracture, there is no reduction in seismic velocity, as the seismic wave does not propagate across the fracture prior to being recorded. Therefore, the effect of a single fracture is impossible to detect. A fracture network with a preferential orientation, on the other hand, causes a reduction in seismic velocity of both P- and S-waves perpendicular to the strike of the fractures (Lynn, et al., 1999; O'Connell & Budiansky, 1974; Ruger, 1997). Should the fracture network be extensive enough, a directional velocity anomaly should be detectable as an increase in travel-time, which is evident when examining travel-time differences between orthogonal source-receiver ray paths.

#### 1.3.1.1 Fracture Detection

Detection of fractures has become increasingly important for resource exploration. Fractures are typically oriented parallel to the dominant horizontal stress direction (Ruger, 1997; Crampin, 1985; Crampin & Lovell, 1991) and over the past decade several case studies have been published using different methodologies to determine the intensity and orientation of fractures.

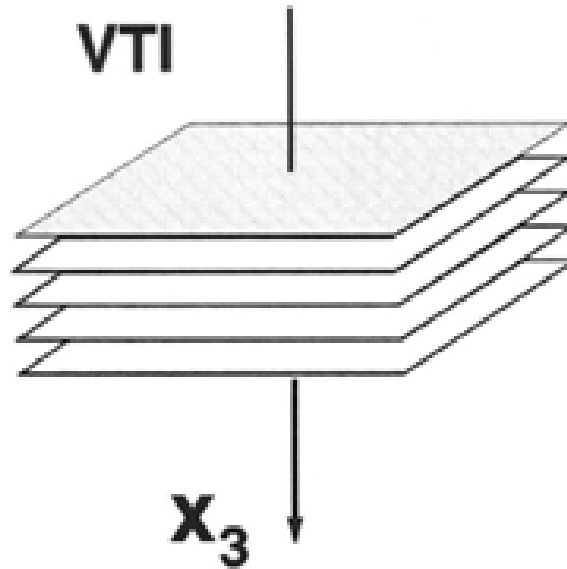


**Figure 1.5 – Cartoon showing a VTI model of horizontally layered stratigraphy. (from Tsvankin, 1997)**

A successful method for the characterization of subsurface fractures is Azimuthal Amplitude Variation with Offset (AVOA). There are many case studies which demonstrate the ability of AVOA to determine fracture strike and relative fracture density. The results have been confirmed through correlation with results from other techniques for fracture characterization such as mug logs, borehole measurements and estimates of regional and local stress regimes (Perez, Grechka, & Michelena, 1999; Neves, Al-Marzoug, Kim, & Nebrija, 2003; Gray, Boerner, Todorovic-Marinic, & Zheng, 2003; Roberts, et al., 2001; Gray, Roberts, & Head, 2002; Gray & Head, 2000).

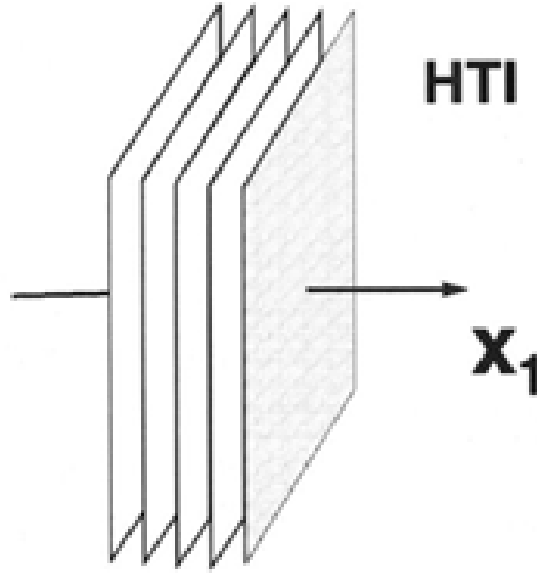


**Figure 1.6 – Cartoon showing a HTI model of vertically layered stratigraphy or an isotropic matrix with vertically oriented fractures. (from Tsvankin, 1997)**

AVOA relies on stacking multi-azimuth seismic data into offset and azimuth bins which are analysed for changes in seismic amplitude (Jenner, 2002). This is done using an AVO approach (Equation 1.9) defined by Ruger (1997) to encompass an HTI medium with an isotropic overburden.

$$R(\theta) = \frac{1}{2} \frac{\Delta Z}{Z} \left\{ \frac{\Delta \alpha}{\alpha} \left( \frac{2\alpha}{\beta} \right)^2 \left( \frac{\Delta \mu}{\mu} - 2\Delta \gamma \right) \Delta \delta \right\} \sin^2 \theta + \frac{1}{2} \left\{ \frac{\Delta \alpha}{\alpha} + \Delta \epsilon \right\} \sin^2 \theta \tan^2 \theta, \quad (1.9)$$

where  $R$  is the reflection coefficient,  $\theta$  is the angle of incidence,  $\alpha$  is P-wave velocity,  $\beta$  is S-wave velocity,  $\delta$ ,  $\epsilon$  and  $\gamma$  are Thomsen's parameters,  $Z$  is P-wave impedance and  $\mu$  is the Shear modulus (Ruger, 1997).

Shear-wave splitting, also known as shear-wave birefringence, is a phenomenon caused by anisotropy which is induced when seismic waves propagate through a medium

exhibiting one or more of the following: aligned crystals, direct stress-induced anisotropy, lithologic anisotropy, structural anisotropy or stress-aligned fracture-induced anisotropy (Crampin & Lovell, 1991; Alford, 1986). As S-waves propagate through the subsurface, the S-waves polarize into a fast S-wave (S1) and slow S-wave (S2) (Figure 1.7), where the fast S-wave is oriented parallel to fractures and the slow S-wave is oriented perpendicular to fractures (Crampin & Lovell, 1991; Guevara-Ochoa & Cary, 2006; Sandanayake & Bale, 2011; Elkibbi & Rial, 2003; Horne, 2003; Crampin et al., 1989). Alford (1986) determined that this polarization of S-waves may be the cause of some of the noise commonly attributed to S-wave data.

Winterstein & Meadows (1991) showed that S-waves can polarize to specific azimuths in particular formations, and more importantly, that the travel-time difference between the two polarizations increased in two zones in the Lost Hills field. They also observed that polarization of the S1 mode correlated with the strike of hydraulic fractures and dominant local horizontal stresses responsible for inducing seismic anisotropy in the area and could be used to predict the orientation of fractures. A study Sandanayake & Bale (2011) also used shear-wave splitting to characterize fracture density where natural and hydraulic fractures are concerned. It shows that production values for tight oil wells in the Shaunavon Formation have a direct correlation between production and the naturally fractured oil bearing sands (Figure 1.8) and where hydraulic fracturing was done, production values are higher.

Seismic travel-time analysis methods, such as Velocity Variation with Azimuth (VVAZ), are techniques used to measure how the seismic wave front is affected by travelling through a zone of seismic anisotropy. When the ray paths from different

azimuths travel through the fractured zone, the integrity of the rock is compromised perpendicular to the fracture orientation meaning P-waves do not propagate at the same velocity in all directions. These velocity variations are more significant at larger offsets and can be approximated using a velocity ellipse in HTI media. If there is a dominant fracture orientation, these changes in velocity manifest as travel-time differences which are detectable when the seismic travel-times are analysed with respect to azimuth. This technique has been applied previously in earthquake seismology (Vetter & Minster, 1981; Shearer & Orcutt, 1985), vertical seismic profiling (Sayers & Ebrom, 1997; Al Dulaijan, Owusu, & Weber, 2012) and reflection seismology (Wang & Zheng, 2007; Zheng, Wang, & Perz, 2008; Delbecq, Downton, & Letizia, 2013) to successfully determine dominant orientation and relative intensity of fracturing (Delbecq, Downton, & Letizia, 2013).

#### **1.4 Multicomponent Seismology**

Multicomponent seismology focuses on the use of compressional (P-wave) and shear wave (S-wave) seismic wave modes to increase our understanding of subsurface rock properties and ultimately to improve our geological interpretation of hydrocarbon reservoirs and ore deposits. As many of today's known hydrocarbon fields are becoming increasingly mature, the use of new technology is required to optimize hydrocarbon extraction from existing fields as well as to determine the feasibility of more subtle and complex hydrocarbon traps (Tatham & McCormack, 1991). Multicomponent seismic technology became a topic of increasing interest in the 1960s, when most seismic exploration was focused on structural interpretation. It was thought that S-waves sections might carry higher frequency content than their P-wave counterparts. It was found, however, that S-waves did not produce higher

quality results, but in fact the S-wave sections were of poorer quality and had lower frequency content than the P-wave sections (Erickson, Miller, & Waters, 1968).

Pickett (1963) attempted to evaluate the potential uses of acoustic logs for formation evaluation, including laboratory experiments to analyze the transit-times of P- and S-waves. He found that P- and S-wave velocities are dependent on effective stress (Figure 1.9), porosity and lithology (Figure 1.10), and that changes in S-wave velocities are larger than changes in P-wave velocities. Pickett (1963) also found that S-waves experience a more significant reduction in amplitude due to fracturing in dolomites than do their P-wave counterpart.

In another study, Gardner and Harris (1968) compared the P- and S-wave responses to different pore saturants. They determined that water saturation increased the P-wave velocity in a sand matrix, but the S-wave velocity decreased under the same conditions, in both unconsolidated and consolidated sands (Figure 1.11), although the ratio of P- and S-wave velocities ( $V_p/V_s$ ) remained relatively constant at varying porosities in a water saturated matrix.

As laboratory research was being conducted into the usefulness of S-waves in providing additional information about lithology, stress and fluid content, there were also advances in the acquisition of S-waves using horizontal vibrators to explore the viability of commercial use of S-wave seismic data. During the early years of S-wave data acquisition studies many of the main concepts of data acquisition and processing were developed, and are still used today (Hardage et al., 2011).

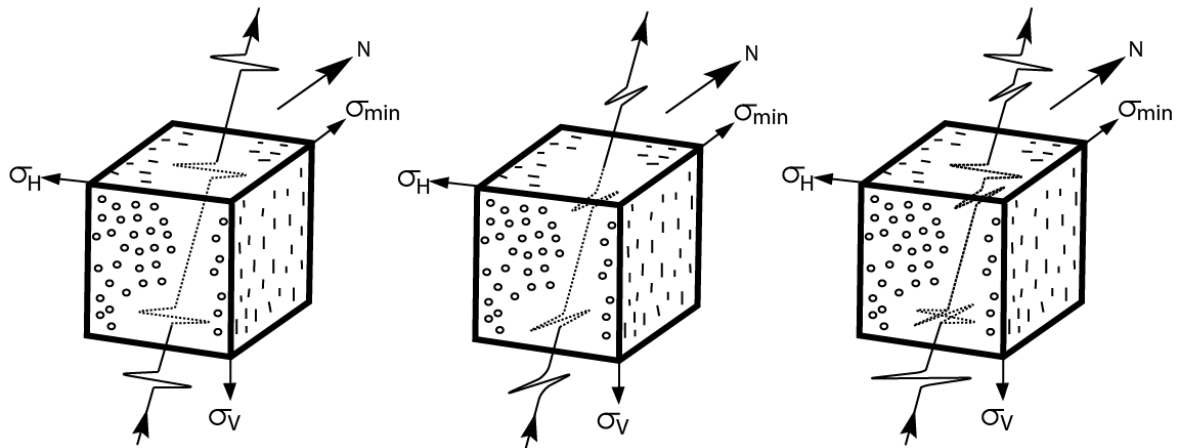


Figure 1.7 – S-wave polarization into a slow S-wave and a fast S-wave due to the presence of east-west oriented fractures. (modified from Crampin et al., 1989)

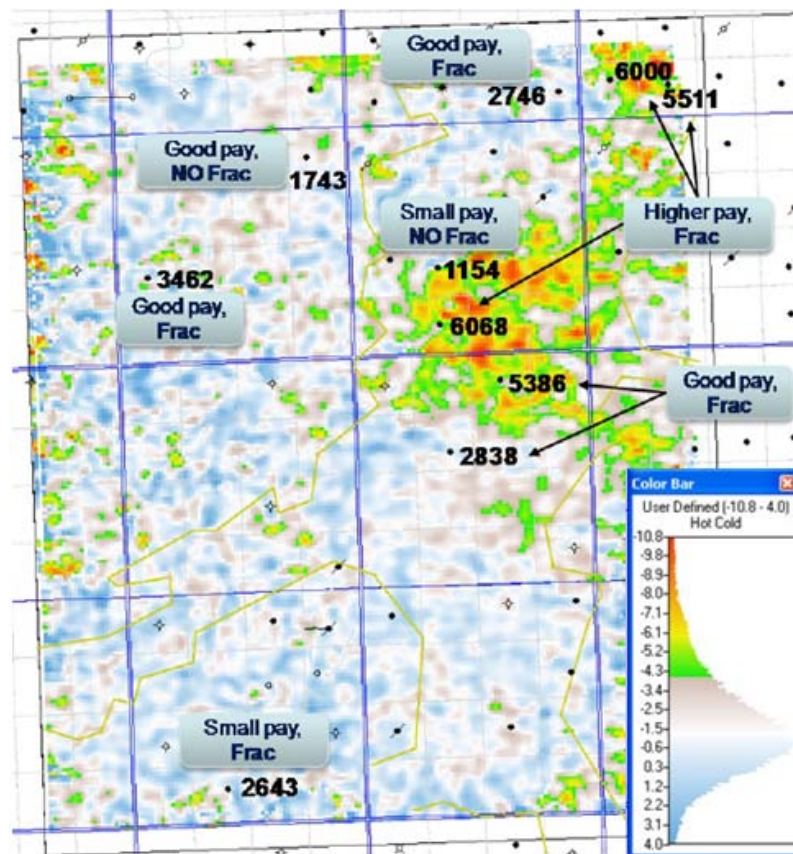
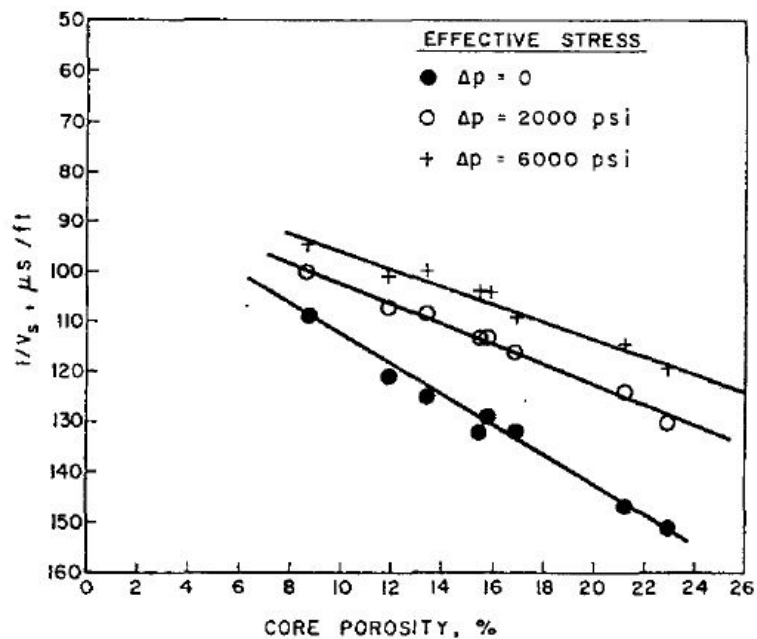


Figure 1.8 – Larger time differences between P-S1 and P-S2 associated with anisotropy (hot colors) have a good correlation with three month total fluid production from wells. (from Sandanayake & Bale, 2011)

Many researchers agree that multicomponent seismic data provide important insight into subsurface rock properties (Tatham & McCormack, 1991). Although S-waves are more costly and complicated to acquire they do present many advantages through their ability to image steeply dipping structures, structure within and beneath gas charged stratigraphy and faulting associated with salt intrusions (Stewart et al., 2003).



**Figure 1.9 – Experimental results showing the relationship between S-wave slowness and porosity while under different levels of stress in dolomite. (from Pickett, 1963)**

Seismic waves propagate through the earth in two primary modes, namely a compression wave and a shear wave. A shear wave with particle motion in a vertical plane called an SV wave and that with particle motion in a horizontal plane called an SH wave (Figure 1.12). As a seismic wave arrives at a receiver, the events which correspond to specific stratigraphic interfaces change in seismic character. This is the result of the orientation of particle motion associated with each wave type, as the subsurface responds differently to

seismic energy in different directions (Hardage et al., 2003). Travel-time differences are one of the most important aspects of interpreting the events on PP, PS and SS sections. Each mode of propagation (P- and S-waves) has its own seismic velocity, and although the exact velocities of each mode are not known at first, using approximate values allows for a reasonable initial model which then improves through processing. Combining approximate velocity models with PP, PS and SS synthetic seismograms provides excellent event location in order to relate seismic travel-times to subsurface lithological boundaries (Figure 1.13) (Fertig & Krajewski, 1989). The temporal location of seismic events is essential to calculating  $V_p/V_s$  – one of the main diagnostic attributes for multicomponent seismic data interpretation (Pickett, 1963; Gardner & Harris, 1968; Tatham & Stoffa, 1976; Van Dok & Gaiser, 2001; Tatham R. , 1982).

When processing P-P seismic data, the downgoing and upgoing wavefields both travel at the same velocity which allows common midpoint (CMP) stacking to be applied, increasing the quality of a final section. When horizontal vibrators are used as sources to capture S-wave information, the downgoing and upgoing wavefields are equivalent and therefore CMP-based processing can still be used (Tessmer & Behle, 1988; Hardage et al., 2011). Early S-wave seismic sections obtained using horizontal vibrators were comparable to those of P-waves (Erickson, Miller, & Waters, 1968; Waters, 1978; Rice, et al., 1981). S-waves also have the ability to image areas which P-wave resolution and signal-to-noise ratio is substandard (Hardage et al., 2011).

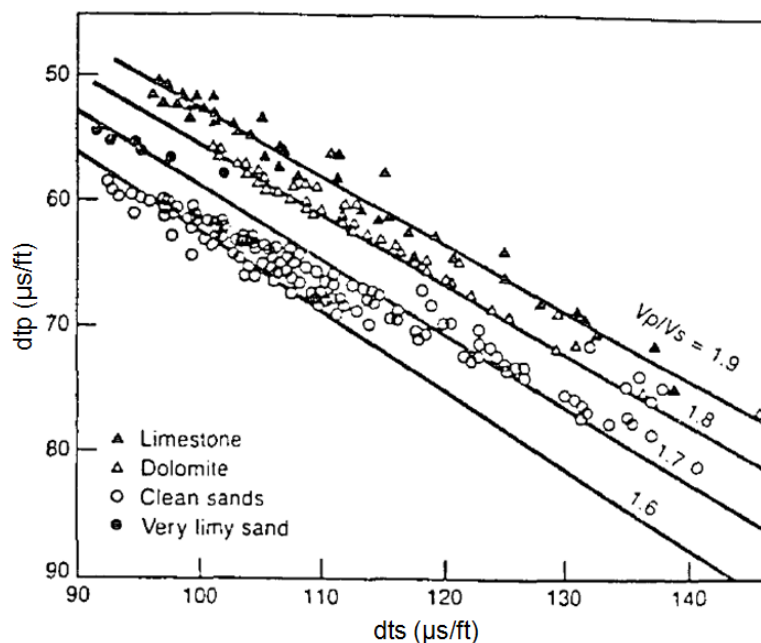


Figure 1.10 – Comparison of reciprocal P- and S-wave velocities for different lithologies. The lines are indicative of specific  $V_p/V_s$  values. (from Pickett, 1963)

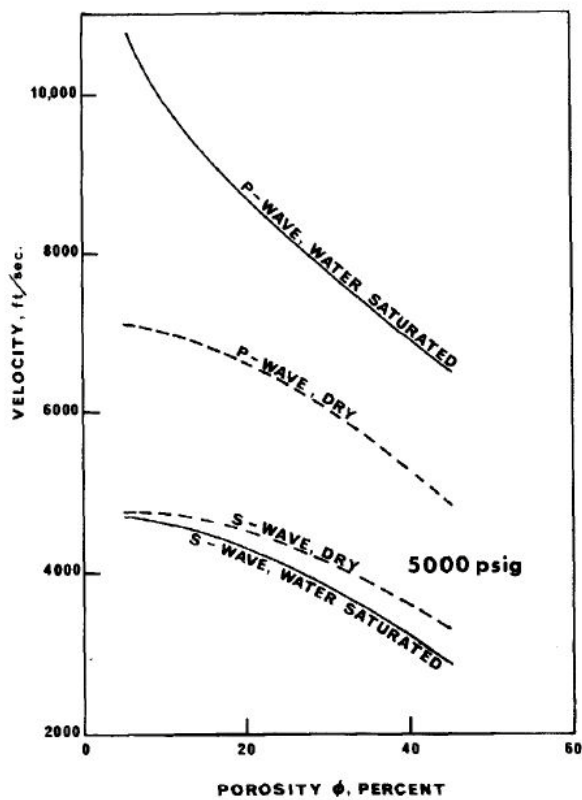
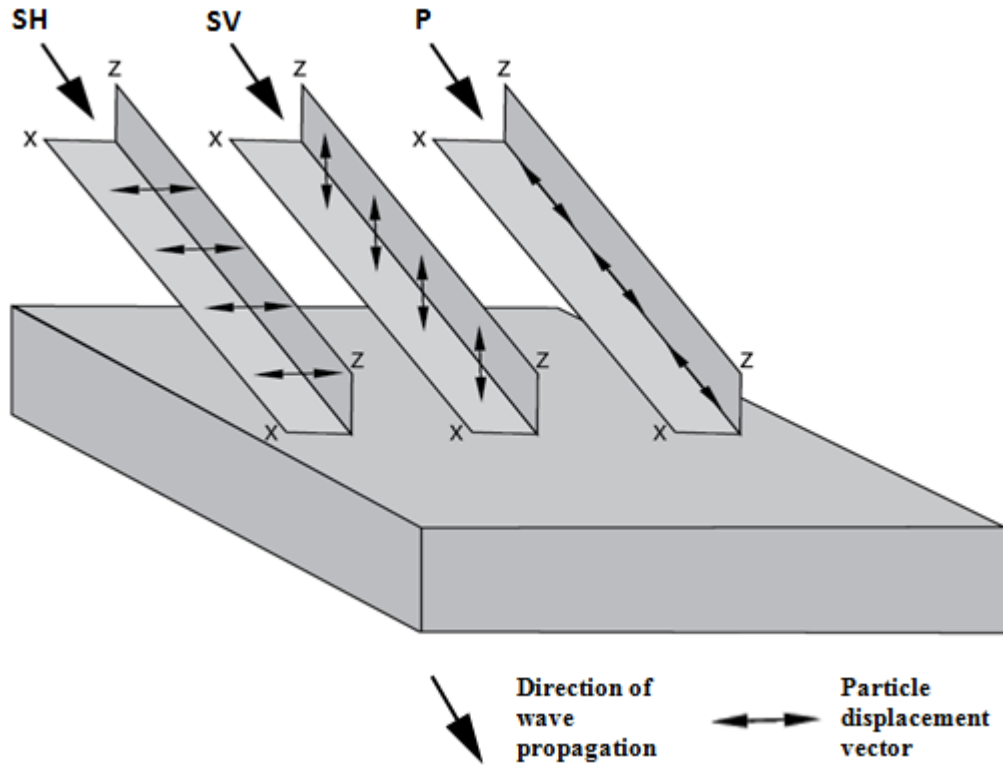


Figure 1.11 – Velocity/porosity relationship. (from Gardner & Harris, 1968)



**Figure 1.12 – Diagram showing a full multicomponent seismic wavefield propagating through a medium. For these three modes the direction of wave propagation is the same, but the particle displacement vectors are different. (modified from Sheriff, 2011)**

The problem with S-wave sources, specifically vibrators, is that they are expensive, and can be much more difficult to transport to isolated locations, and S-S seismic sections are often noisier and have lower temporal resolution than P-P sections (Stewart et al., 2002). The increased noise in S-wave seismic sections is, in part, due to the polarization of S-waves into a fast and slow direction.

### ***1.4.1 Converted Wave Seismology***

Converted waves provide shear information at recording times 30% shorter than S-S surveys (Stewart et al., 2002), and were first used recorded with success to map subsurface structure during the 1940s using an explosive source on the surface (Ricker & Lynn, 1950). They are popular today because onshore seismic surveys are typically recorded using P-wave sources such as dynamite and vertical vibrators. Vertical seismic sources are less expensive to purchase and operate than horizontal seismic sources and dynamite is much easier to transport to rural or isolated survey locations (Stewart, 2002). In the case of marine surveys, P-wave sources, when combined with 4 component ocean bottom cable strings attached to the sediment on the ocean floor, provided the only method of collecting multicomponent seismic information.

Converted waves are defined as a P-wave which converts upon reflection, with the reflected ray angle governed by Snell's Law (Equation 1.10), as an S-wave, with SV particle motion.

$$\frac{\sin \theta}{V_p} = \frac{\sin \phi}{V_s}, \quad (1.10)$$

where  $\theta$  is the angle of the incident P-wave,  $V_p$  is the P-wave velocity,  $\phi$  is the angle of the reflected SV-wave and  $V_s$  is the velocity of the SV-wave. This mode conversion from P- to SV, means that the downgoing wavefield velocity ( $V_p$ ) differs from that of the upgoing wavefield velocity ( $V_s$ ) resulting in an asymmetric ray path through the subsurface, making the CMP stack incorrect (Tessmer & Behle, 1988). The point at which the mode conversion occurs is known as the conversion point (CP) and because S-wave velocity is lower P-wave velocity the conversion point is closer to the receiver than the midpoint (Figure 1.14).

The CP location also varies with depth for any source-receiver offset in an asymptotic fashion (Figure 1.15) (Hardage et al., 2011; Stewart, 2002; Tessmer & Behle, 1988). The CP approaches the asymptotic conversion point (ACP) at large depths. The development of the common conversion point (CCP) stack allows for the same attenuation of multiples and the reduction of random noise which is achieved in conventional P-wave sections using CMP stacking.

## **1.5 Thesis Objectives**

The main objective of this thesis is to analyse a multicomponent, time-lapse seismic dataset for assessment of fractures in the subsurface associated with potash mining operations in Saskatchewan, Canada. These fractures are vertical to sub-vertical in nature and induce seismic anisotropy known as HTI. The stratigraphy of interest is a carbonate succession of Devonian age, located at depth between 600 and 1100 m below the surface. The data were analysed using several techniques to determine whether the fractures in the subsurface create measurable anisotropic effects on PP and PS seismic volumes.

In order to assess the level of anisotropy in the area travel-time differences between azimuths will be analysed. This will be done through the interpretation of several key horizons in seismic volumes with stacks of different source-receiver ray paths. The registration of PP and PS seismic volumes allows for the calculation of  $V_p/V_s$  which is used to indicate changes in lithology, the presence of fluid and in the case of this study, the location of fractures, through significant decreases in S-wave velocity. A primary concern throughout this process is the accuracy of horizon placement on the PS volumes, as converted wave datasets are subject to reduced temporal resolution compared to their PP

counterparts. This is resolved through the selection of appropriate seismic events which are then bulk shifted, in time, to a more suitable location.

Finally, seismic attribute analysis, through the examination of complex trace and multi-trace attributes, is conducted to attempt to highlight zones of highly fractured stratigraphy. Together, travel-time,  $V_p/V_s$  and attribute analysis will improve our understanding of the geological causes of a low velocity, low amplitude anomaly through the centre of the study area.

## **1.6 Summary of Software Used**

Several software packages were used throughout the course of this thesis:

- Seisware
- Hampson-Russell ProMC and eLog
- Quaddes (CREWES Toolkit)
- Syngram (CREWES Toolkit)
- Microsoft Office for the preparation of this thesis

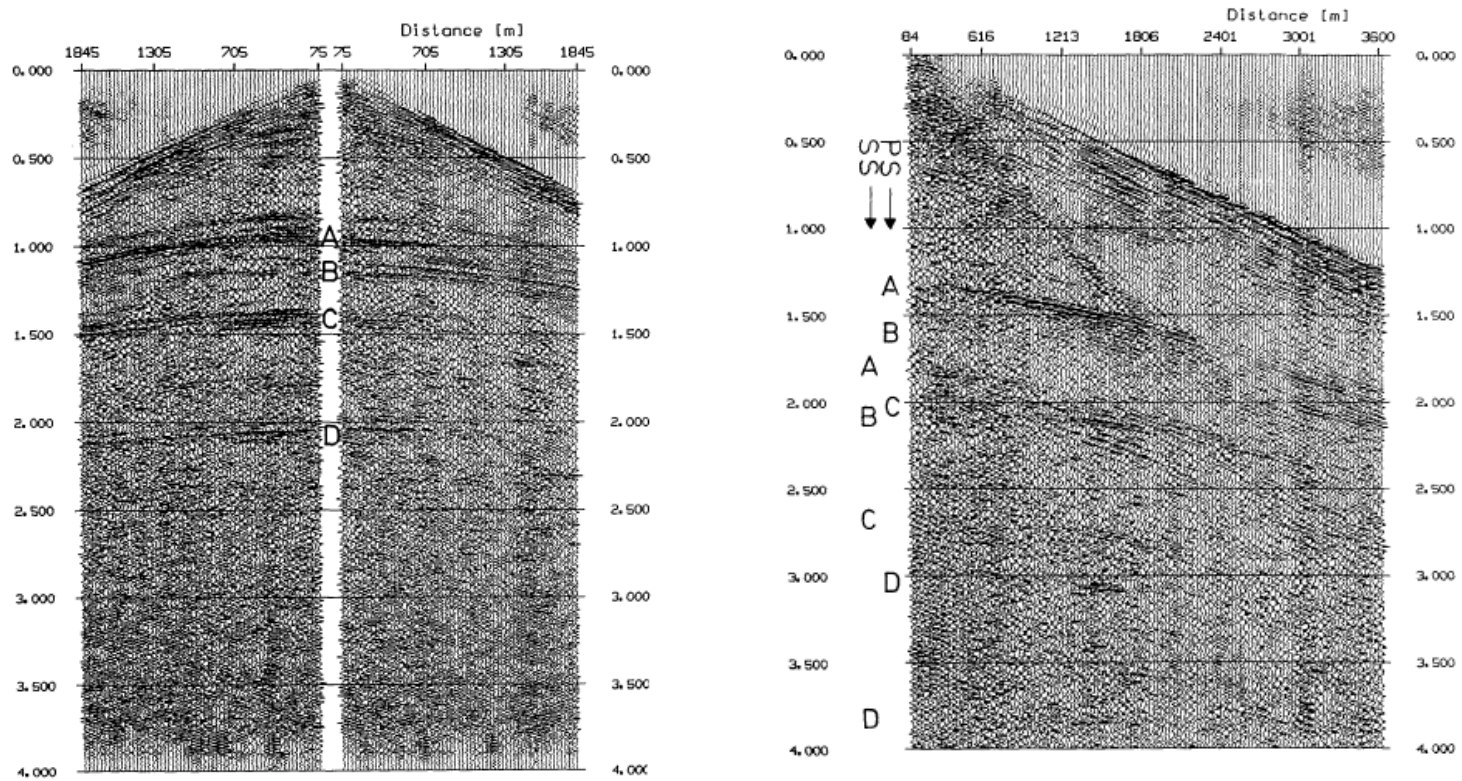


Figure 1.13 – A P-wave shot record showing 4 major stratigraphic events, A through D (left). Converted wave shot record corresponding to the section in Figure 1.5 showing the seismic events A through D for the PS and SS modes (right). Note the travel time differences between the events for the different mode converted data. (from Fertig & Krajewski, 1989)

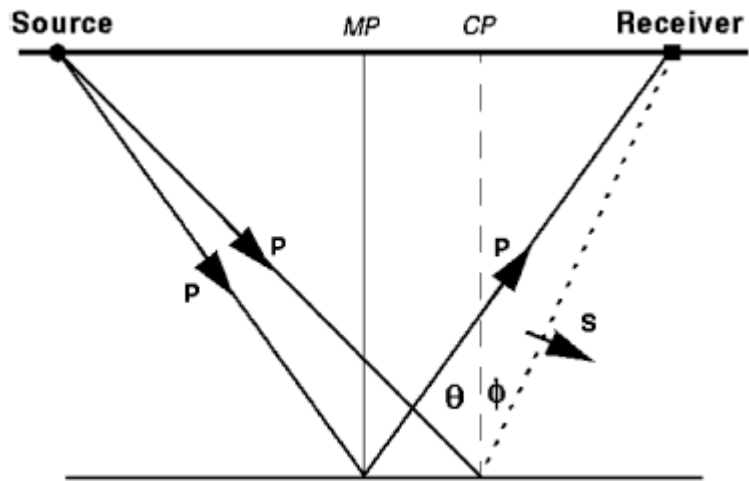


Figure 1.14 – A P-wave and PS wave reflection in a single homogeneous, isotropic layer. Note the converted wave reflects at its conversion point (CP) and the conventional P-wave reflects at a midpoint (MP). The arrows show direction of particle motion for each downgoing and upgoing wave mode. (from Stewart, 2002)

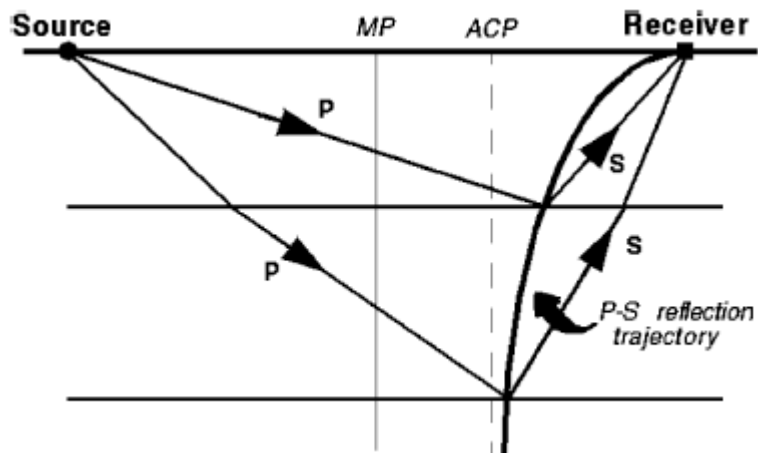


Figure 1.15 – The conversion point of a P-S reflection approaches the asymptotic conversion point (ACP), away from the receiver, as depth increases. The ACP is generally between the receiver and the midpoint (MP) of a conventional P-wave reflection profile. (from Stewart, 2002)

## Chapter Two: TRAVEL-TIME ANALYSIS

### 2.1 Introduction

Fractures reduce the cohesion within the rock perpendicular to the direction of fracture propagation. Seismic waves propagating parallel to the fracture will not experience any change in velocity, whereas a seismic wave propagating perpendicular to the direction of fracture propagation will experience a decrease in velocity (Lynn et al., 1999; O'Connell & Budiansky, 1974; Ruger, 1997). Such velocity anomalies are referred to as transverse isotropy (Thomsen, Weak Elastic Anisotropy, 1986), and are evident through the travel-time analysis of seismic events which travel at orthogonal source-receiver ray paths. In this study area, where fractures are 20-30 degrees subvertical (Boyd Personal Communication), and the surrounding carbonate stratigraphy is relatively flat, seismic waves are likely to experience a specific type of anisotropy called horizontal transverse isotropy, or HTI (Figure 2.1) (Hudson, 1981; Tsvankin, 1997).

The presence of HTI allows for the analysis of travel-time differences between orthogonal azimuths. In order to do so, the PP and PS datasets were divided into 5 volumes; one full azimuth stack volume and four azimuthally sectorized volumes containing a stack encompassing a 45 degree aperture of reciprocal source-receiver ray paths. These volumes are centred around 0&180, 90&270, 45&225 and 135&335 degrees (Figure 2.2). In order to detect possible HTI, five horizons were picked in each of the volumes: the Birdbear Formation, the Souris River Formation, the Dawson Bay Formation, the Prairie Evaporite Formation and the Winnipegosis Formation.

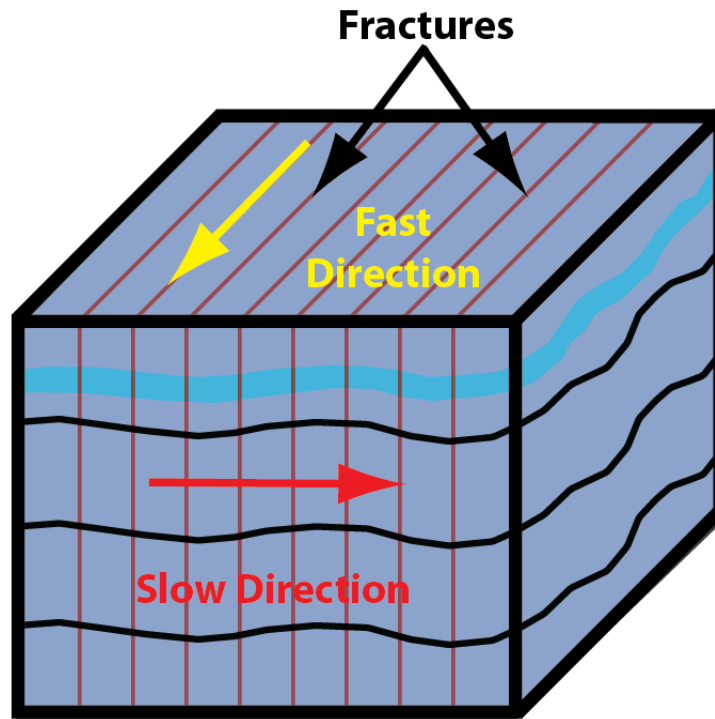


**Figure 2.1 – Schematic diagram showing the fast and slow directions of seismic wave propagation with respect to fractures in the subsurface. The vertical fractures induce a reduction in seismic velocity perpendicular to the orientation of fracturing, whereas the seismic velocity parallel to fracturing is unchanged.**

The effects of HTI induced from subsurface fracturing should be visible in the four sub-volumes due to the small changes in residual normal move-out (NMO) between azimuthal gathers using full-azimuth velocities. The changes in residual NMO propagate into the azimuthally sectorized stacks and yield small travel-time differences in the stacked seismic events when the global NMO velocities are applied to the sectorized volumes (Figure 2.3).

Travel-time differences were calculated by subtracting horizons picked from two orthogonal azimuthally sectorized volumes centred around 0&180 degrees (A) and 90&270 degrees (C). Should the travel-time from A be larger than that of C, the outcome is a

positive time difference which would propose a slower seismic velocity in the A orientation. A negative time difference suggests a slower seismic velocity in the C orientation. This process is then repeated for 45&225 degrees (B) and 135&335 degrees (D).

Before travel-time differences can be calculated, seismic horizons were first tied to geological formations through the well tie process.

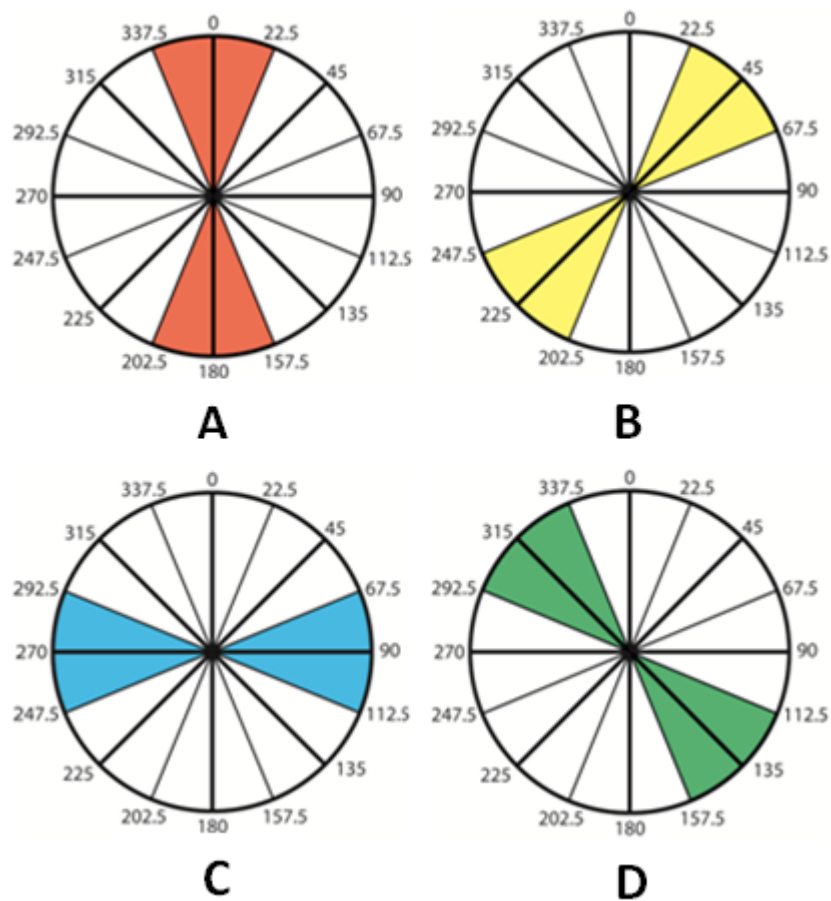


**Figure 2.2 – Distribution of source-receiver ray paths used to make up the four azimuthally sectored seismic volumes. The volumes are labeled corresponding to the reciprocal azimuths in the middle of the stacked aperture.**

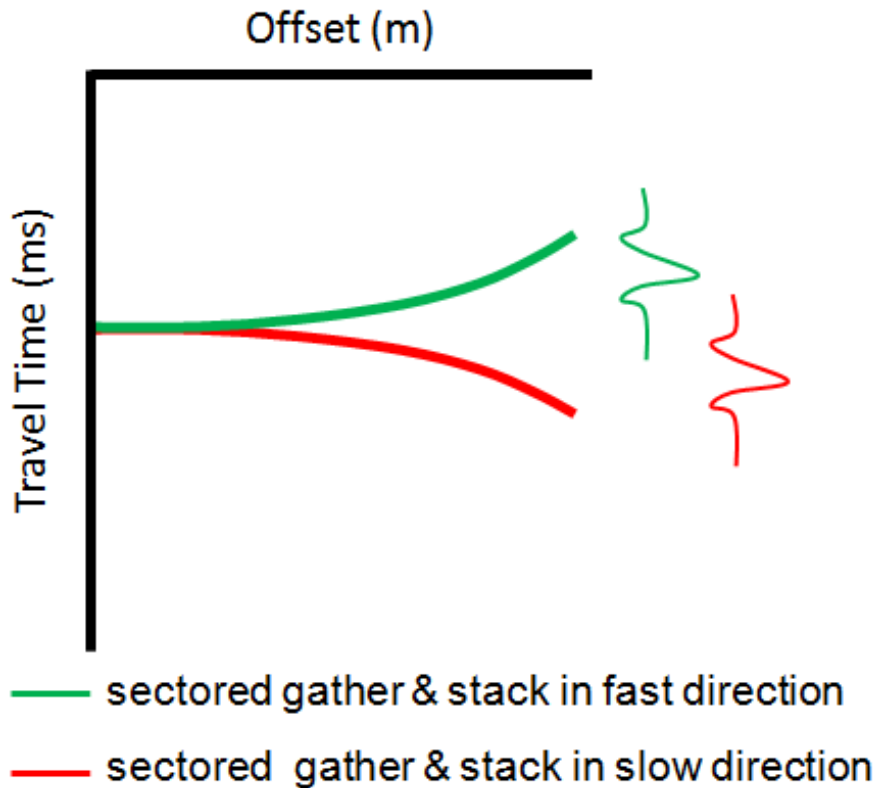


**Figure 2.3 – Residual NMO from the sectored receiver gathers and stacks corresponding to the directions of fast (green) and slow (red) seismic wave propagation, as well as the travel-times associated with those azimuthally sectored stacks.**

## 2.2 Horizon Interpretation

In order to begin analysis of a seismic volume, the subsurface formations were first correlated to the corresponding time on a seismic section. This is done through the generation of synthetic seismograms using P- and S- wave sonic and density wireline logs which are typically acquired when a well is drilled. In the study area there were 14 wells with P-wave sonic logs, 2 wells with dipole sonic logs, which provide the S-wave velocity component, and 3 wells with density logs. Figure 2.4 shows blocked wireline logs from one of the wells used pick horizons on both the PP and PS data sets. The selection of seismic

events which correspond to stratigraphic layers is crucial to the interpretation of a seismic dataset, and is accomplished by relating geological well tops to seismic reflectors through the generation of synthetic seismograms. The critical formations for the interpretation of this volume are the Birdbear Formation, the Souris River Formation, the Dawson Bay Formation, the Prairie Evaporite Formation and the Winnipegosis Formation, some of which are not shown on the log.

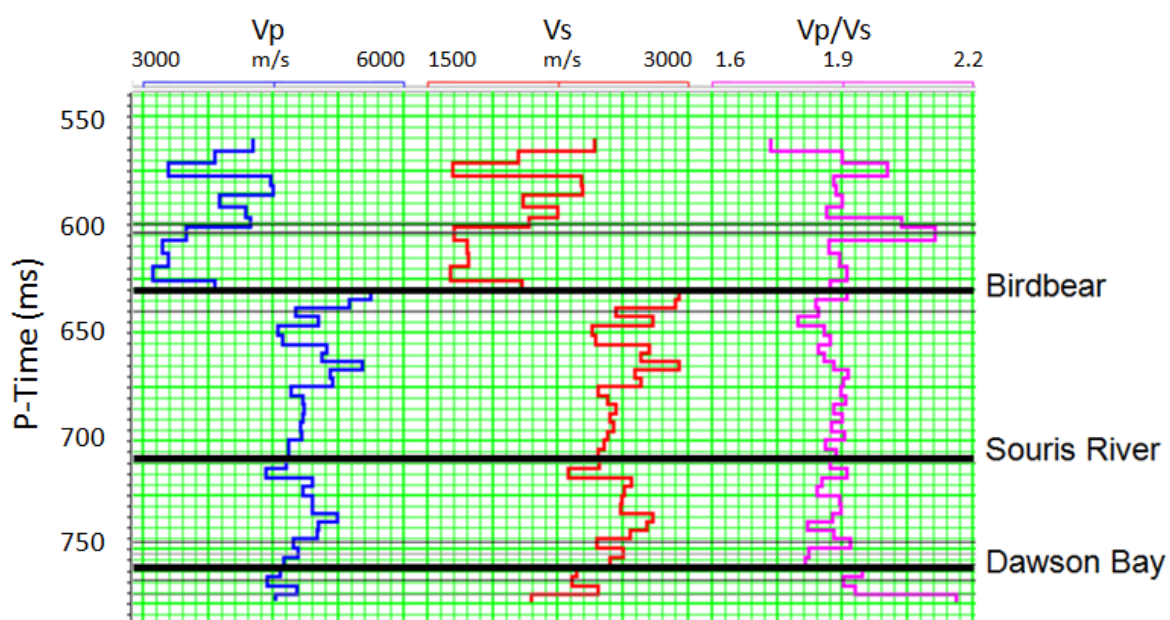


**Figure 2.4 - Blocked wireline logs acquired from one of the wells in the study area. The P-wave sonic is in blue, S-wave sonic in red and Vp/Vs calculated from both sonic logs in magenta. The geological tops are in black.**

Correlation between the synthetic seismogram and the seismic volume is calculated at the well bore to ensure an accurate assessment of the horizons to be interpreted. Figure 2.5 is an example of a synthetic seismogram generated and its correlation, of 0.806, with the baseline PP seismic volume. All 14 wells were tied in similar fashion and yielded similar correlation coefficients. The tying of the PS seismic is done using synthetic seismograms,

in which reflection coefficients calculated from both the P-wave and S-wave sonic logs, are convolved with a wavelet representative of the seismic traces. An additional step factors in the  $V_p/V_s$  to adjust the time-depth relationship accordingly. The two wells with dipole sonic wells were tied with only minor stretches applied to attain an optimal correlation of 0.685 (Figure 2.6).

The Prairie Evaporite and Winnipegosis formations are not seen as geological tops on the well logs in the area. This is because the wells are specifically planned not to penetrate the Prairie Evaporite Formation, and therefore this top was slightly more difficult to pick. The Prairie Evaporite Formation was picked in the PP seismic volumes based on the termination of the well log, and the location of the potash mine workings which are visible in the seismic volumes.

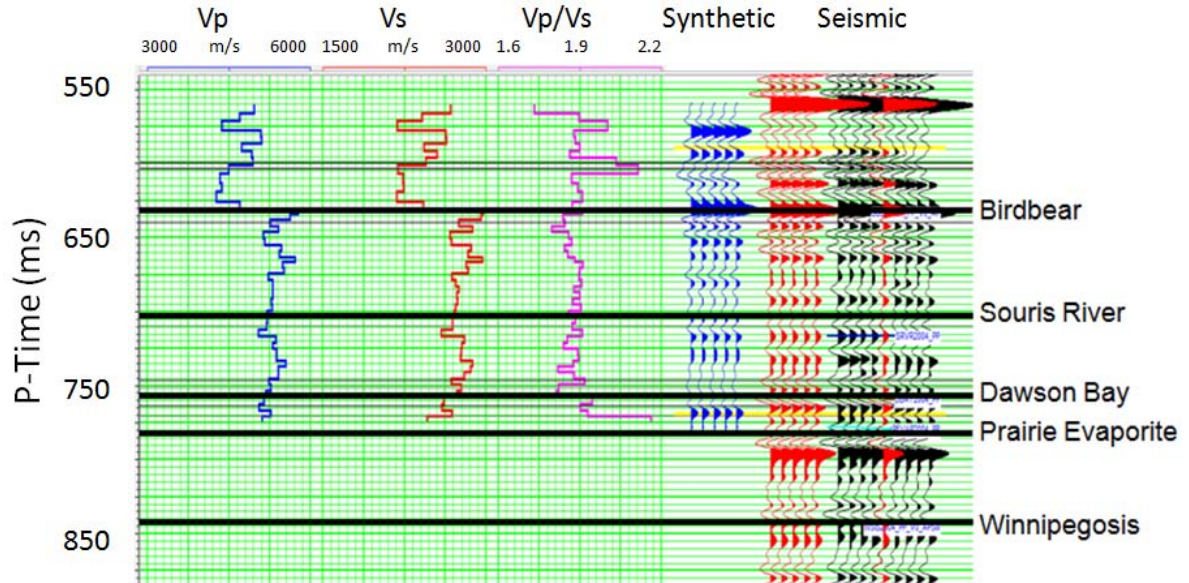


**Figure 2.5 – PP synthetic seismogram (blue seismic traces) constructed using the P-wave sonic (blue log) and is correlated with the baseline PP seismic volume (red/black seismic traces).**

The Winnepegosis Formation was picked in the baseline and monitor PP and PS volumes through the identification of what is interpreted to be a carbonate mound in the Southeast and a pinnacle reef in the northeast of the survey area.

Time structure maps were created through interpretation of the 5 horizons of interest for both the baseline and monitor surveys on both PP and PS volumes. Analysis of these horizons, the seismic volumes and the geological information conveyed by RPS Boyd (Boyd Personal Communication) suggests that fractures could be the cause of the low velocity anomaly in the centre of the study area, the extent of which is shown as a “push down” (an increase in travel-time) in Figure 2.7. In both PP volumes, the low velocity anomaly is also accompanied by an overall reduction in seismic amplitude (Figure 2.8). In the PS volumes however, the seismic amplitudes are unaffected.

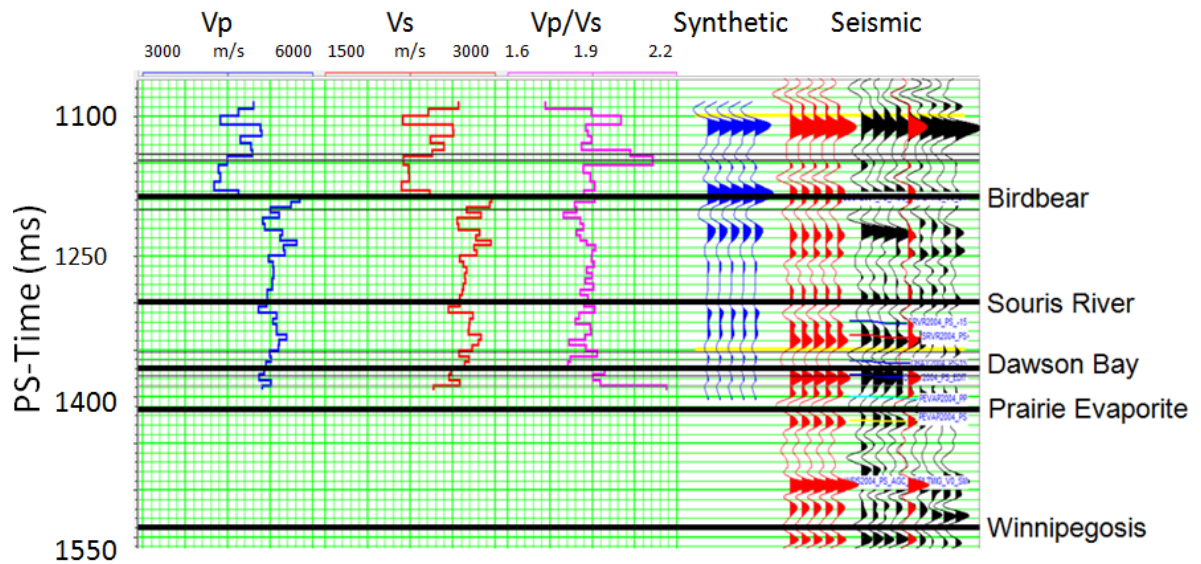


**Figure 2.6 – PS synthetic seismogram (blue seismic traces) constructed using the P-wave sonic (blue log), the S-wave sonic (red log) and the Vp/Vs (magenta log) is used to apply a velocity stretch before the synthetic is tied with the baseline PS seismic volume (red/black seismic traces).**

The PS dataset has a lower frequency content, and is noisier than the PP dataset (Figure 2.9). As a result, the PS horizons were much more difficult to pick than the PP horizons. However, the use of azimuthal travel-time analysis for both the PP and PS seismic volumes was applied to investigate the presence of seismic anisotropy in the subsurface.

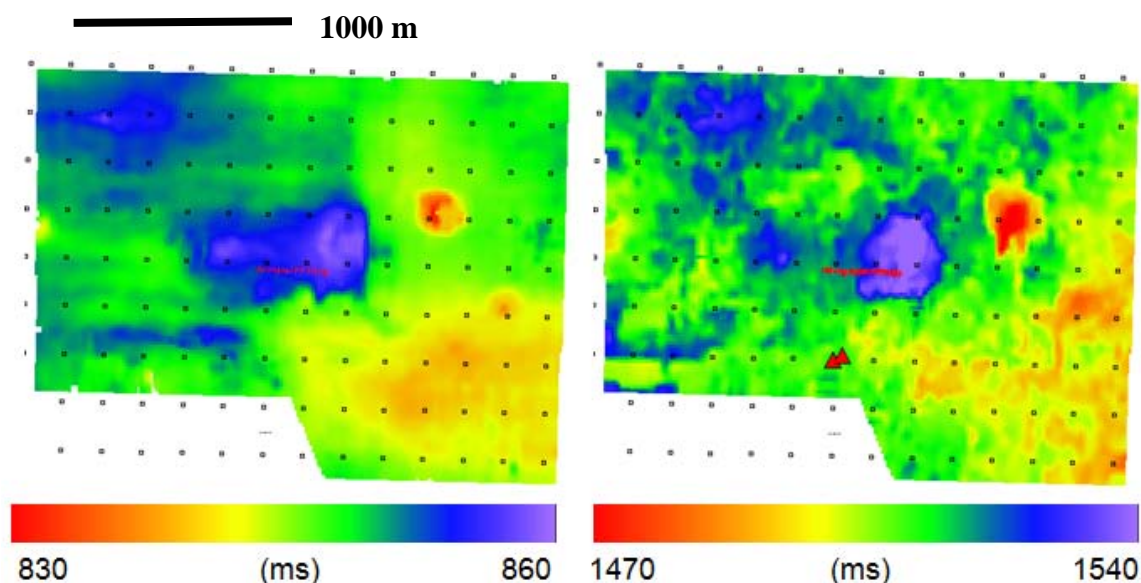


**Figure 2.7 – Time structure maps showing the Winnipegosis Formation from the baseline PP seismic volume (left) and baseline PS seismic volume (right). The large blue-purple anomaly in the centre of the map shows a travel-time “push down” which is thought to be attributed to the presence of fractures in the carbonate layers above the Prairie Evaporite Formation. The red circle in the Northeast corresponds with an interpreted pinnacle reef, and the yellow-red in the Southeast shows the outline of an interpreted carbonate mound.**

### 2.3 PP Travel-time Analysis

The Souris River Formation shows minimal travel-time differences that are between -5 and +5 ms in the baseline and monitor PP volumes (Figure 2.10 and Figure 2.11). There are few major differences between the baseline and monitor vintages, which illustrates

survey repeatability. The Prairie Evaporite PP time difference plots shows evidence of the mine workings southeast of the study area in the A-C orientation plots (Figure 2.12 and Figure 2.13).

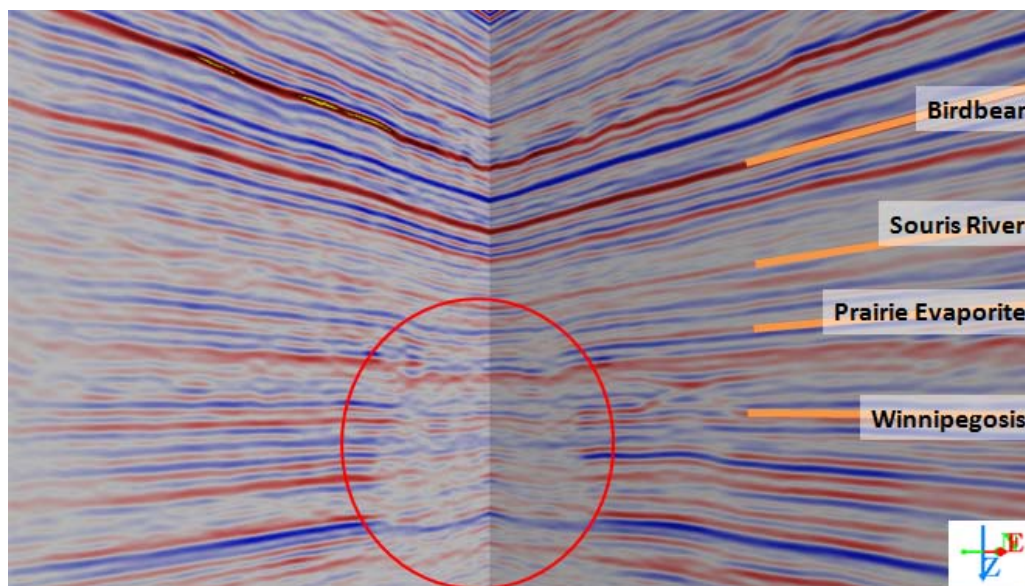


**Figure 2.8 – An inline and crossline from the baseline PP volume displaying the low amplitude, low velocity anomaly at the centre of the study area (red circle). The anomaly propagates below the Souris River Formation to the bottom of the section.**

The large negative travel-time difference in the southeast of the survey area is attributed to mine workings in the C orientation which creates a reduction in seismic velocity due to the open mine rooms with the same orientation. The monitor A-C azimuthal PP time difference plot also shows a travel-time difference of +7 ms towards the centre of the study area. The B-D plots (Figure 2.13) show much less detail because of the trend of the mine workings. The large negative anomaly in the centre of the study area is at the eastern-most edge of the workings which trend east to west. Overall there are minimal travel-time differences between the baseline and monitor surveys in the B-D azimuthal time difference plots.

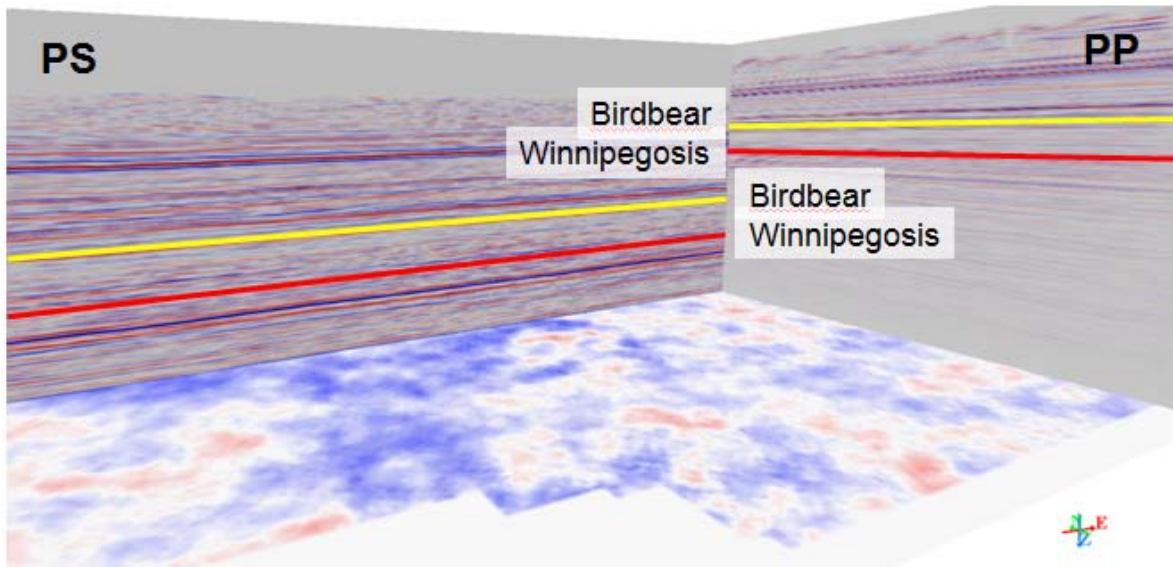


Figure 2.9 – Chair display showing an inline through the baseline PP volume (right) and the baseline PS volume (left). This figure emphasizes the travel-time differences between the PP and PS volumes, as well as the lower frequency content and higher noise levels in the PS volume.

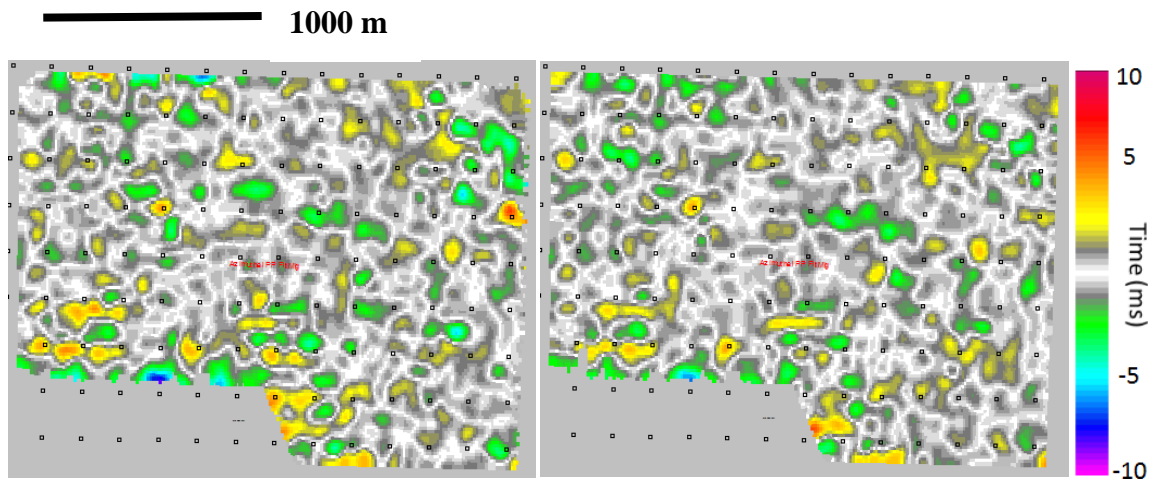
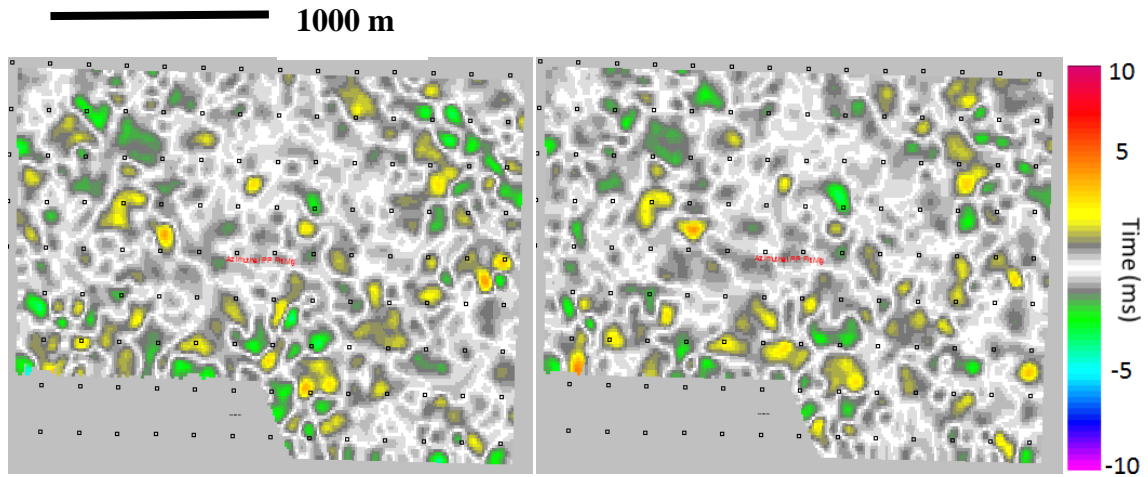
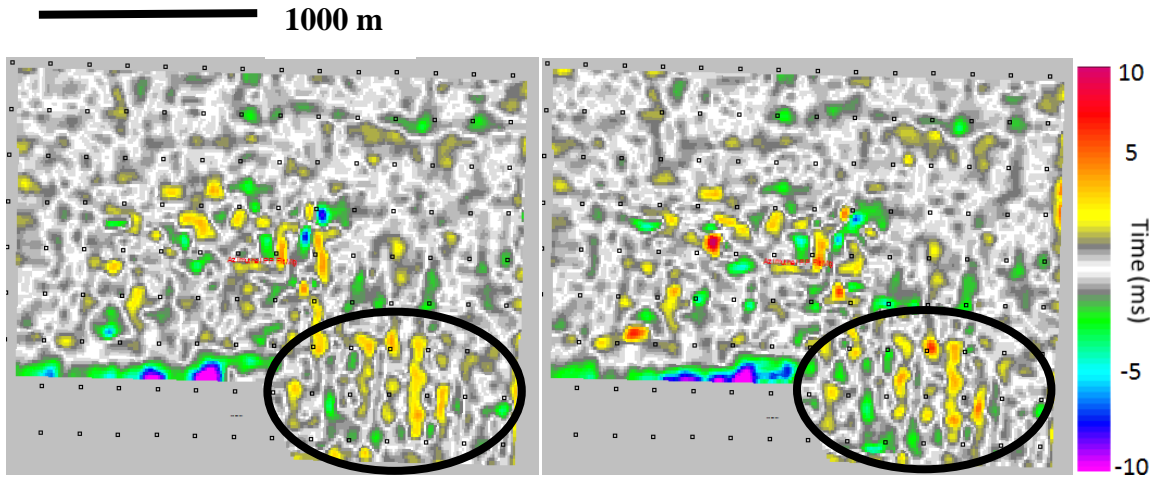


Figure 2.10 – PP time difference plots for the Souris River Formation calculated by subtracting the A-C azimuths for the baseline (left) and monitor (right) seismic volumes.



**Figure 2.11 – PP time difference plots, for the Souris River Formation, calculated by subtracting the B-D azimuths for the baseline (left) and monitor (right) seismic volumes.**

The PP time difference plots calculated for the Winnipegosis Formation horizons from the difference azimuths show much larger variations in travel time between orthogonal azimuths, especially in the central section of the study area (Figure 2.14). The main anomalies of interest are as large as +10 ms. The southern-most positive differences in the A-C plot (Figure 2.14) indicates a low north-south velocity, which if created by fractures, suggest that the fractures trend in an east-west orientation. The western area positive travel-time anomaly increases in magnitude between the baseline and monitor surveys. The northeastern positive anomaly is connected with the most southeastern anomaly at the easternmost edge of the mine workings in the centre of the study area. Just beyond the eastern edge of mine workings, a negative travel-time anomaly is present, albeit much larger in amplitude in the monitor survey (black ellipses).



**Figure 2.12 – The baseline (left) and monitor (right) A-C azimuth PP time difference plots for the Prairie Evaporite Formation, showing mine workings in the southeast corner of the map (black ellipses).**

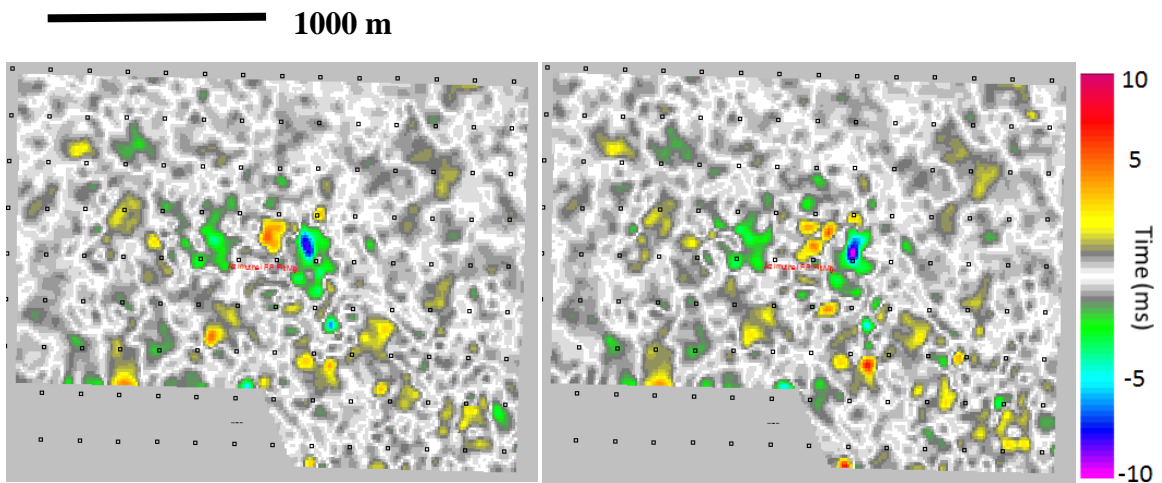


**Figure 2.13 – The baseline (left) and monitor (right) B-D azimuth PP time difference plots for the Prairie Evaporite Formation.**

In the B-D Winnipegosis PP time difference plots (Figure 2.15), the most positive travel-time anomaly corresponds with a large, positive travel-time anomaly from the A-C

Winneposis time difference plots (black ellipses). The blue negative anomaly towards the west of the central anomaly is located in the centre of the mine workings.

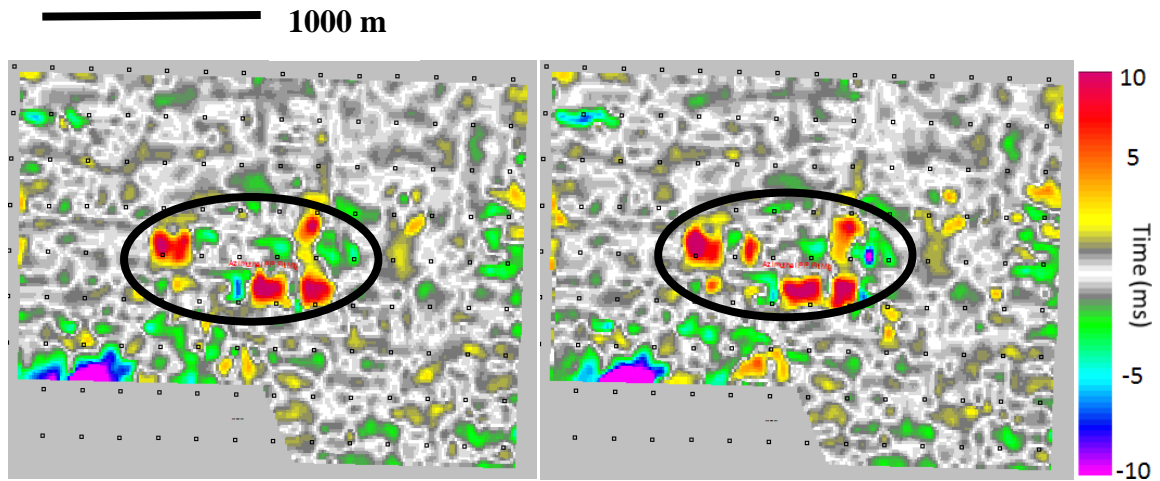


**Figure 2.14 – The baseline (left) and monitor (right) A-C azimuth PP time difference plots for the Winneposis Formation.**

#### **2.4 PS Travel-time Analysis**

The range of travel-time differences calculated using the PS horizons, as expected, is significantly larger than the travel-time differences calculated from the PP horizons. As in the PP time difference plots, the Souris River horizons do not yield any significant anomalies; they do however, show a much more uniform negative overall difference in the A-C azimuths (Figure 2.16).

There also appear to be some differences in travel-time between the baseline and monitor PS time difference plots which have a good correlation to the east of the study area, but not in the west, similar to the B-D azimuth PS time difference plots (Figure 2.17).

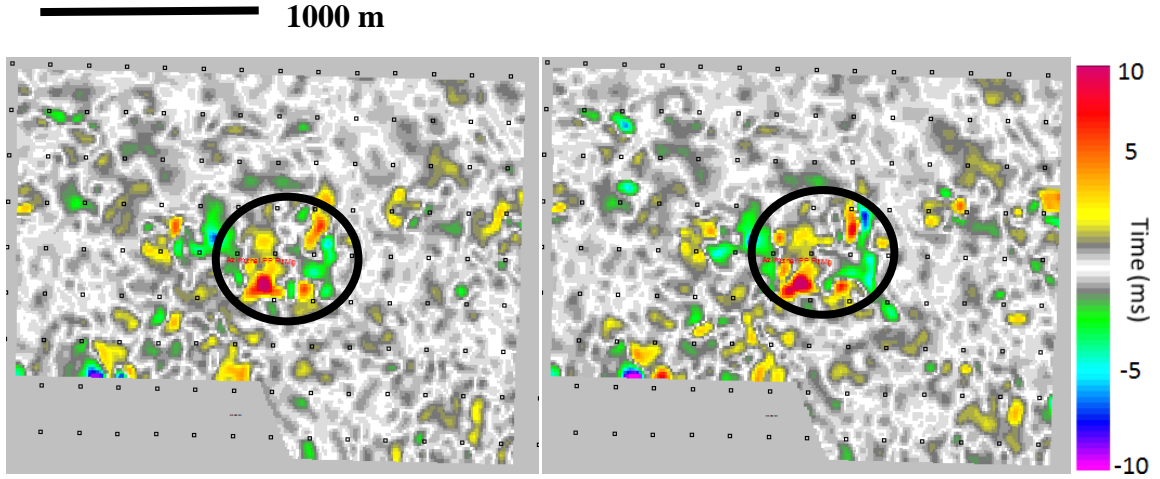


**Figure 2.15 – The baseline (left) and monitor (right) B-D azimuth PP time difference plots for the Winnipegosis Formation.**

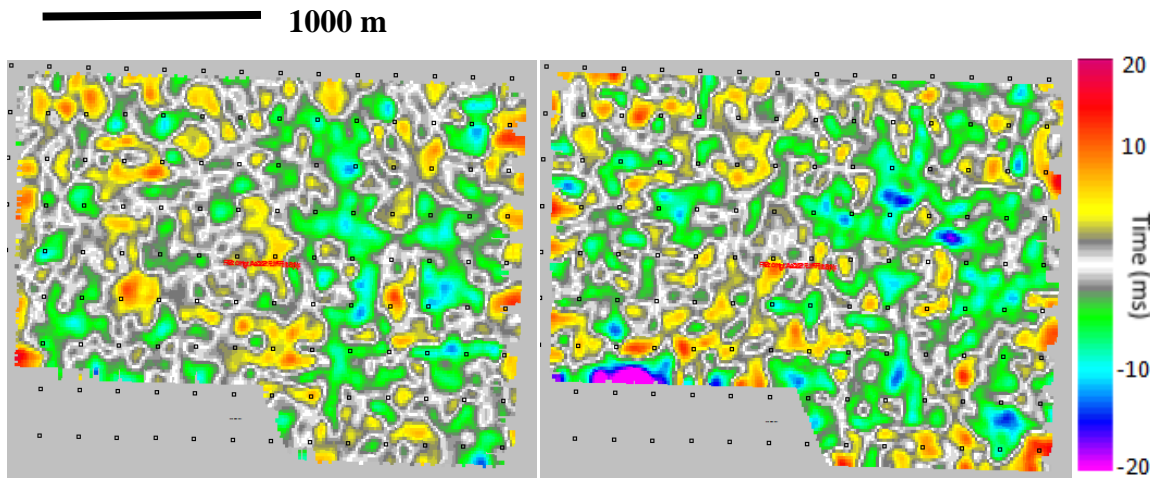


**Figure 2.16 – The baseline (left) and monitor (right) A-C azimuth PS time difference plots for the Souris River Formation.**

The Prairie Evaporite A-C azimuth PS time difference plot from the monitor volume (Figure 2.18) shows a large negative travel-time difference, which was not present in the baseline PS time difference plot (black circle). This indicates a seismic velocity reduction in the C orientation towards the eastern edge of the central mine workings. The large negative travel-time differences on the eastern edge of the survey increase in magnitude

between the baseline and monitor survey, where mine workings line the outermost edges of the survey area. This increased travel-time anomaly could be a result of subsurface stress changes induced by the presence of the mining operations which creates fractures parallel to the north-south oriented mine rooms and thus reduces the seismic velocity in the east-west orientation.

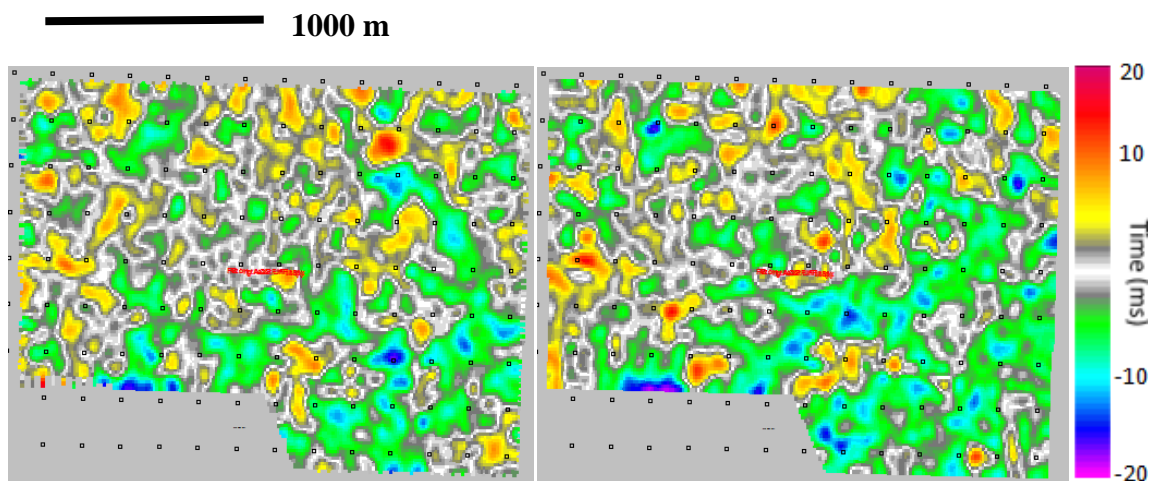


**Figure 2.17 – The baseline (left) and monitor (right) B-D azimuth PS time difference plots for the Souris River Formation.**

This is supported by the reduced magnitude of the travel-time anomaly in the B-D azimuth PS time difference plots (Figure 2.19). However, a slight increase in negative travel-time difference is present where some A aligned mine workings intersect those at a C orientation (centre of eastern edge of survey).

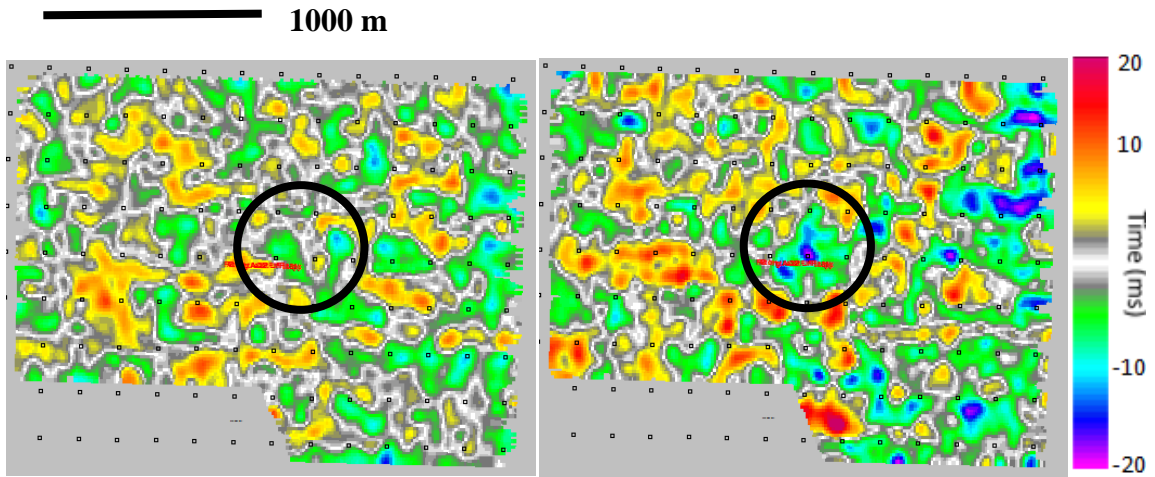


**Figure 2.18 – The baseline (left) and monitor (right) A-C azimuth PS time difference plots for the Prairie Evaporite Formation. The black circle indicates a large negative travel-time difference in the monitor volume, not present in the baseline.**

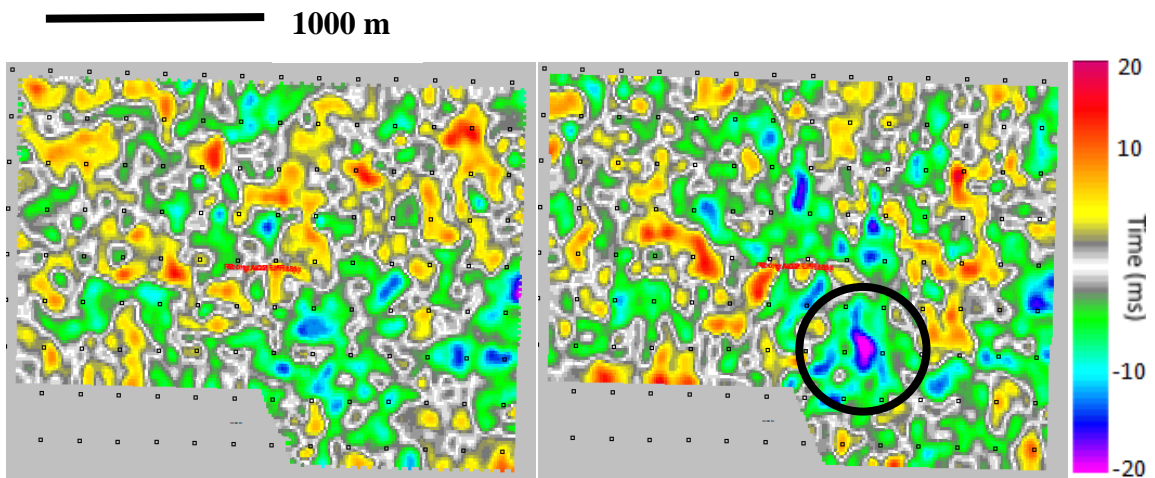


**Figure 2.19 – The baseline (left) and monitor (right) B-D azimuth PS time difference plots for the Prairie Evaporite Formation. The black circle indicates a large negative travel-time difference in the monitor volume, not present in the baseline.**

The Winnipegosis Formation shows a high positive travel-time anomaly on the west side of the baseline A-C azimuth PS time difference plot (Figure 2.20), which is not present in the corresponding monitor map. The largest positive and negative anomalies in the centre of the dataset correspond to the edges of the central mine workings; furthermore the

orientation of slow seismic wave propagation in the PS time difference plots are identical to those in the PP time difference plots (Figure 2.14). The travel-time anomalies in the northeast of the baseline A-C azimuth time difference plot are in the area of the interpreted pinnacle reef, where the Winnipegosis reef in the A volume appears wider than in the C volume creating a negative travel-time difference on the edges of the interpreted reef. B-D azimuth time difference plots (Figure 2.21) show an increase in the positive anomaly to the east of the central mine workings in the monitor survey which is not present in the baseline survey. The monitor survey also sees an increase in the magnitude of the negative travel-time anomaly in the southeast of the study area.

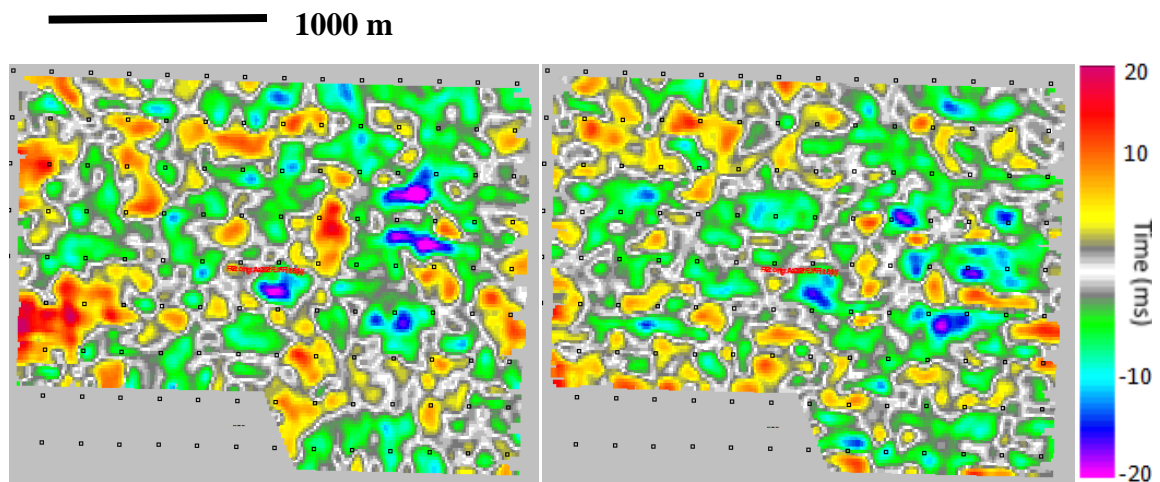


**Figure 2.20 – The baseline (left) and monitor (right) A-C azimuth PS time difference plots for the Winnipegosis Formation.**

## 2.5 Summary

This chapter has shown the analysis of azimuthal travel-times from PP and PS seismic volumes by horizon differencing in order to examine possible fracture systems surrounding a potash mine in southeast Saskatchewan, Canada. In particular, the goal of

this work was to interpret the effect of fractures within the Dawson Bay Formation through the calculation of travel-time differences between seismic events in volumes which were created using a stack of sectorized, orthogonal source-receiver azimuths. This is made possible because fractures reduce the velocity of seismic waves traveling across the fracture plane, creating a state of HTI, which can be identified due to the increase of event travel-time isolated to the azimuths perpendicular to fracture strike. Interpretation of the time difference plots created from the seismic events picked in the multiple azimuthally sectorized PP and PS volumes provided insight into the state of anisotropy in the subsurface.

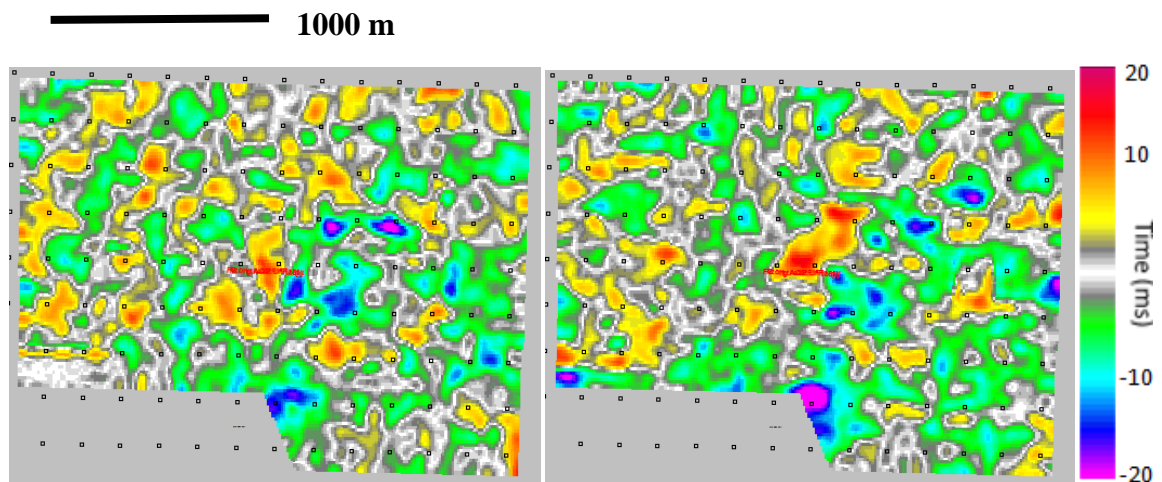


**Figure 2.21 – The baseline (left) and monitor (right) B-D azimuth PS time difference plots for the Winnipegosis Formation.**

Analysis of the PP time difference plots shows that fractures with a preferential orientation propagate outwards from the mining area in a direction parallel to the mine room geometry, specifically below the mine in the Winnipegosis Formation. Above the mining level, in the Dawson Bay Formation, the PP time difference plots show a reduction of seismic velocity in the C direction suggesting that fractures are propagating parallel to

the eastern edge of the central mining operation. Although fractures are likely to be present throughout the excavation area, they are interpreted to have no preferential orientation which results in a reduction of seismic velocity in all directions. Therefore the fractures do not induce a large enough seismic anisotropy to be visible in the PP time difference plots focusing on orthogonal azimuths of wave propagation. The monitor PS time difference plots also produced a large negative travel-time anomaly in the Prairie Evaporite Formation A-C sectors, at the edge of the mining area, which was not present in the baseline survey. These observations suggest that there is fracturing surrounding the mine workings which creates HTI, identified through azimuthal travel-time analysis.

## Chapter Three: VELOCITY ANALYSIS

### 3.1 Introduction

Where fractures are present in the subsurface,  $V_p/V_s$  will increase depending on fracture density, as the P-wave velocity will generally exhibit a lower percentage decrease than the S-wave velocity (Hardage, DeAngelo, Murray, & Sava, 2011; O'Connell & Budiansky, 1974). In order to determine the relative extent of fracturing in the subsurface, analysis of  $V_p/V_s$  was undertaken using the picked horizons from the PP and PS full azimuth volumes. To visualize the vertical changes in  $V_p/V_s$  throughout a seismic volume, horizon matching was performed in which travel-times associated with each point of a PS horizon were shifted to match that of the corresponding PP horizon. Using Equation 3.1,  $V_p/V_s$  is calculated:

$$\frac{V_P}{V_S} = \frac{2\Delta t_{PS} - \Delta t_{PP}}{\Delta t_{PP}} \quad (3.1)$$

Where  $V_p$  is the P-wave velocity,  $V_s$  is the S-wave velocity,  $\Delta t_{PS}$  is the PS travelttime and  $\Delta t_{PP}$  is the P-wave travelttime. Where well control is present,  $V_p/V_s$  is within reasonable values for carbonates (Palaz & Marfurt, 1997; Mavko, 2005).

### 3.2 $V_p/V_s$ Analysis

In order to perform a thorough  $V_p/V_s$  analysis, a background ratio of P-wave velocity to S-wave velocity must first be established. This was done during the registration process when horizons were placed in their appropriate temporal locations on both the PP and PS seismic sections (Figure 3.1). The squeezing of the PS seismic section to match that of the PP section is governed by  $V_p/V_s$ . By matching the horizons picked on the PS section to those on the PP section it was possible to determine an appropriate background  $V_p/V_s$  to

begin the horizon matching process. This ratio was determined to have an initial value of 2.0 (Figure 3.2) which is higher than the  $V_p/V_s$  seen in the well logs (Figure 2.4). The  $V_p/V_s$  is higher because the seismic takes into account the  $V_p/V_s$  of the entire seismic section including the Cretaceous shales ( $V_p/V_s$  of 2.1) and the weathered layer ( $V_p/V_s$  of 4.0-6.0).

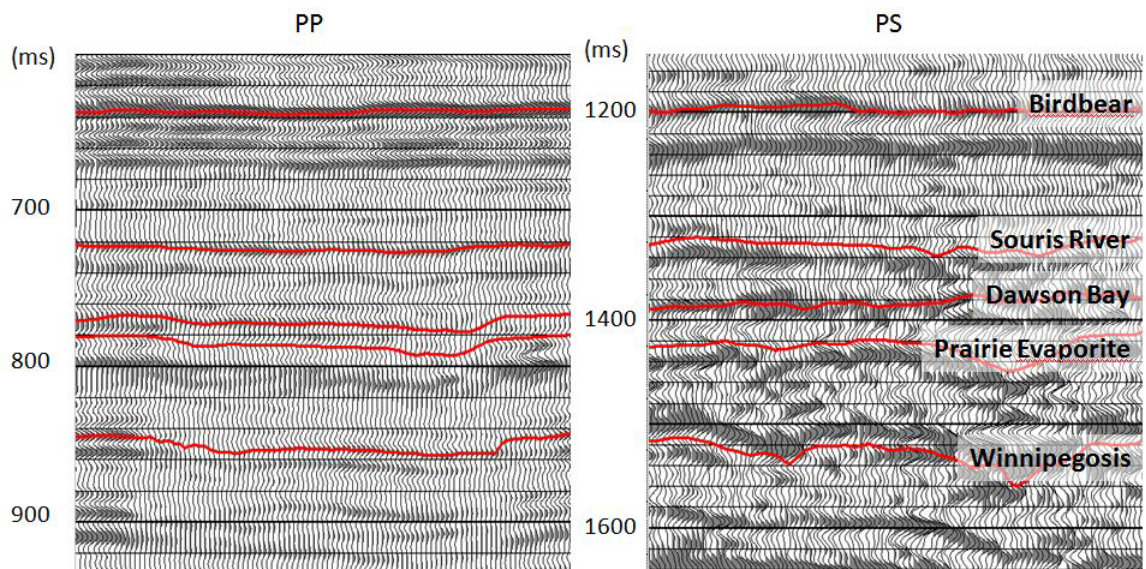


**Figure 3.1 – Crossline showing five major horizons picked in the PP (left) and PS (right) seismic volumes through the low velocity, low amplitude anomaly in the centre of the dataset. The PS volume is compressed using a  $V_p/V_s$  of 2.0 to best match the placement of each horizon with their PP counterpart.**

The first horizons to be matched were those of the Birdbear Formation (yellow horizon) from the baseline seismic volume. The matching of this event established  $V_p/V_s$  for the stratigraphy above the level of interest and is influenced by the near surface, unconsolidated layers, which increases the  $V_p/V_s$  to approximately 2.7 (top of Figure 3.3).

When the Souris River Formation (green horizon) was added to the horizon matching process, interval  $V_p/V_s$  was calculated for the interval from the top of the Birdbear

Formation to the top of the Souris River Formation (Figure 3.4). The  $V_p/V_s$  values in this plot are strictly associated with the PP and PS horizons and are calculated using Equation 3.1. The vertical striping seen is a function of the slight vertical changes in the travel-time picks of both the PP and PS horizons with respect to each other, as any slight travel-time difference between the two horizons will result in a change in  $V_p/V_s$  for that point in the survey. The magnitude of the vertical striping changes from line to line (see the top and bottom lines in Figure 3.4) and between the baseline and monitor surveys, but is present throughout the horizon matching process. The  $V_p/V_s$  for this interval throughout the baseline survey ranges between 1.65 and 2.4 with an average value of 1.9, which is appropriate for the carbonaceous Birdbear Formation.

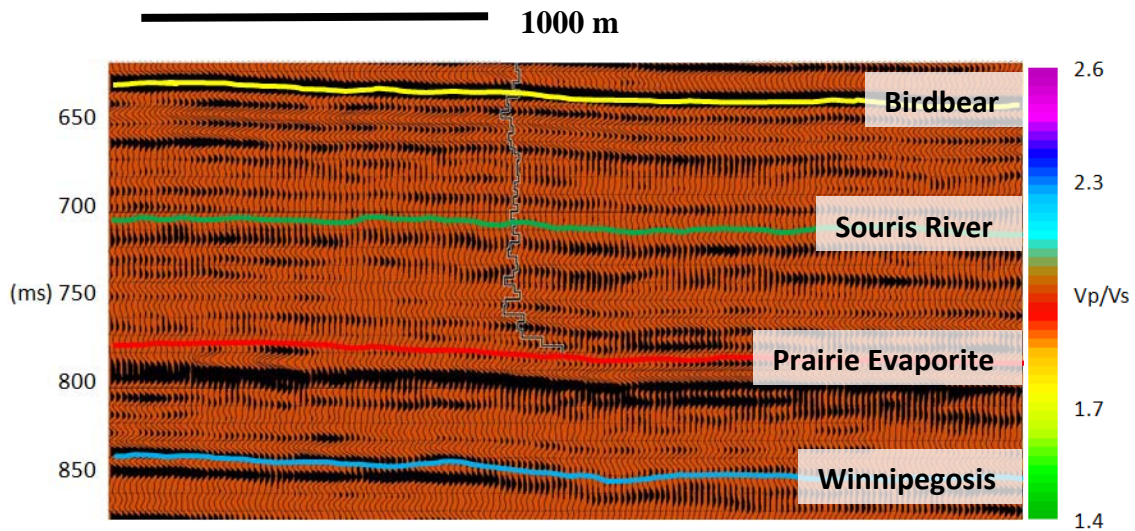


**Figure 3.2 – Crossline from the baseline seismic volume through one of the wells containing a dipole sonic log.  $V_p/V_s$ , shown in color, is set to the background  $V_p/V_s$  of 2.0 determined from the registration process. The horizons from top to bottom are the Birdbear Formation (yellow), Souris River Formation (green), Prairie Evaporite Formation (red) and Winnipegosis Formation (blue).**

Including the Prairie Evaporite Formation (red horizon) in the matching process provided  $V_p/V_s$  for the interval from the top of the Souris River Formation to the top of the Prairie Evaporite Formation, which encompasses the fractured carbonates of the Dawson Bay Formation.

In Figure 3.5, the interval between the green and red horizons shows distinct differences between a crossline outside the low velocity, low amplitude anomaly (upper) and the line inside the low velocity, low amplitude anomaly (lower), specifically, the magnitude of the interval  $V_p/V_s$  is higher through the anomaly than it is outside the anomaly. Within the anomaly,  $V_p/V_s$  ranges from 1.8 to 2.3 and between 1.7 and 2.1 outside the anomaly. The two areas of  $V_p/V_s$  between 2.0 and 2.3 through the low velocity, low amplitude anomaly have been interpreted to be the result of fracturing in the Dawson Bay Formation.

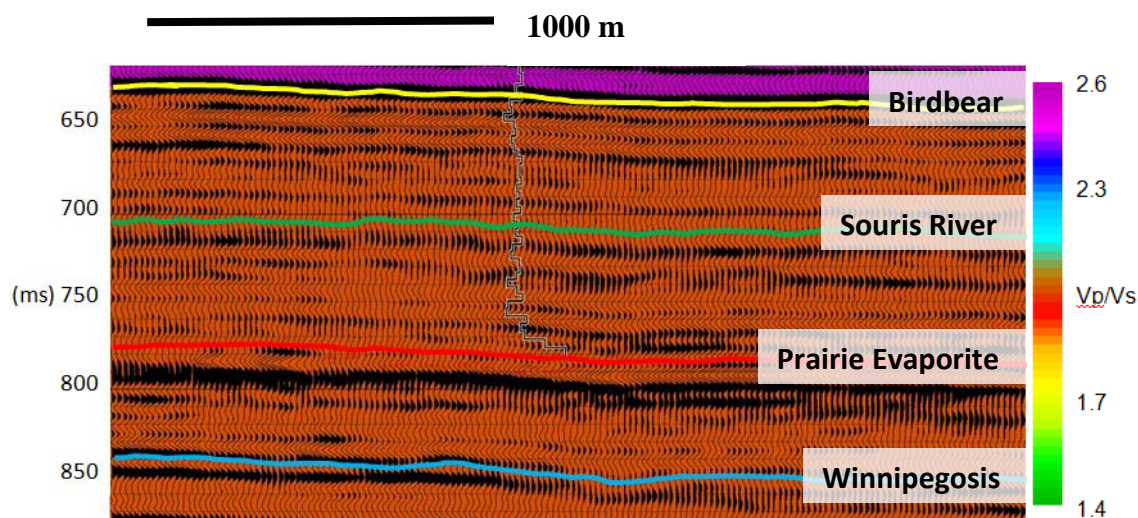


**Figure 3.3** – Crossline from the baseline seismic volume through a well with dipole sonic log. The Birdbear PP and PS horizon matching has been applied generating the high  $V_p/V_s$  at the top of the section. This increased  $V_p/V_s$  at the top of the section is due to the high  $V_p/V_s$  of the overburden.

The final horizons added to the procedure correspond to the top of the Winnipegosis Formation (blue horizon). The  $V_p/V_s$  of the Prairie Evaporite interval increases significantly when comparing values between crosslines inside and outside of the central anomaly (Figure 3.6). The crossline through a well outside of the anomaly (top Figure 3.6) shows an average  $V_p/V_s$  around 1.9, whereas the line through the anomaly (bottom Figure 3.6) has an average  $V_p/V_s$  of 2.2. Adding the Winnipegosis Formation to the analysis completed the horizon matching process, through the use of only PP and PS traveltimes. In order to create a more complete  $V_p/V_s$  volume, the  $V_p/V_s$  calculated from the dipole sonic logs was assigned as a background  $V_p/V_s$  instead of the uniform  $V_p/V_s$  of 2.0 used up to this stage of the analysis.

This improves the accuracy of the  $V_p/V_s$  analysis in the areas closest to the well (Figure 3.7) as the vertical resolution of a well log is much better than that from the seismic volumes. The  $V_p/V_s$  was calculated using the P-wave and S-wave sonic logs which were blocked into 10 m intervals in order to complement the vertical resolution of the seismic volumes. Unfortunately, wells in this region are only logged for the interval spanning from the Devonian unconformity 30 m deeper than the top of the Dawson Bay Formation. Therefore, this approach to  $V_p/V_s$  analysis could only be undertaken over this interval. The main change to the horizon-matched  $V_p/V_s$  when the well log information is added is an increase of  $V_p/V_s$  at the bottom of the logged interval from  $V_p/V_s = 2.0$  to  $V_p/V_s = 2.5$ . This occurs in the Dawson Bay Formation just above the Prairie Evaporite Formation near the east end of the example line. This increase in  $V_p/V_s$  is interpreted to be the result of fracturing within the Dawson Bay Formation. From the Dawson Bay Formation up to the

top of the Souris River Formation, the  $V_p/V_s$  decreases by an average of 0.2, and in the Birdbear Formation the  $V_p/V_s$  has an average increase of 0.1-0.2.

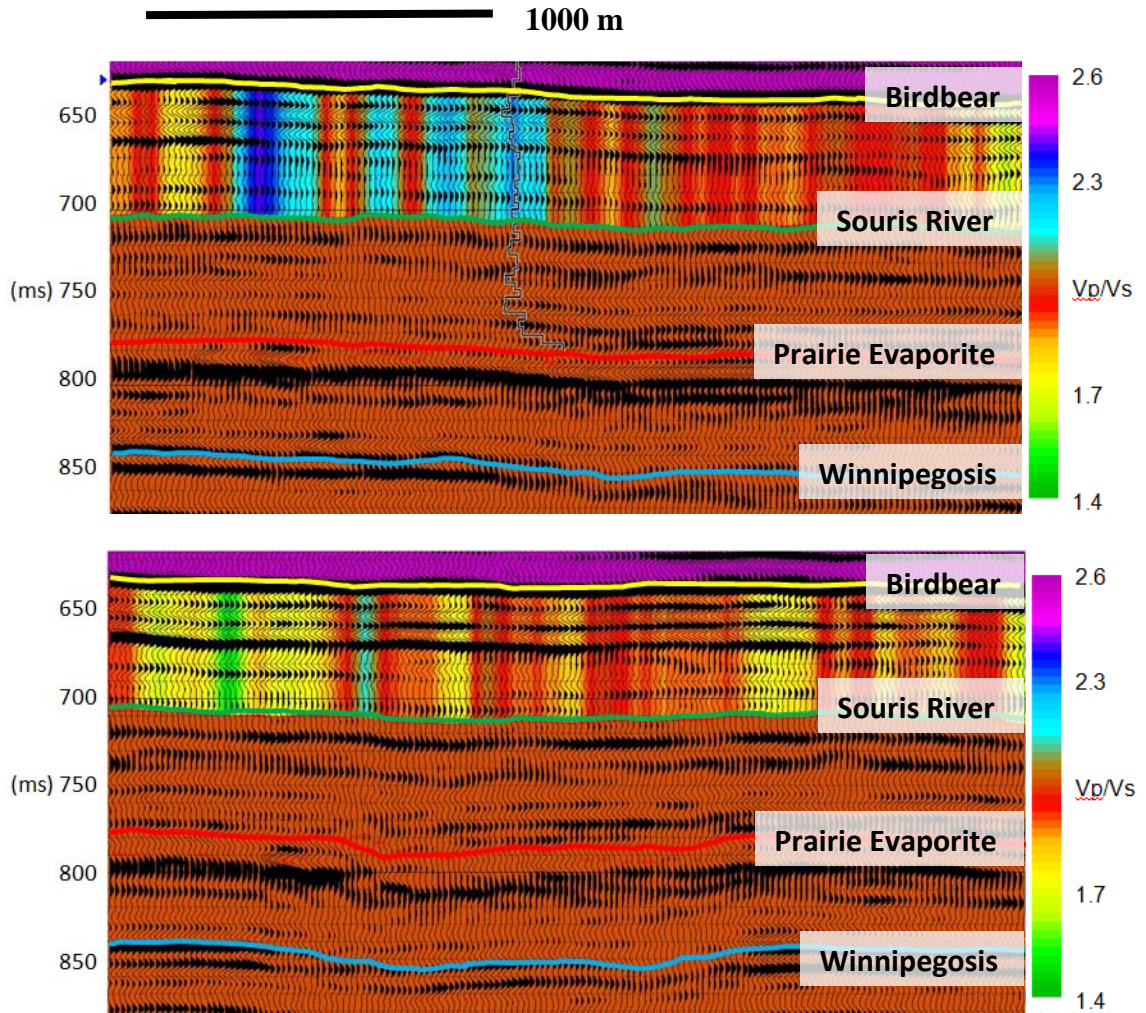


**Figure 3.4 – Crossline from the baseline volume showing a line through a well with dipole sonic log (upper) and a line through the low velocity, low amplitude anomaly in the centre of the dataset (lower). Notice the higher average  $V_p/V_s$  in the Birdbear interval on the line outside of the seismic anomaly. The top of the Birdbear Formation is the yellow horizon, the Souris River Formation is green, the Prairie Evaporite Formation is red and the Winnipegosis Formation is blue.**

When the well log  $V_p/V_s$  was applied to the region of the low velocity, low amplitude seismic anomaly, the  $V_p/V_s$  increases within the Dawson Bay Formation (Figure 3.8), just

as it does outside of the anomaly. The magnitude of the increase is similar between these areas; however, the thickness of the zone with increased  $V_p/V_s$  within the anomaly is much greater. This has been interpreted to be due to fractures having a larger vertical propagation within the area of the anomaly than they do in the region outside of the seismic anomaly.

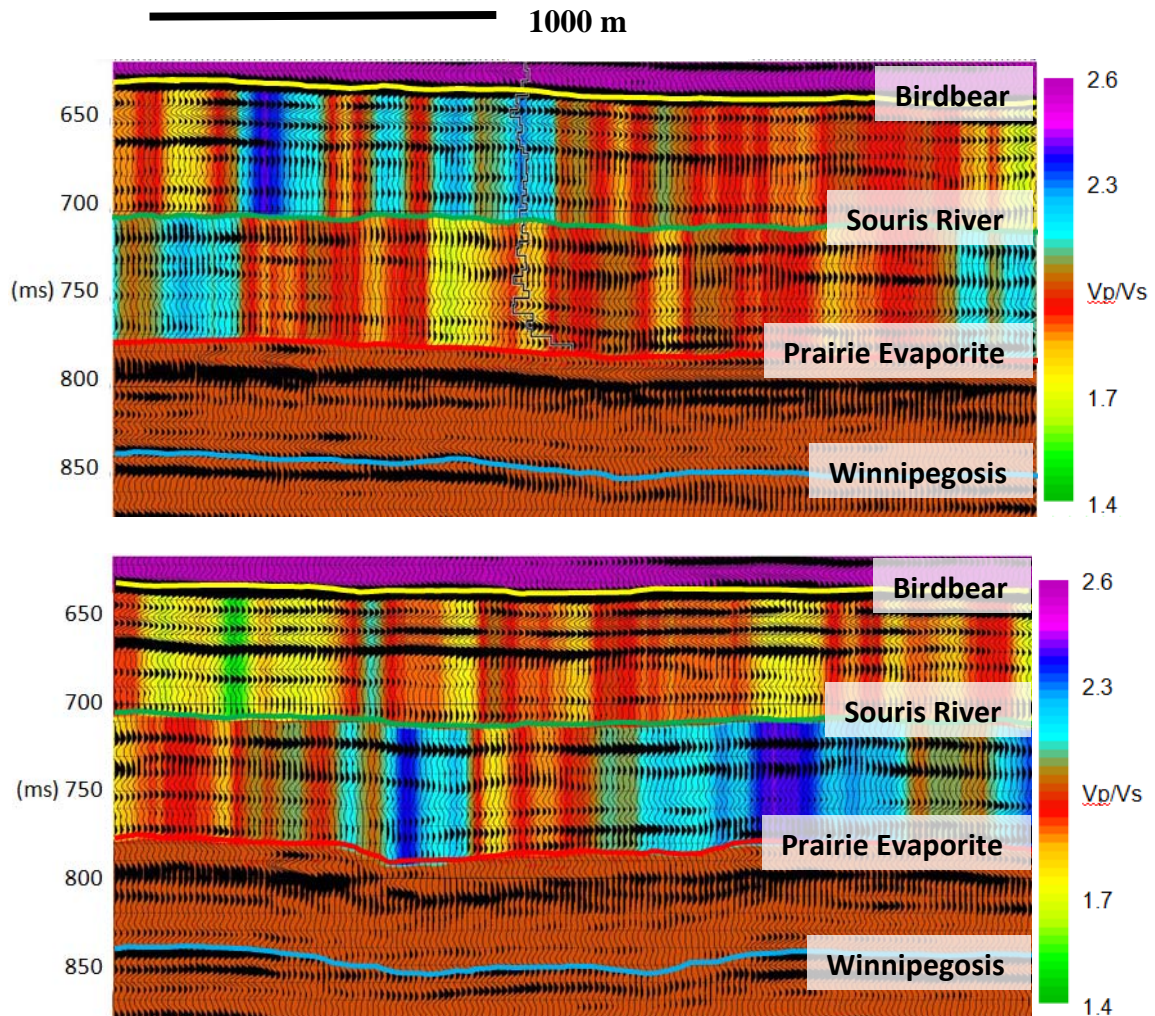


**Figure 3.5 – Crossline from the baseline volume showing a line through a well with dipole sonic log (upper) and a line through the low velocity, low amplitude anomaly in the centre of the dataset (lower). Notice the higher average  $V_p/V_s$  in the Souris River interval on the line in the seismic anomaly. The top of the Birdbear Formation is the yellow horizon, the Souris River Formation is green, the Prairie Evaporite Formation is red and the Winnipegosis Formation is blue.**

The PP and PS horizons picked from the monitor survey underwent the same analysis. Figure 3.9 shows the same crosslines as shown in Figure 3.6 (baseline survey), allowing for a time-lapse analysis of the changes in  $V_p/V_s$ .

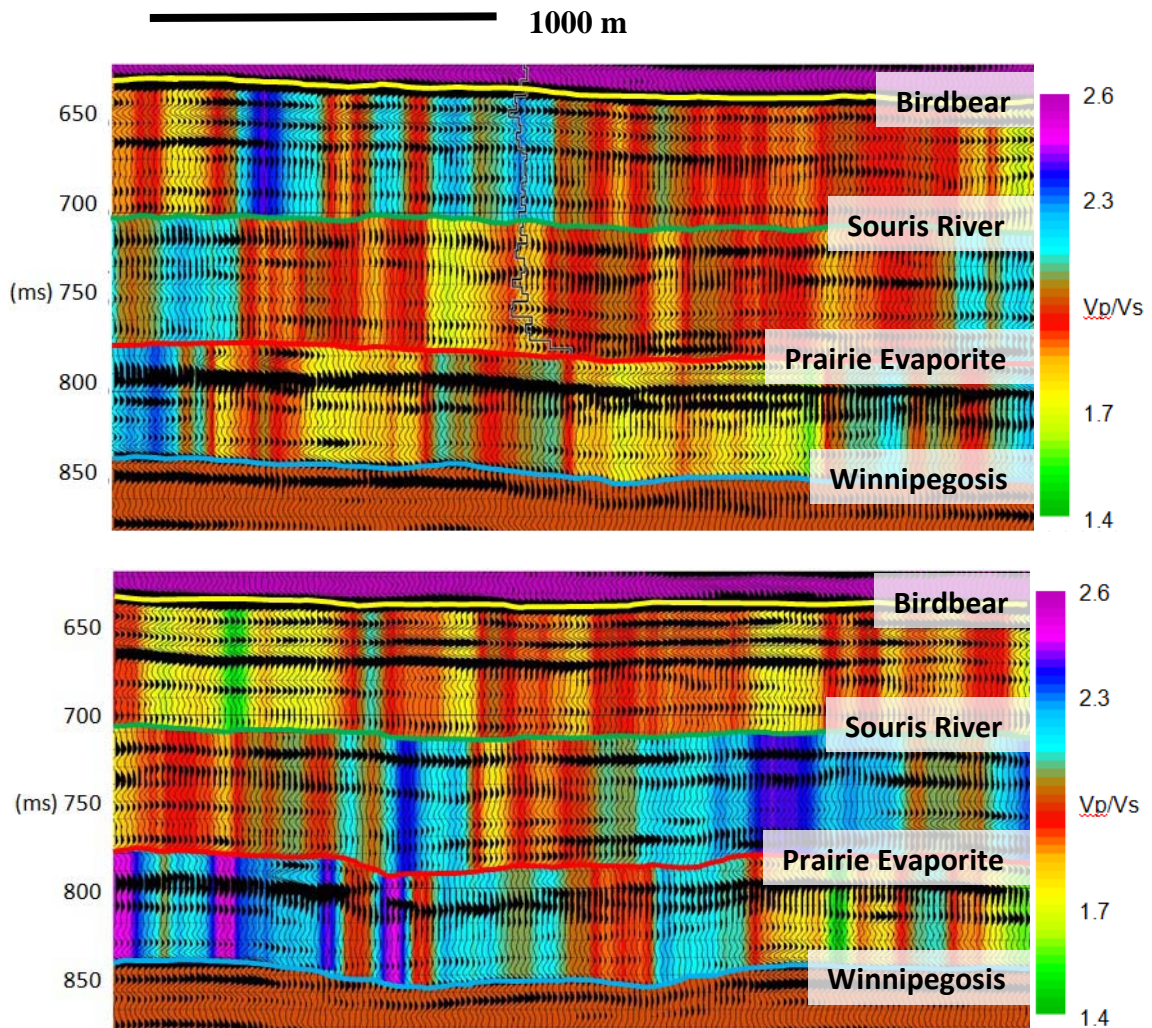


**Figure 3.6 – Crossline from the baseline volume showing a line through a well with dipole sonic log (upper) and a line through the low velocity, low amplitude anomaly in the centre of the dataset (lower). Notice the higher average  $V_p/V_s$  in the Prairie Evaporite interval on the line in the seismic anomaly. The top of the Birdbear Formation is the yellow horizon, the Souris River Formation is green, the Prairie Evaporite Formation is red and the Winnipegosis Formation is blue.**

The background Vp/Vs from well logs will not change between vintages as the well was drilled before either survey was acquired, meaning any differences in Vp/Vs are strictly related to travelttime differences between seismic vintages.

The monitor survey shows the same increase in Vp/Vs through the Souris River and Prairie Evaporite intervals within the central area of the dataset where the low velocity, low amplitude seismic anomaly is present. The higher Vp/Vs within the Birdbear interval outside of the anomaly is also seen throughout the horizon matching process for the baseline survey.

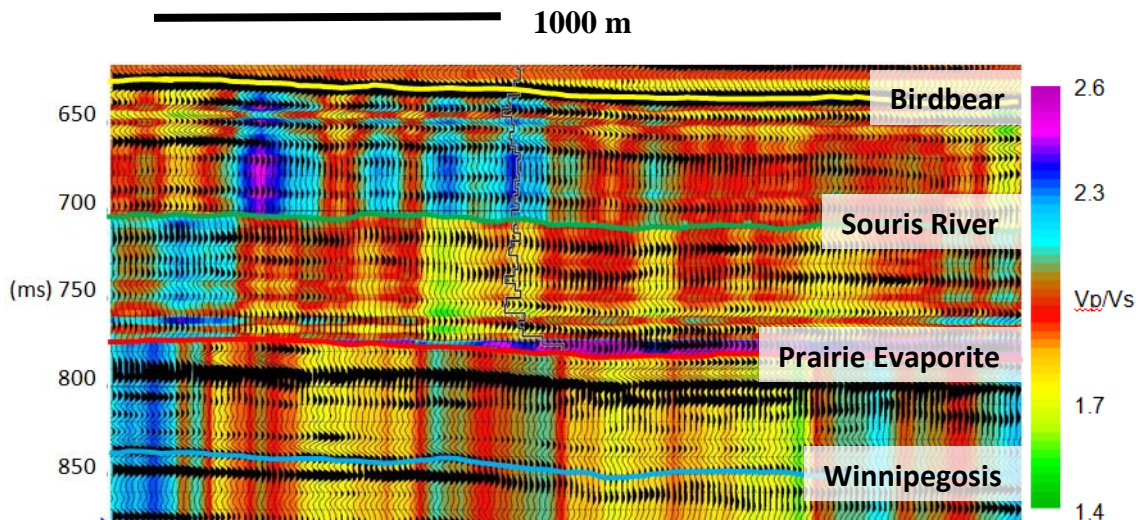


**Figure 3.7 – Crossline from the baseline volume which goes through a well with dipole sonic, where Vp/Vs log has been calculated (log on cross section). There is a significant increase in Vp/Vs at the bottom of the Souris River Formation (green horizon) within the Dawson Bay Formation when the well control is incorporated into the horizon matching process (purple on the east end of the line). The Vp/Vs increases from 2.0 to 2.5, an increase interpreted to be the result of fracturing in the lower regions of the Dawson Bay Formation, just above the top of the Prairie Evaporite Formation (red horizon).**

Incorporating the well information into the horizon matching process for the monitor survey yields results illustrated by the crosslines in Figure 3.10 and Figure 3.11, which

correspond to the crosslines from the baseline volumes in Figure 3.7 and Figure 3.8, respectively. The crossline from the monitor survey through the well (Figure 3.10) exhibits similar trends as the identical crossline from the baseline survey. This was expected as the well control provided the same correction to both vintages of the Vp/Vs volume created by the horizon matching process.

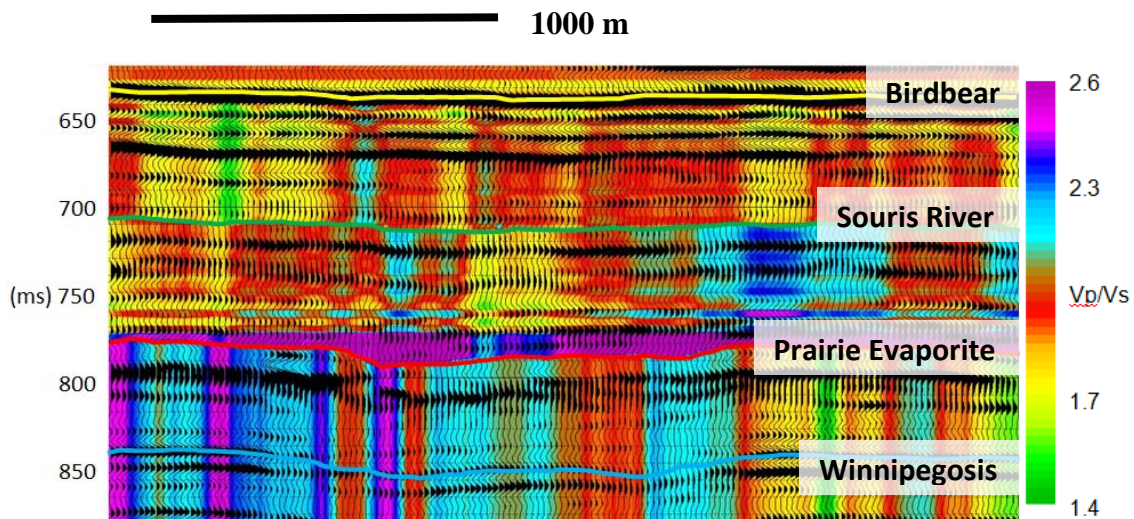


**Figure 3.8 – Crossline from the baseline volume which goes through low velocity, low amplitude seismic anomaly in the centre of the volume. There is a significant increase in Vp/Vs at the bottom of the Souris River Formation (green horizon) within the Dawson Bay Formation when the well control is incorporated into the horizon matching process (purple above the red horizon). The Vp/Vs increases from 2.0 to 2.5, an increase interpreted to be the result of fracturing in the lower regions of the Dawson Bay Formation, just above the top of the Prairie Evaporite Formation (red horizon). The increased thickness of the fractured area through the centre of the section is interpreted to be an increase in the extent of vertical fracturing.**

The crossline from the monitor survey through the centre of the seismic anomaly in the middle of the dataset shows the same increase in Vp/Vs from 2.0 to 2.5, but there is a greater area of increased Vp/Vs near the centre of the line. This would indicate an increase in the areal extent of fracturing between the baseline and monitor surveys. Looking only at

selected inlines and crosslines, however, makes it difficult to determine the spatial extent of such features.

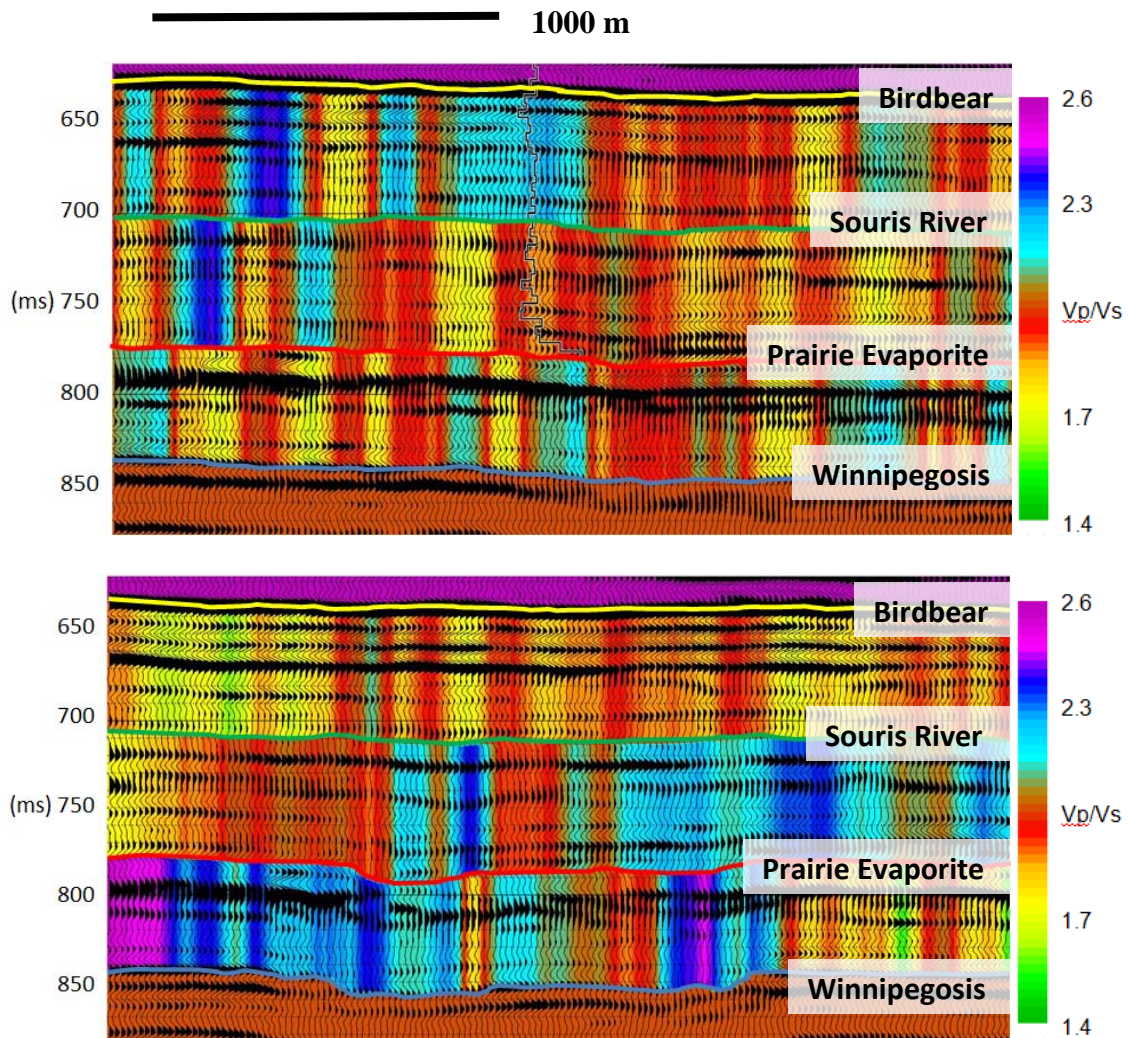


**Figure 3.9 - Crossline from the monitor volume showing a line through a well with dipole sonic log (upper) and a line through the low velocity, low amplitude anomaly in the centre of the dataset (lower). Notice that in general the crossline through the seismic anomaly in the centre of the dataset (lower) has a higher  $V_p/V_s$  than the line outside of the anomaly, specifically in the Souris River and Prairie Evaporite intervals. The Birdbear Formation has a lower  $V_p/V_s$  in the area of the seismic anomaly. These trends are unchanged from the baseline to the monitor surveys. The top of the Birdbear Formation is the yellow horizon, the Souris River Formation is green, the Prairie Evaporite Formation is red and the Winnipegosis Formation is blue.**

Seismic cross sections are an excellent way to compare vertical and horizontal differences between  $V_p/V_s$  along a particular line, but they do not give a good representation of how  $V_p/V_s$  varies spatially over an interval. For this reason interval  $V_p/V_s$  was calculated over the full 3D volume for the three intervals of interest: the Birdbear interval (top of the Birdbear Formation to the top of the Souris River Formation), the Souris River interval (top of the Souris River Formation to the top of the Prairie Evaporite Formation) and the Prairie Evaporite interval (top of the Prairie Evaporite Formation to the top of the Winnipegosis Formations).

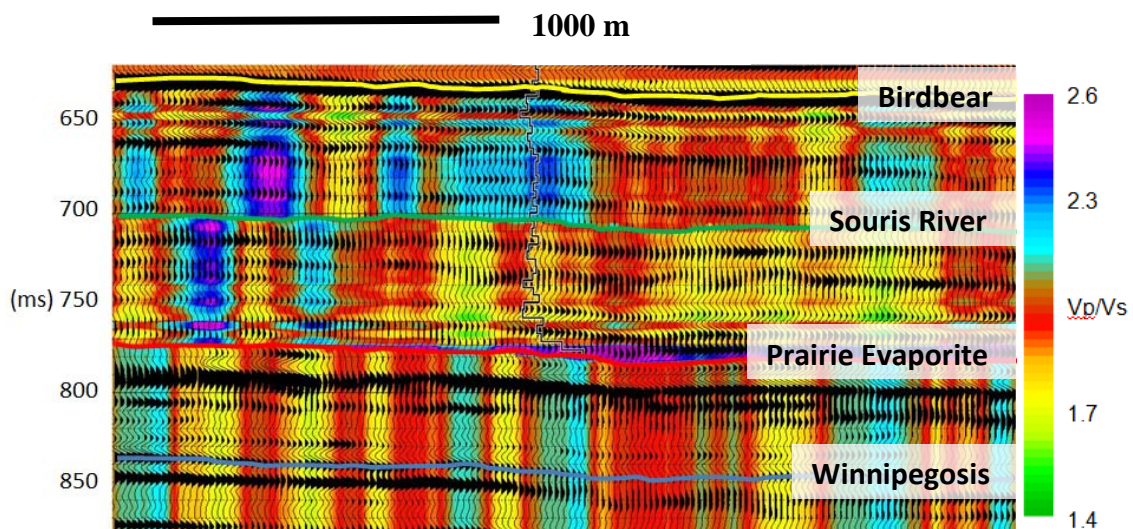


**Figure 3.10 - Crossline from the monitor volume, through a well with dipole sonic, where  $V_p/V_s$  log has been calculated (log on cross section). There is a significant increase in  $V_p/V_s$  at the bottom of the Souris River Formation (green horizon) within the Dawson Bay Formation when the well control is incorporated into the horizon matching process (purple on the east end of the line). The  $V_p/V_s$  increases from 2.0 to 2.5, an increase interpreted to be the result of fracturing in the lower regions of the Dawson Bay Formation, just above the top of the Prairie Evaporite Formation (red horizon).**

A comparison of the interval  $V_p/V_s$  between the Birdbear and Souris River horizons (Figure 3.12) confirms that there is little difference in the seismic volumes above

the Souris River Formation between the baseline and monitor surveys. Furthermore, the  $V_p/V_s$  for this interval is reasonable for the carbonate stratigraphy with an average  $V_p/V_s$  of 2.0 and local minimum and maximum values of 1.75 and 2.4, respectively.

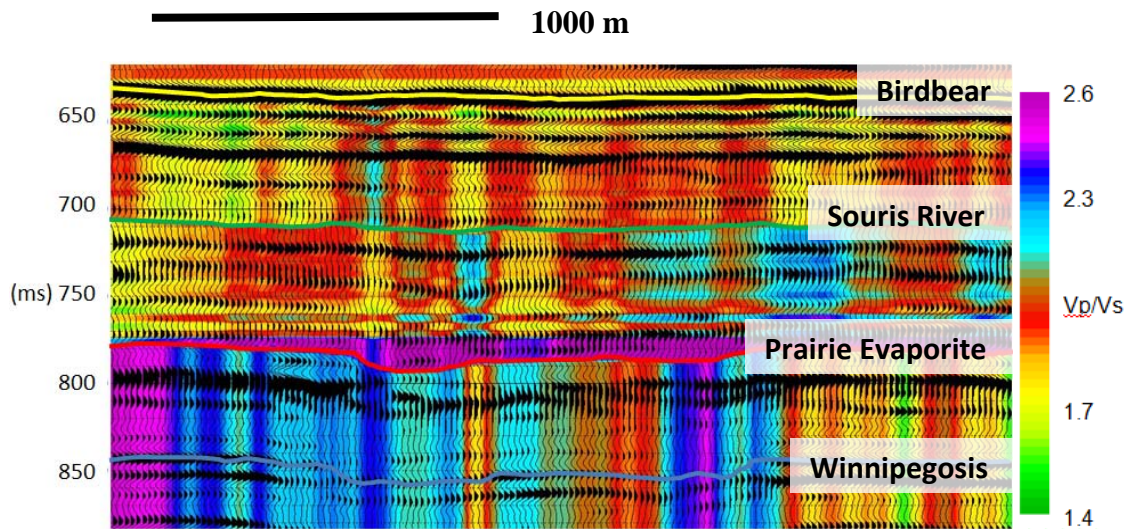


**Figure 3.11 - Crossline from the monitor volume which goes through low velocity, low amplitude seismic anomaly in the centre of the seismic volume. There is a significant increase in  $V_p/V_s$  at the bottom of the Souris River interval (green horizon) within the Dawson Bay Formation when the well control is incorporated into the horizon matching process (purple above the red horizon). The  $V_p/V_s$  increases from 2.0 to 2.5, an increase interpreted to be the result of fracturing in the lower regions of the Dawson Bay Formation, just above the top of the Prairie Evaporite Formation (red horizon). The increased thickness of the fractured area through the centre of the section is interpreted to be an increase in vertical extent of fracturing.**

$V_p/V_s$  from the fractured interval between the Souris River and Prairie Evaporite formations (Figure 3.13) displays a higher average  $V_p/V_s$  of 2.2 than found in the Birdbear-Souris River succession (Figure 3.12). Specifically, the higher average values are found in the west and southeast parts of the study area, areas where mine workings are present in the Prairie Evaporite Formation. The northeast area exhibits a lower average  $V_p/V_s$  of approximately 1.8, which corresponds to the areas where fractures would not be

likely stimulated due to mining. Neither the Birdbear-Souris River nor the Souris River-Prairie Evaporite interval Vp/Vs plots show any significant differences between the baseline and monitor surveys, indicating that no new fractures were interpreted to be formed within the Dawson Bay Formation during the time between the baseline and monitor surveys.

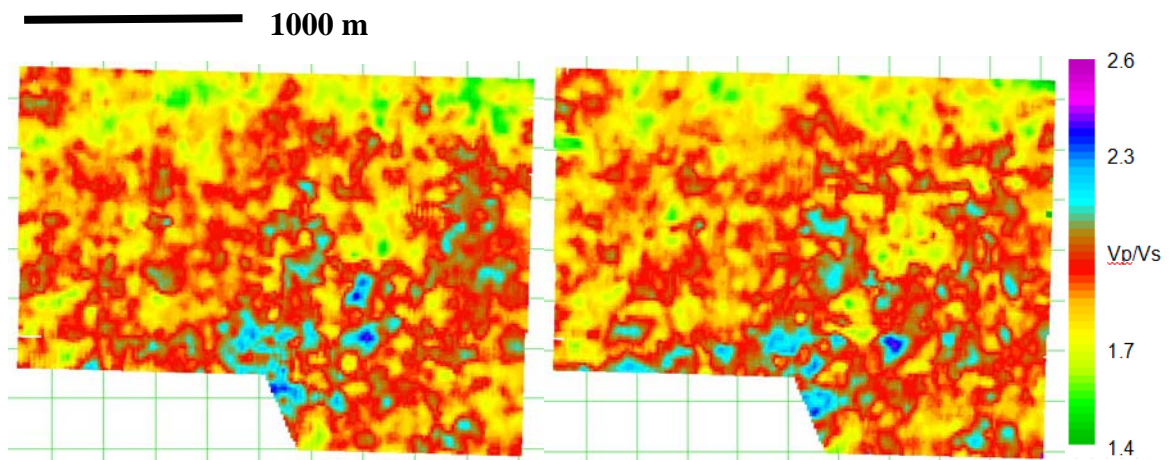


**Figure 3.12 – Interval Vp/Vs for the baseline (left) and monitor (right) from the Birdbear to Souris River formations.**

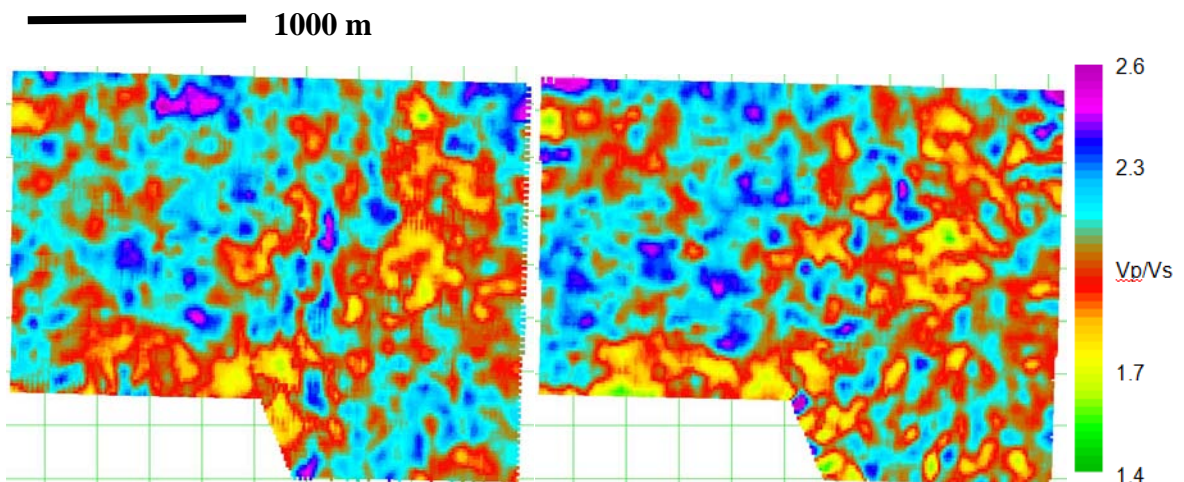


**Figure 3.13 – Interval Vp/Vs for the baseline (left) and monitor (right) from the Souris River to Prairie Evaporite formations.**

The interval  $V_p/V_s$  for the Prairie Evaporite-Winnipegosis sequence between baseline and monitor volumes shows some significant differences between the two seismic surveys (Figure 3.14).

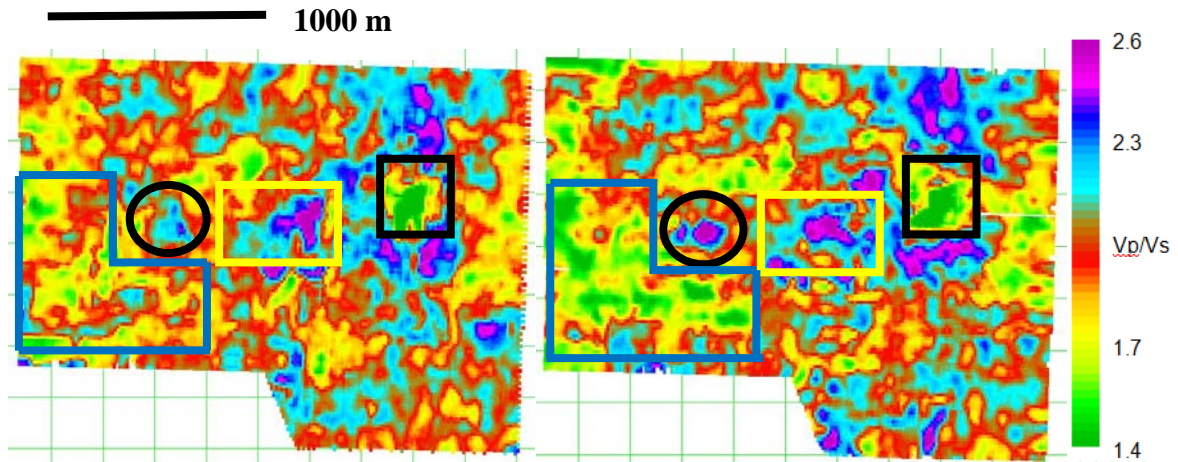


**Figure 3.14 – Interval  $V_p/V_s$  for the baseline (left) and monitor (right) surveys from the Prairie Evaporite to Winnipegosis formations. The black circles show an area of significant increase in  $V_p/V_s$  between surveys, and the black rectangle shows the location of a carbonate reef structure in the Winnipegosis Formation.**

Most notable are the significant decrease in  $V_p/V_s$  in the southwest of the study area and a increase of  $V_p/V_s$  from 2.1-2.6 within the central parts of the survey area (black ellipse in Figure 3.14). These discrepancies require further analysis in order to determine the geological cause. Two anomalies, however, remain constant over both vintages: the pinnacle reef in the northeast (low  $V_p/V_s$  of 1.4 shown by the black square in Figure 3.14) and the  $V_p/V_s$  high of 2.6 in the centre of the dataset where the low amplitude anomaly is located (yellow box in Figure 3.14), supporting the hypothesis that fractures are responsible for the presence of the low velocity anomaly.

### 3.3 Effect of Horizon Placement on Vp/Vs

There are two factors which significantly influence the calculation of the interval Vp/Vs for a specific stratigraphic interval; the picking of a particular seismic horizon on the PP volume and of course on the PS volume in order to best represent the true location of a geological interface. As the travel-time associated with both the PP and PS horizons are used to calculate Vp/Vs (Equation 1), the accuracy of horizon picking is critical for optimal Vp/Vs results. The most likely source of error comes from the PS seismic volume, where the frequency content is significantly reduced and the signal-to-noise ratio is lower than that of the PP seismic volume (Figure 3.15). This reduction in dominant frequency means that the conventional method of picking horizons at a seismic peak, trough or zero-crossing does not provide an accurate enough depiction of the true location of a geological subsurface boundary; the continuity of seismic events is also reduced because of the noise in the PS volume. In a region where the stratigraphic layers in the subsurface are as flat lying, as in the study area, it is possible to improve the accuracy of the horizon representation of the lithological boundary by picking the closest most coherent seismic event to the well top on the synthetic tie and then by applying a time shift to these pseudo-horizons. This practice is focused primarily on the PS horizons, due to the high signal-to-noise ratio and low dominant frequency and bandwidth, and not all horizons require such editing.

Figure 3.16 shows the PP synthetic seismogram tie with the geological tops from the well logs along with the horizons picked. The Souris River horizon was shifted by -13 ms to better match the location of the geologic top on the seismic section. While picking the PS horizons it was found that the geological top for the Souris River Formation is located on

the shoulder of the peak at about 1300 ms which makes picking a seismic event to portray this geological interface difficult. In order to pick a horizon which best portrays the true subsurface location of the Souris River Formation, a more coherent seismic peak 38 ms below the geological top from the well logs was picked as a pseudo-horizon which is later shifted to the proper position (Figure 3.17). The same procedure was applied to the PS Prairie Evaporite horizon pick as the most coherent event closest to the top of the Prairie Evaporite Formation was 20 ms below the bottom of the well log.

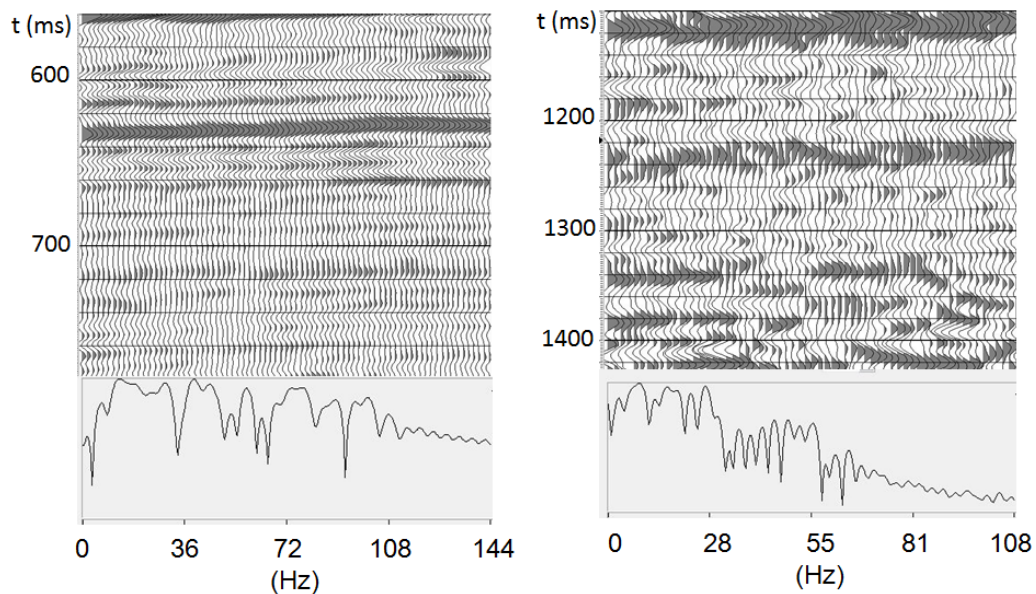


**Figure 3.15 – Seismic crossline showing the difference in frequency content between the PP (left) and PS (right) volumes for intervals of identical thickness. The frequency spectrum associated with each interval is directly below the seismic section.**

The selection of the correct time shift for each horizon is important because the  $V_p/V_s$  ratio is very sensitive to errors in travel-time picks between PP and PS volumes. Figures Figure 3.18 through Figure 3.21 shows the effect PS travel-time errors can have on the associated interval  $V_p/V_s$ . Figure 3.18 shows a crossline through the azimuthal stack volume A where a of -38 ms time shift (that used for the full azimuthally stacked section)

has been applied to the Souris River PS pseudo-horizon and its resulting  $V_p/V_s$ . This time shift is not suitable for the azimuthally stacked volume, as the  $V_p/V_s$  is too high above the Souris River Formation pick, and too low below the Souris River Formation.

Figure 3.19 shows the same section using a -45 ms time shift on the Souris River pseudo-horizon. The -7 ms difference in the time shift results in a decrease in  $V_p/V_s$  above the Souris River Formation and an increase below the Souris River Formation on the order of 0.2. Notice that below the Prairie Evaporite (where no changes were made) the  $V_p/V_s$  remains constant for the Prairie Evaporite-Winnipegosis interval.

Figure 3.20 and Figure 3.21 show the  $V_p/V_s$  in map view for both the Birdbear-Souris River interval and the Souris River- Prairie Evaporite interval, respectively. These images show that although the magnitude of the  $V_p/V_s$  changes due to the difference in time shifts applied, the general trends are the same.

### **3.4 Summary**

An increase in  $V_p/V_s$ , calculated using the interpreted PP and PS horizons, corresponds with the low velocity anomaly in the centre of the study area. This suggests the presence of fracture networks which extend vertically to sub-vertically from the Prairie Evaporite Formation towards the top of the Dawson Bay Formation. Fractures reduce S-wave velocities more significantly than P-wave velocities resulting in an overall increase in  $V_p/V_s$ . I observed that  $V_p/V_s$  also increased between the baseline and monitor seismic volumes where the central, low velocity anomaly is present, indicating a potential increase in fracture density within this anomalous area over the course of the acquisition of the two seismic surveys.

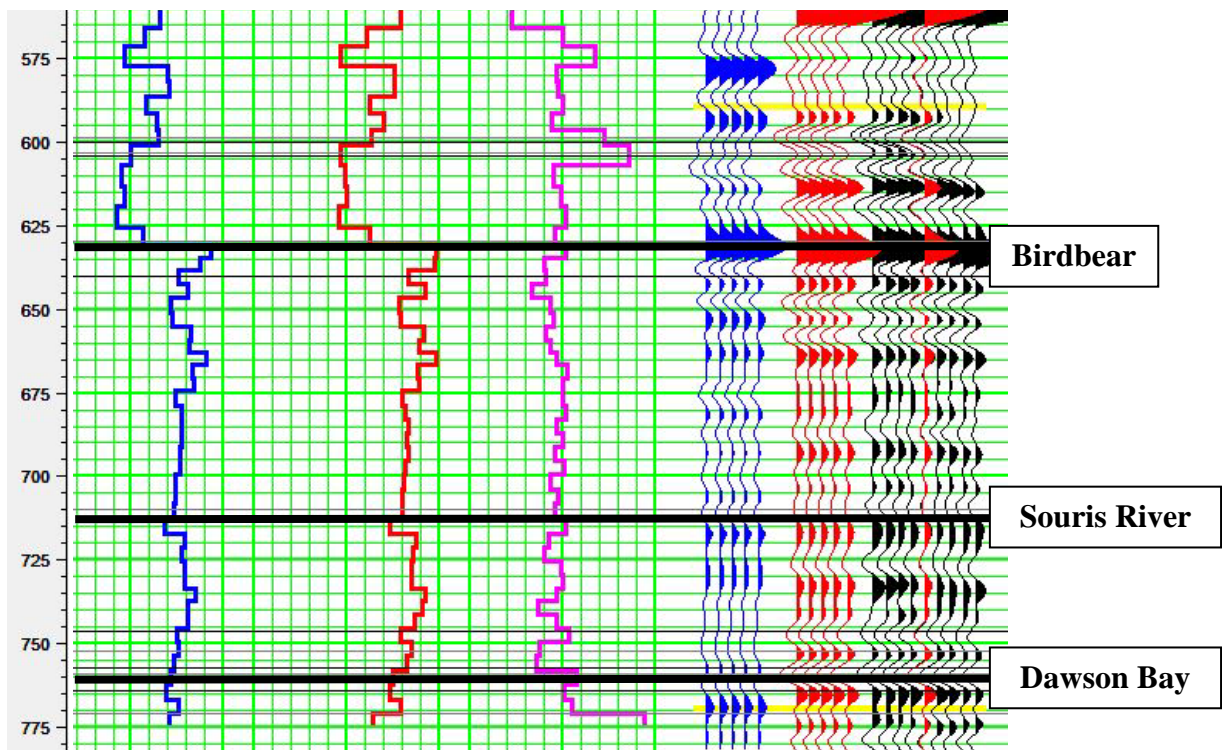


Figure 3.16 – PP synthetic seismogram (blue seismic trace) tied to the 2004 full azimuth stack PP seismic volume (red and black seismic). The logs on the left are the P-sonic (blue), S-sonic (red) and calculated  $V_p/V_s$  (pink).

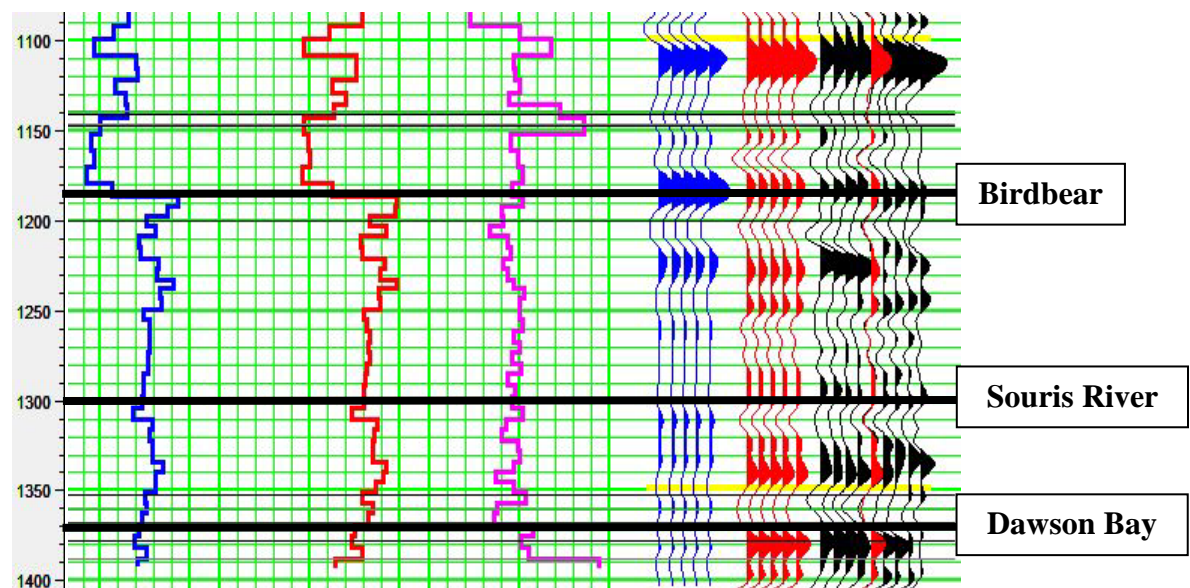
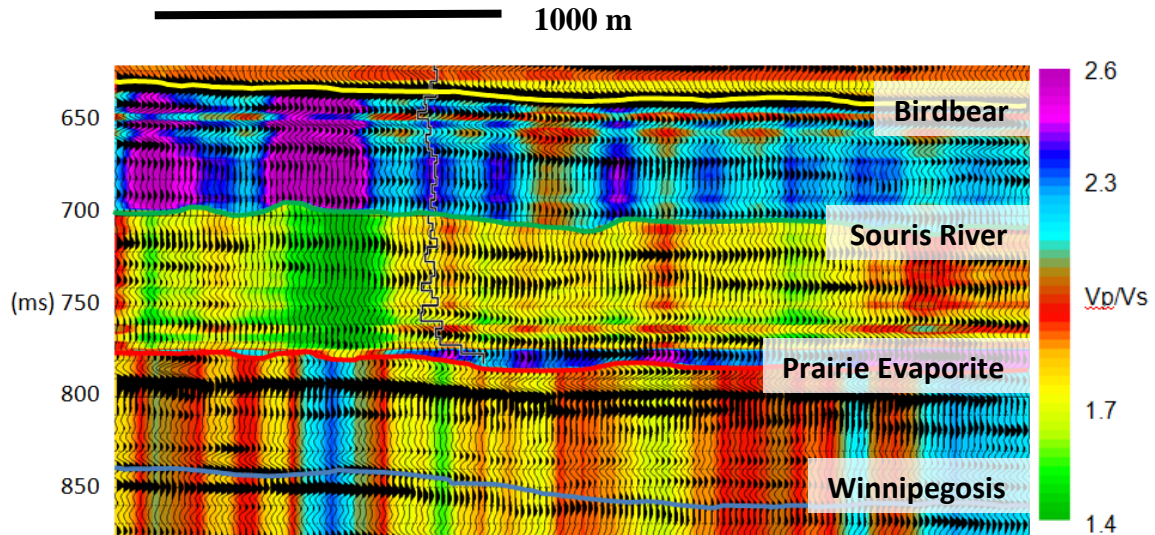


Figure 3.17 – PS synthetic seismogram (blue seismic trace) tied to the 2004 full azimuth stack PS seismic volume (red and black seismic). The logs on the left are the P-sonic (blue), S-sonic (red) and calculated  $V_p/V_s$  (pink).



**Figure 3.18 – Crossline through the well (same as Figure 3.7) which shows the difference in  $V_p/V_s$  in the Birdbear – Souris River and Souris River – Prairie Evaporite intervals for the baseline seismic volume A. This difference is due to the time shift (-38 ms) applied to the Souris River horizon from the PS volume, orientation A.**

In order for the interval  $V_p/V_s$  analysis to be as accurate as possible, it was necessary to select a seismic event, both PP and PS, which best corresponds to the location of the well top on the seismic section. The PP seismic volumes have higher dominant frequency than that of the PS volumes, therefore, selecting a seismic peak or trough which represents a geological interface is relatively simple. The lower frequency bandwidth and dominant frequency of the PS seismic volumes results in significantly reduced temporal resolution, which in turn makes it more difficult to place a seismic horizon at the location of a geological interface.

Applying a time shift to the PS horizon corrected this issue and placed the seismic horizon at a more appropriate temporal position, and this resulted in a more accurate interval  $V_p/V_s$  for the stratigraphy of interest. Small temporal shifts of as little as  $\pm 7$ ms, as

discussed in this chapter, can have a significant influence on the magnitude of  $V_p/V_s$ , showing the importance of precise picking the PS horizon.

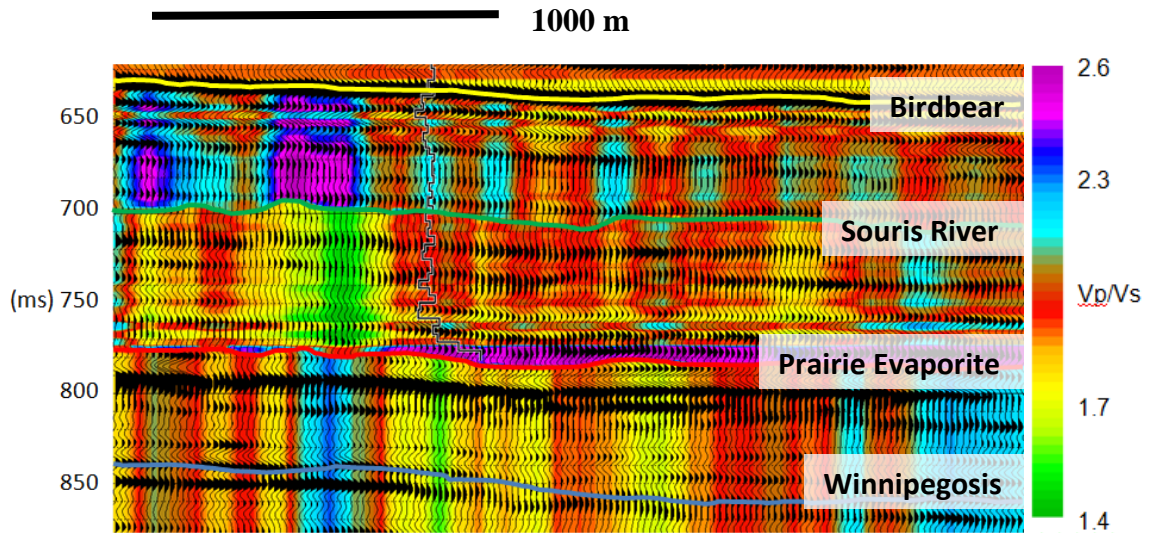


**Figure 3.19** – Crossline through the well (same as Figure 3.7) with an adjusted time shift (-45 ms) applied to the Souris River Formation of the baseline A PP and PS seismic volumes.

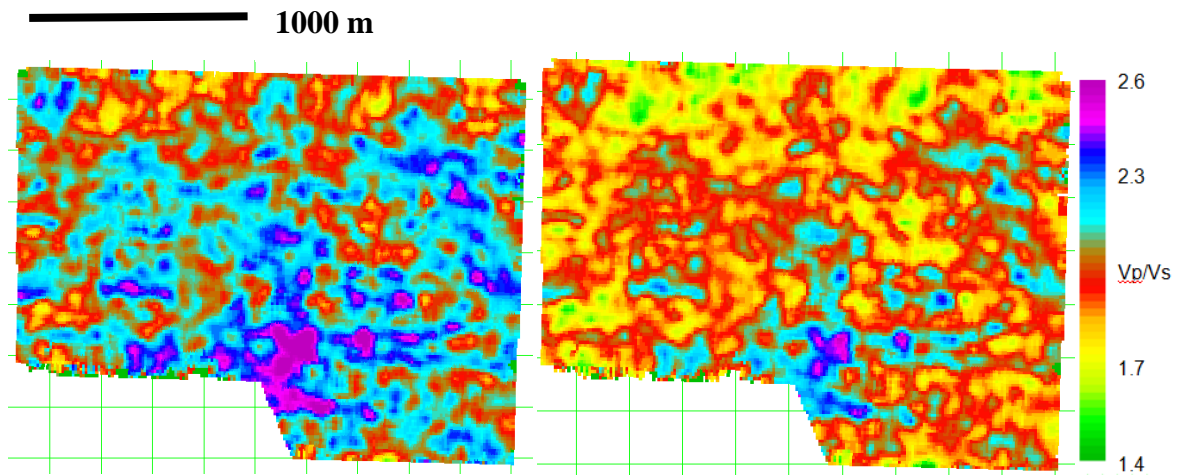


**Figure 3.20** – Comparison between the interval  $V_p/V_s$  from the Birdbear Formation to Souris River Formation for the seismic volumes of orientation A. On the left, the same time shift is applied to the Souris River Formation as was in the full azimuth volume (-38 ms). On the right, a reassessed time shift of -45 ms is applied in order to better position the horizon on the seismic section.

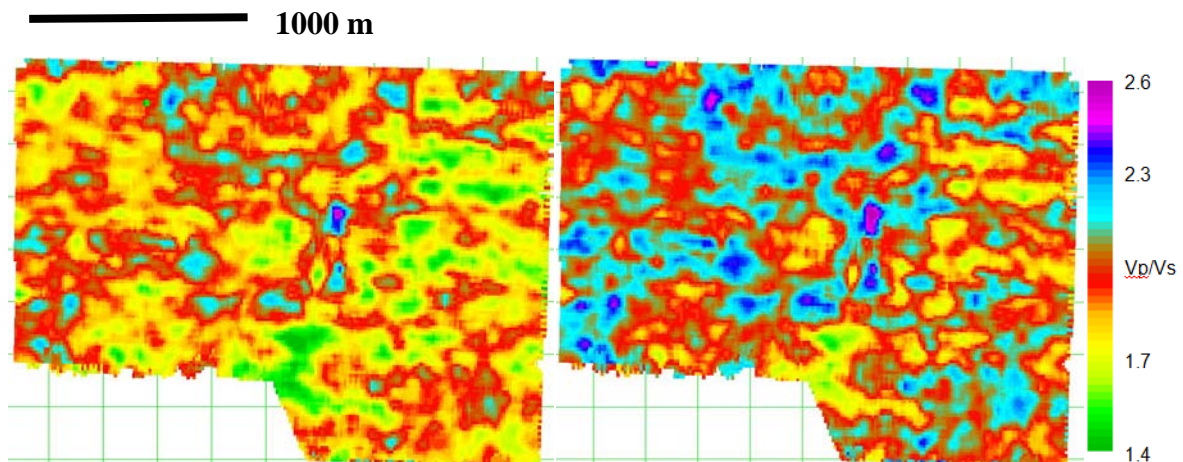


**Figure 3.21 – Comparison between the interval  $V_p/V_s$  from the Souris River Formation to the Prairie Evaporite Formation for the seismic volumes of orientation A. On the left, the same time shift is applied to the Souris River Formation as was in the full azimuth volume. On the right, a reassessed time shift of -45 ms is applied in order to better position the horizon on the seismic section.**

## Chapter Four: **SEISMIC ATTRIBUTE ANALYSIS**

### **4.1 Introduction**

A seismic attribute is defined as a value calculated from seismic data which highlights the time, amplitude and frequency of seismic signal. Time attributes are typically associated with geological structure, where amplitude and frequency are related to stratigraphy and reservoir characterization (Sheriff, 2011). Seismic attribute analysis is a way of extracting additional information from a seismic volume. Attribute analysis was made possible through the developments in digital signal recording of seismic data and has been under development since the 1970s. Making the switch from analog to digital signal recording improved the quality of seismic data, and by 1975 almost all of the acquired seismic lines were being recorded digitally (Chopra & Marfurt, 2007). Improved signal quality led to the realization that preservation of relative amplitude could benefit explorationists and the quantification of seismic amplitudes was a technology which would be useful in hydrocarbon exploration (Chopra & Marfurt, 2007).

Once colour display was made available by Balch (1971), it was believed that attribute analysis would become more quantitative through the use of colour as opposed to variable-area displays (Anstey, 2005). Although advancements in attribute technology were being made through the 1980s due to significant increases in computer processing power and seismic processing capability, seismic attributes themselves fell slightly out of favor with interpreters due to problems assigning physical meaning to attributes. This lasted until the 1990s when 3D seismic technology became standard in the oil and gas industry. The extraction of seismic attributes across entire 3D seismic volumes, and the 3D visualization

of features within the attribute gave seismic interpreters the ability to analyze variations in seismic structure and stratigraphy between seismic lines (Chopra & Marfurt, 2007).

#### 4.1.1 Complex Seismic Trace Analysis

Complex seismic trace analysis was among the first of the seismic attributes and was introduced by Taner, Koehler & Sheriff (1979) as reported by Barnes (2007), Chopra & Marfurt (2007). The method focuses on the concept that a seismic trace,  $f(t)$ , is the real part of a complex signal:

$$F(t) = f(t) + i f^*(t), \quad (4.1)$$

where  $i = \sqrt{-1}$ , and  $f^*(t)$  is the quadrature component. The seismic trace is defined as:

$$f(t) = A(t) \cos \theta(t), \quad (4.2)$$

and the quadrature trace is the seismic trace rotated by -90 degrees:

$$f^*(t) = A(t) \sin \theta(t). \quad (4.3)$$

where  $\theta(t)$  is the phase angle. The trace envelope, also known as instantaneous amplitude, and most commonly as amplitude envelope,  $A(t)$ , is calculated using both the real seismic trace, and the quadrature trace:

$$A(t) = [f^2(t) + f^{*2}(t)]^{1/2} = |F(t)|. \quad (4.4)$$

The amplitude envelope is the maximum amplitude a seismic trace can achieve with a constant phase rotation (Barnes, 2007). The magnitude of the amplitude envelope depends on lithology, bed thickness, and frequency content within the seismic trace. High reflection strength is often associated with major lithological boundaries, and can differ from the amplitude value of the real trace due to thin bed interference patterns, or any lateral variation in rock properties along either side of an unconformity or lithological boundary

(Taner, Koehler, & Sheriff, 1979). In the past, rapid changes in reflection strength have been used to interpret faults and search for hydrocarbons, specifically gas (Taner, Koehler, & Sheriff, 1979).

#### 4.1.2 Semblance Attribute

The semblance attribute is used to compare the seismic amplitudes of a single trace to the seismic amplitudes of several adjacent traces. Semblance is based on the Bahorich and Farmer (1995) coherence cube, which is a crosscorrelation technique that immediately showed major faulting and salt diapirs (Figure 4.1) as well as sedimentary structures such as channels which were previously difficult to interpret on typical seismic sections. The semblance attribute used in this study is calculated using the following equation:

$$S = \frac{\sum_{i=k-N/2}^{i=k+N/2} [\sum_{h=1}^L \sum_{j=1}^M f_{ijh}]^2}{L \cdot M \sum_{i=k-N/2}^{i=k+N/2} \sum_{h=1}^L \sum_{j=1}^M (f_{ijh}^2)} \quad (4.5)$$

Where  $f_{ijh}$  is the seismic trace, L is the number of lines, M is the number of traces and N is the number of samples and is based on the semblance-based coherency algorithm from Marfurt et al. (1998). Coherency algorithms have been used, since their development, to better characterize fault systems which run parallel to strike where their seismic signature becomes lost against a background of sedimentary bedding (Chopra, 2002). Some examples of fault detection using coherence can be found in Marfurt et al. (1998), Chopra & Marfurt (2007) and Brown (2004).

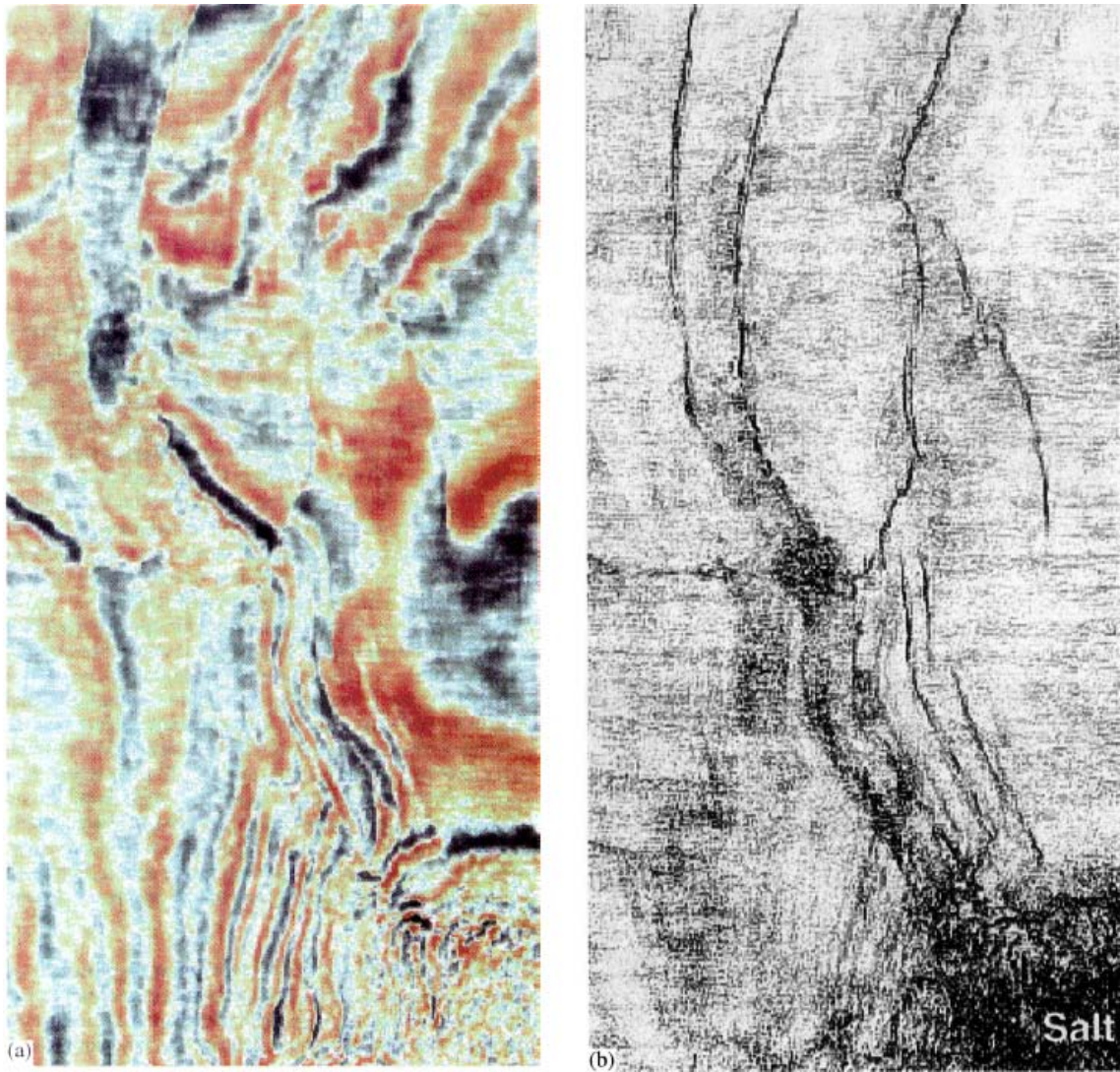


**Figure 4.1 – (a) A time-slice through a PP seismic volume in which many of the faults in the coherence time-slice (b) at the same level are difficult to see. (from Bahorich & Farmer, 1995)**

In this thesis, combining the analysis of the amplitude envelope and semblance attributes, conducted on both the PP and PS baseline and monitor volumes, gave further insight into the interpretation of the depositional environment and localised failure networks discussed in the previous chapters.

## **4.2 Seismic Attribute Interpretation**

### ***4.2.1 Baseline PP Seismic Attribute Analysis***

The interpretation of seismic attributes in this chapter focused on the interval of interest between the Birdbear Formation and the Winnipegosis Formation. The purpose of attribute analysis was to determine the extent to which fractures may exist in the subsurface both horizontally and vertically. First, a time slice through the semblance and amplitude envelope volumes was taken at 710 ms in the PP baseline volume (Figure 4.2). These slices show that the eastern half of the seismic volume at this level has a reduced coherence between adjacent traces. The amplitude envelope slice at 710 ms shows a dominant amplitude less than 0.5. The areas of lowest amplitude envelope values in the northeast of the survey correspond to the areas of lowest semblance (red box).

A time slice through 720 ms shows a dramatically different character on the baseline PP semblance plot in Figure 4.3. The majority of this slice has a high coherence, meaning that there is very little difference seismically and therefore lithologically at this level. However, in the centre of the volume there is an ellipsoid feature (red ellipse) which appears to have a low coherence with the surrounding carbonates of the Souris River Formation. Another feature of interest is the triangle shape in the southeast of the survey area (green triangle) which matches the location of a carbonate mound in the Winnipegosis Formation (Figure 2.7). The 720 ms slice through the amplitude envelope volume shows an increase in the average value. The centre of the dataset displays amplitude envelope values on the order of 1.0 to 1.5, except in the area which corresponds to the lowest semblance values, from the top of Figure 4.3, where the amplitude envelope value is on the order of

0.0 to 0.3. The area where the carbonate mound is outlined in the semblance plot (green triangle) does not exhibit any amplitude envelope anomaly.

At the bottom of the Souris River Formation, just above the Dawson Bay Formation, a time slice through the baseline PP semblance volume at 748 ms (top of Figure 4.3) shows high semblance values everywhere except a central anomaly as was seen in the 720 ms time slice (red ellipse), and in the southeast of the slice where the carbonate mound feature is present (green triangle).

The amplitude envelope slice at 748 ms (bottom of Figure 4.3) has a high background amplitude envelope on the order of 1.0 to 1.5 except around the edges and at the locations of the two areas with low semblance in the corresponding slice through the semblance volume, where the amplitude envelope drops to low magnitudes between 0.0 and 0.5.

The top of the Prairie Evaporite Formation is located at approximately 774 ms and displays high semblance values in the baseline PP volume (top of Figure 4.5). One area in the centre of the time slice exhibits slightly decreased semblance values which I interpret to highlight the borders of the semblance anomalies seen within the Souris River Formation and just above the Dawson Bay Formation, shown in Figure 4.3 and Figure 4.4, respectively. These anomalies on the semblance time slice correspond to amplitude envelope values between 0.0 and 0.3 on the 774 ms slice through the amplitude envelope volume (bottom of Figure 4.5). The eastern half of the amplitude envelope time slice has values between 1.0 and 1.5, where those in the western half of the survey are between 0.5 and 1.0. The central amplitude and semblance anomaly has interpreted to be the result of fracturing in the Dawson Bay Formation which has propagated upwards through the stratigraphic column.

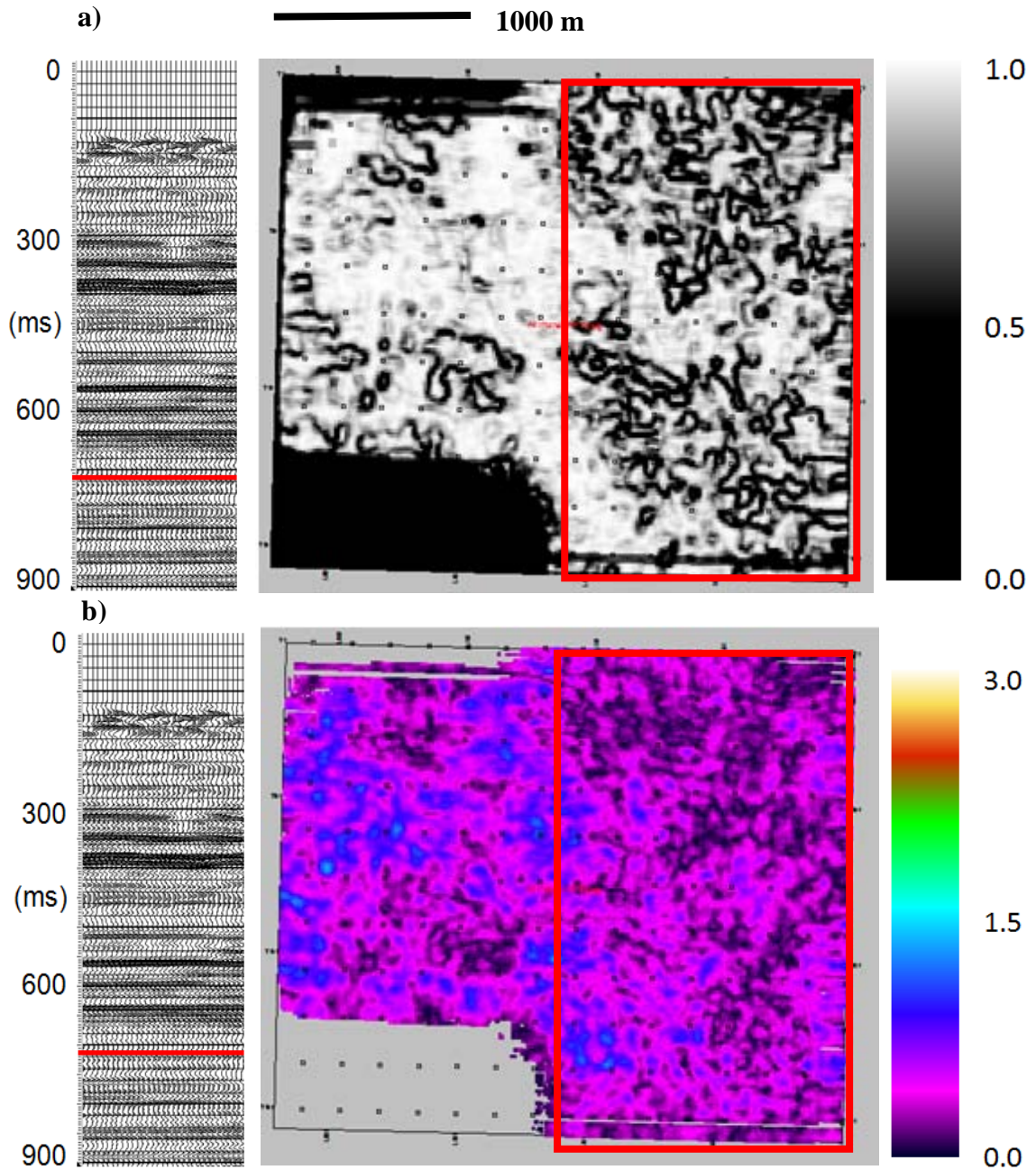


**Figure 4.2 – Baseline PP semblance (a) and amplitude envelope (b) time slice through the top of the Souris River Formation (710 ms). The eastern edge of the survey shows a lower semblance value (red box) than the western edge. The lowest amplitude envelope values on the eastern edge of the survey correspond to low semblance values in the corresponding semblance slice.**

When a time slice at 792 ms through the mine level is analyzed, the mine workings are evident in both the semblance slice (Figure 4.6a) and the amplitude envelope slice (Figure 4.6b). The mine rooms are delineated nicely to the southeast, and along the eastern edge of the survey in both the semblance and amplitude envelope volumes. The air-filled mine rooms show up as high amplitude envelope values due to the high impedance contrast in density and P-wave velocity with respect to the salt of the Prairie Evaporite Formation and the mine rooms. Semblance also delineates the edges of the mine rooms due to the large differences in reflectivity generated through high impedance contrasts (Figure 4.6). The majority of the slice through the amplitude envelope volume has a background value of 1.5 except in the northwest (red box) and the centre (red ellipse) of the dataset where the values are much lower (between 0.0 and 0.5). The northwest low-amplitude anomaly is not present in the semblance time slice, however, the central amplitude anomaly outlines an area of lower semblance which has been interpreted to be the result of fracturing.

A time slice through the middle of the Prairie Evaporite Formation, at 836 ms, shows some residual effects of the mine workings in both the semblance (Figure 4.7a) and amplitude envelope (Figure 4.7b) time slices. The semblance time slice indicates a more chaotic reflection pattern in the western half of the Prairie Evaporite Formation, interpreted to be the result of mine rooms at the mine level above. The semblance slice also indicates that there are two carbonate reefs present at 836 ms in the eastern half of the survey (red circles), in the middle of an eastern high semblance step-like feature (green box).

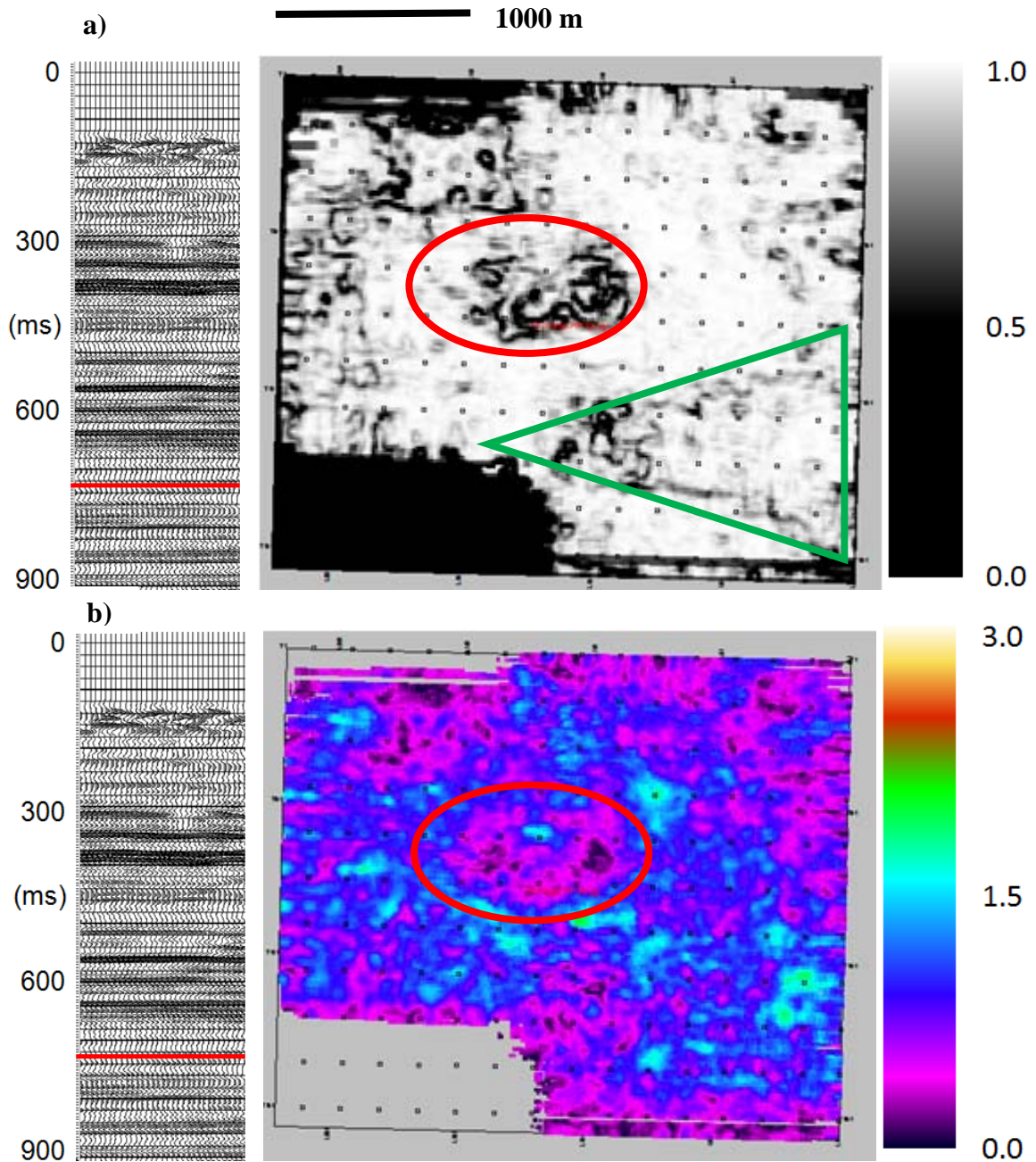


**Figure 4.3 – Baseline PP semblance (a) and amplitude envelope (b) time slices through the middle of the Souris River Formation (720 ms). In general the semblance is high across the slice except in the centre of the volume where a low semblance anomaly exists. This anomaly corresponds to the high  $V_p/V_s$  anomaly described in Figure 3.14. The lowest amplitude envelope values, found in the centre of the dataset, correspond directly to the area of low semblance from Figure 4.2.**

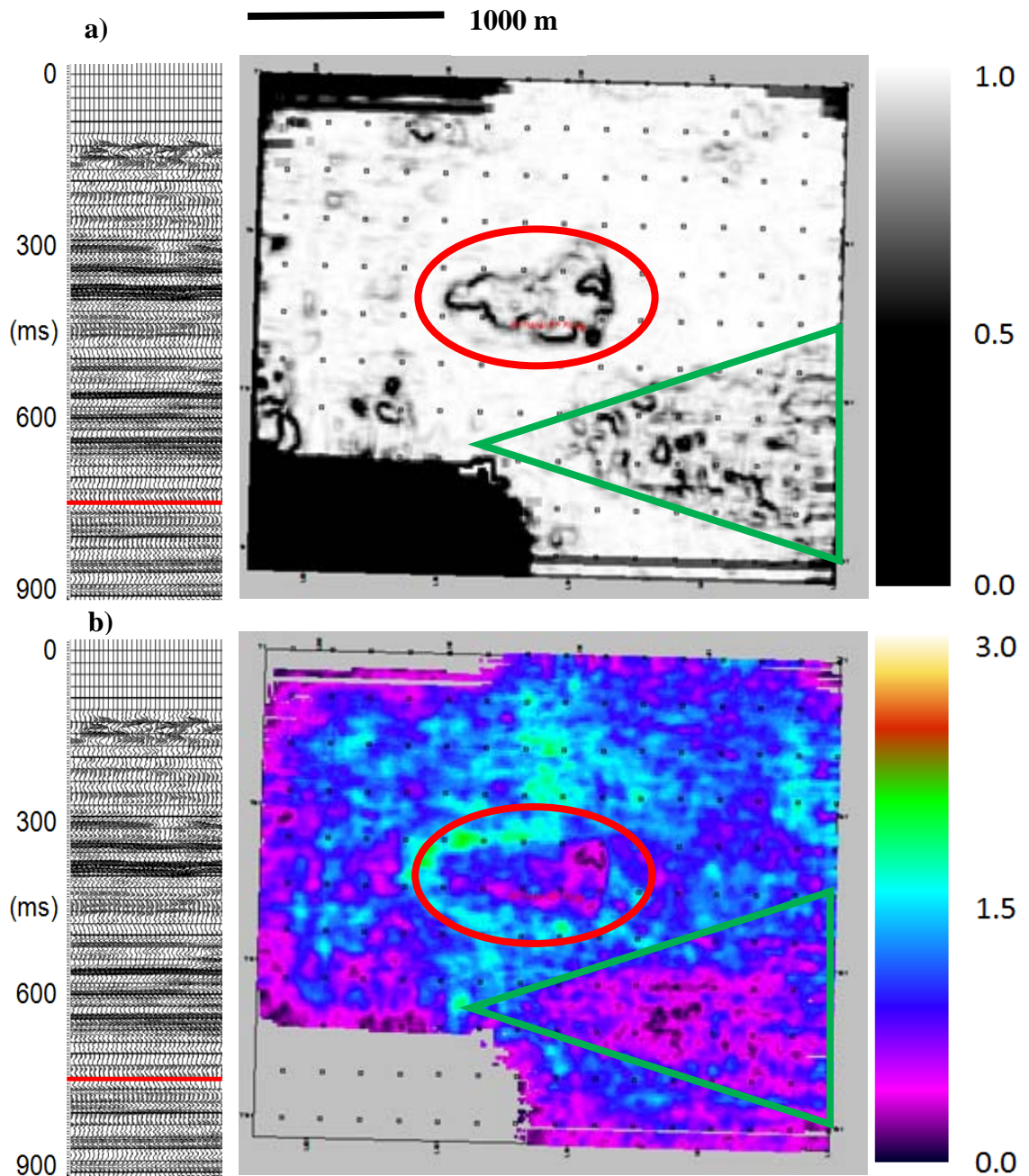


**Figure 4.4 - Baseline PP semblance (a) and amplitude envelope (b) time slices just above the top of the Dawson Bay Formation (748 ms). The semblance time slice shows two anomalies with relatively low semblance: one in the centre of the dataset where a low amplitude, low velocity anomaly with high  $V_p/V_s$  is located and another where a carbonate mound is interpreted to be located in the Winnipegosis Formation below. The amplitude envelope time slice (b) shows amplitudes between 1.0 and 1.5 throughout the slice except around the edges of the survey area and where the low semblance anomalies are located.**

These reefs are visible because of the significant difference in reflectivity between the salt of the Prairie Evaporite Formation and the carbonates of the Winnipegosis reefs. The reefs are also visible on the amplitude envelope time slice at the same level as two low value circles (magnitude of 0.5) in the middle of an eastern section with an average amplitude envelope value of 1.5 and 2.0.

The semblance time slice at the top of the Winnipegosis Formation (848 ms) contains semblance values nearing 1.0 for most of the section (Figure 4.8a). There are low semblance values at the location of the interpreted fracture network in the middle of the dataset (red circles), and along the edges of the step-like feature seen within the Prairie Evaporite Formation. The geological interpretation of this step-like feature is a carbonate mound as it matches the structural high on the Winnipegosis horizon (Figure 2.7). The amplitude envelope at this level (Figure 4.8b) shows higher amplitude envelope values (on the order of 2.0-2.5) in the northwest and southeast, and a significant drop in value (magnitude of 0.0 to 0.5) to the northeast. The two reef features are no longer present because the slice is slightly below the top of the Winnipegosis Formation.

#### ***4.2.2 Baseline PS Seismic Attribute Analysis***

Once the analysis of the PP semblance and amplitude envelope attributes had been completed, the same attributes were calculated for the baseline PS full azimuth stack volume. The PP and PS volumes were then compared at the same level in order to see if there was any correlation between anomalies seen in the PP volumes and those in the PS volumes. The PP and PS registration process was critical in order to compare the seismic attributes from the PP volumes to those of the PS volumes at the same depth.

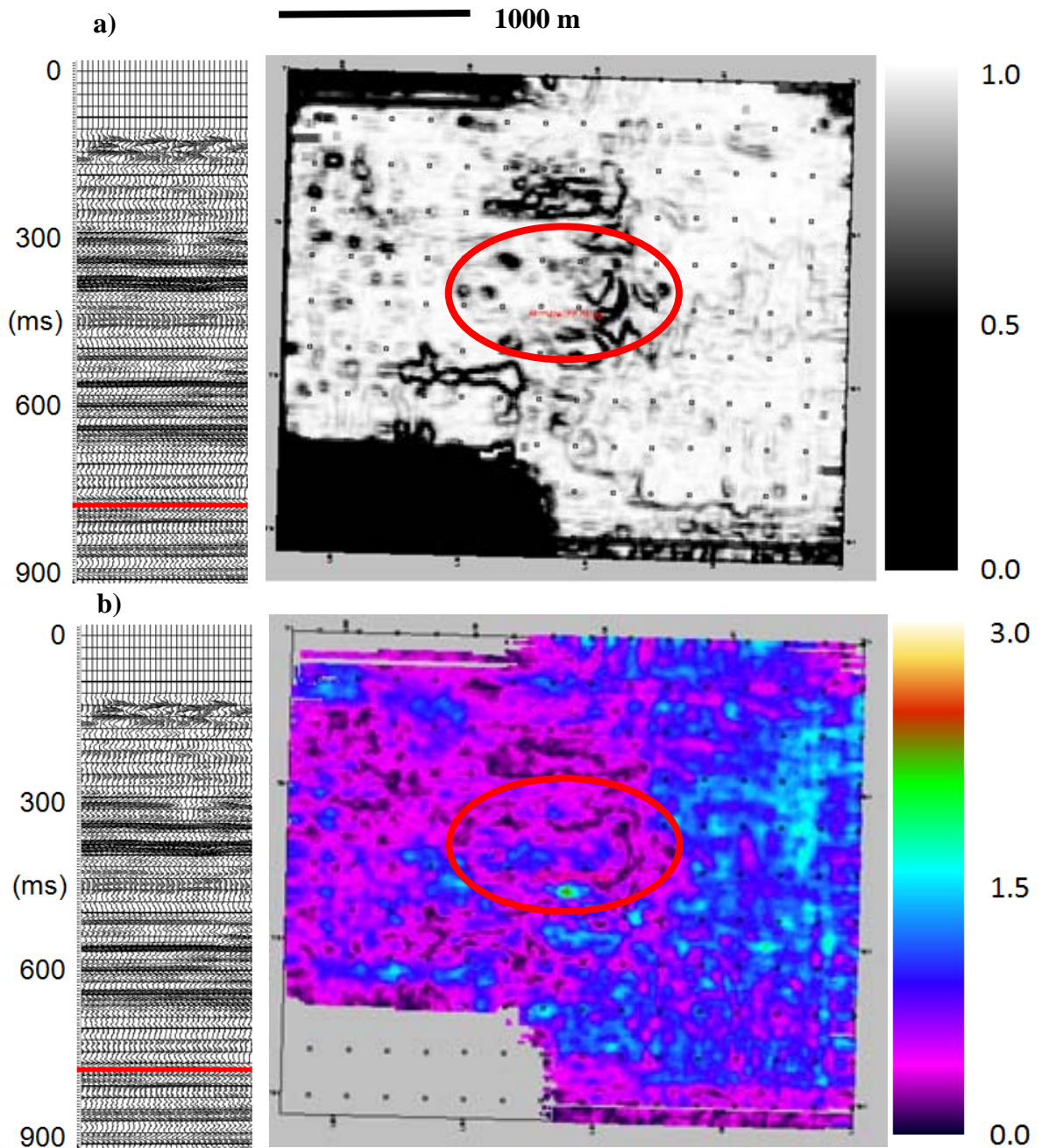


**Figure 4.5 – Baseline PP semblance (a) and amplitude envelope (b) time slices through the top of the Prairie Evaporite Formation (774 ms) show the same correlation between low semblance and low amplitude envelope values. There is a low semblance area which surrounds the area interpreted to contain randomly oriented fractures seen in Figure 4.3 and Figure 4.4.**

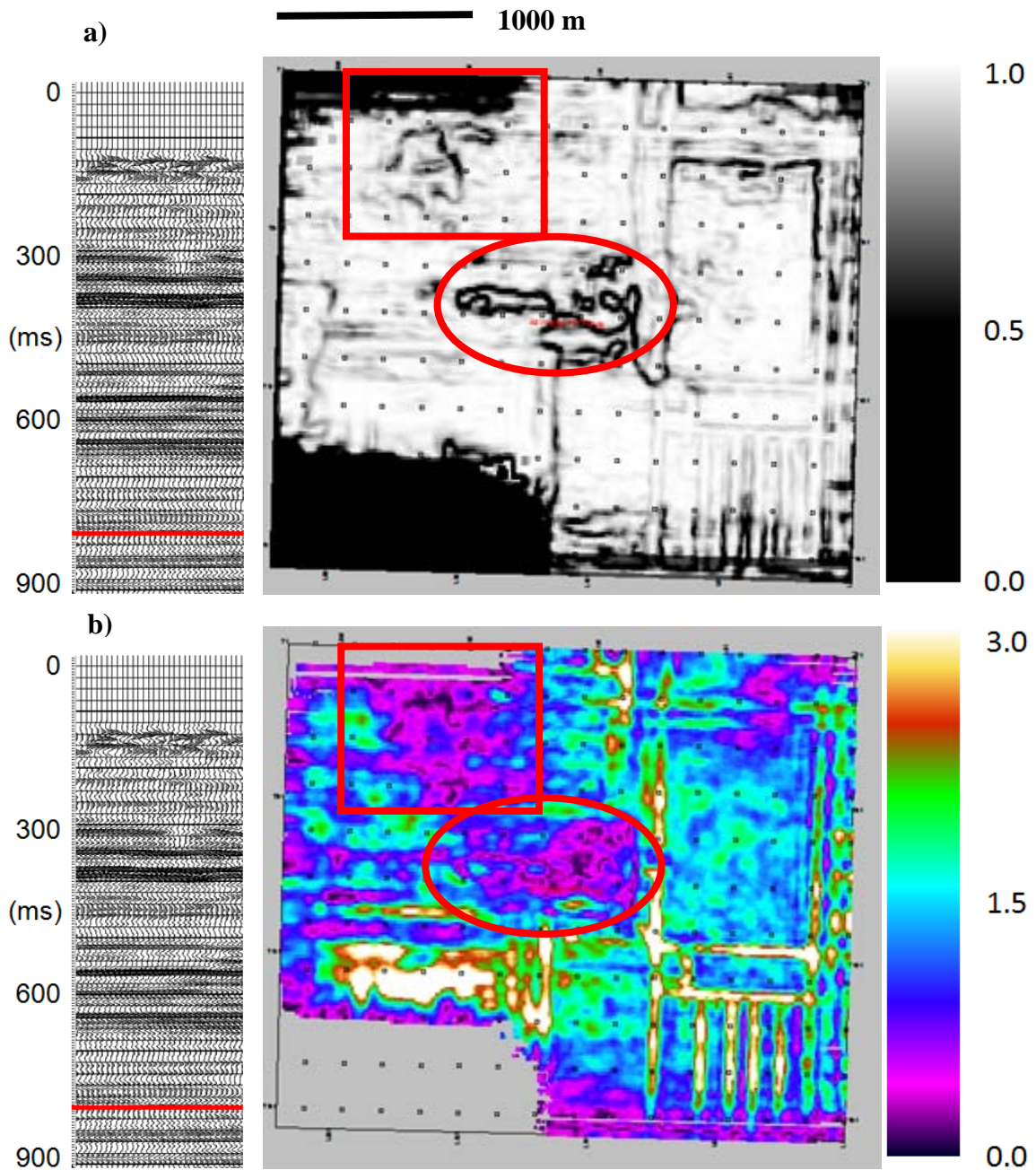


**Figure 4.6 - Baseline PP semblance (a) and amplitude envelope (b) time slices through the Prairie Evaporite Formation (792 ms) clearly show the mine rooms. In the centre of the slice through the amplitude envelope volume, there is a low value anomaly which is significantly lower than that of the rest of the area. This anomaly has been interpreted to be the result of subsurface fracturing which does not have a preferential orientation.**

Upon analysis of the amplitude envelope volume from the baseline PP full azimuth stack, it was evident that there were coherent amplitude envelope anomalies associated with mining operations or natural and/or induced fracture networks, as shown in Figures 4.3 and 4.4. Figure 4.9 shows the semblance and amplitude envelope attributes from the baseline PS volume, which is equivalent in depth to the PP semblance and amplitude envelope slices in Figure 4.3, located just below the top of the Souris River Formation. The semblance time slice (Figure 4.9a) shows an anomaly in the centre of the dataset which corresponds to the low amplitude, low velocity anomaly in the PP volume. The amplitude envelope time slice (Figure 4.9b) does not show the same anomaly in this interval. At this point it was clear that the low signal-to-noise ratio of the PS volume was having an effect on the quality of the semblance and amplitude envelope attributes which makes them less useful than those from the PP volumes.

The semblance time slice through the Prairie Evaporite Formation in the PP seismic volume (Figure 4.5) is interpreted to show mine workings surrounding a highly fractured area (red circle). The PS semblance time slice through the top of the Prairie Evaporite Formation at 1426 ms (Figure 4.10) shows a high semblance value in the centre of the dataset, surrounded by lower semblance in a shape similar to the fracture induced anomaly in the PP seismic volume. The amplitude envelope time slice at the top of the Prairie Evaporite Formation shows high values in north-south trends which are indicative of mining operations. Areas of low values (less than 1.0) occur where mine rooms are less finely spaced.

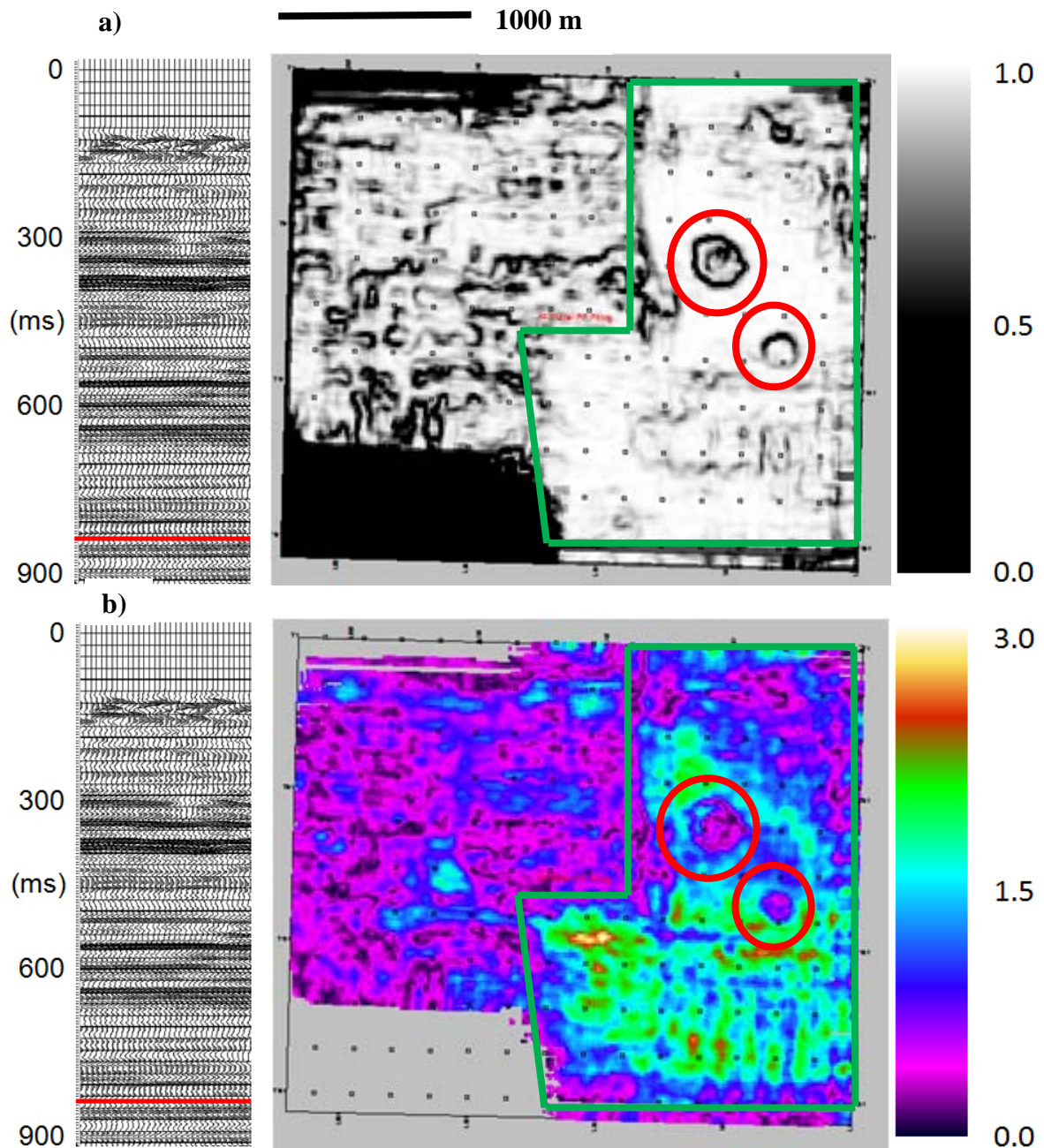


**Figure 4.7 - Baseline PP semblance (a) and amplitude envelope (b) time slices through the Prairie Evaporite Formation (836 ms) shows two carbonate reefs (red circles) on the eastern side of the survey. The slice through the amplitude envelope volume (b) outlines a carbonate mound (green box) with amplitudes between 1.0 and 2.5. The western side of the survey, to the west of the carbonate mound, has a lower average amplitude envelope value between 0.0 and 0.5.**

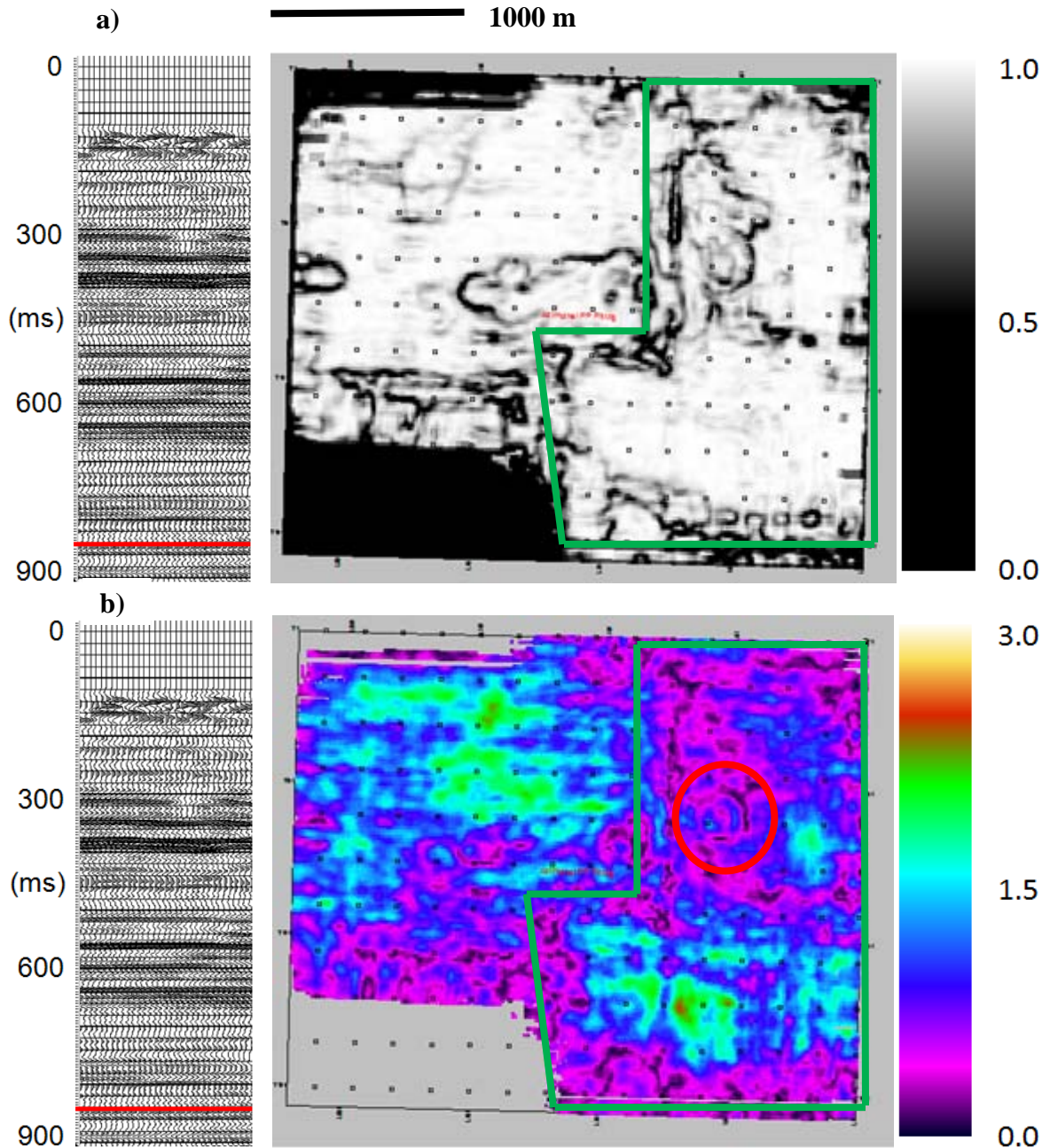


**Figure 4.8 - Baseline PP semblance (a) and amplitude envelope (b) time slices through the top of the Winnipegosis Formation (848 ms) shows the outline of one of the reefs from the slices in Figure 4.7 (red circle). There is no correlation between amplitude envelope and semblance at this level, but the semblance time slice (a) still shows the outline of the low amplitude, low velocity anomaly in the centre of the dataset (triangle) and the outline of the carbonate mound feature (green box).**

The semblance and amplitude time slices through the middle of the Prairie Evaporite Formation (Figure 4.11) show a single reef structure (northern red circle) which corresponds to one of the two reefs found in the PP semblance and amplitude slices (Figure 4.7). The red circle in the south is the location of the second reef found in the PP volume which does not appear in either the semblance or amplitude envelope time slices even though the PS time slices at 1474 ms correspond to the PP time slices at 836 ms.

The red ellipse in the centre of both time slices corresponds to the area interpreted to have increased fracture density interpreted previously, but there is no significant anomaly in either slice which would suggest the presence of a fractured zone at this level in the PS semblance and amplitude envelope volumes.

The semblance and amplitude time slices at the top of the Winnipegosis Formation (1496 ms), do not show the two smaller reef structures in the PS volumes that were seen in the PP volumes. Neither, the semblance time slice (Figure 4.12a), nor the amplitude envelope time slice (Figure 4.12b) do not show the location of what was interpreted to be the edge of the carbonate mound in the PP semblance and amplitude envelope volumes (Figure 4.8). In the semblance volume (Figure 4.12a) the central semblance anomaly corresponds with the fractured carbonates interpreted in the PP volumes and in the upper section of the PS semblance volume.

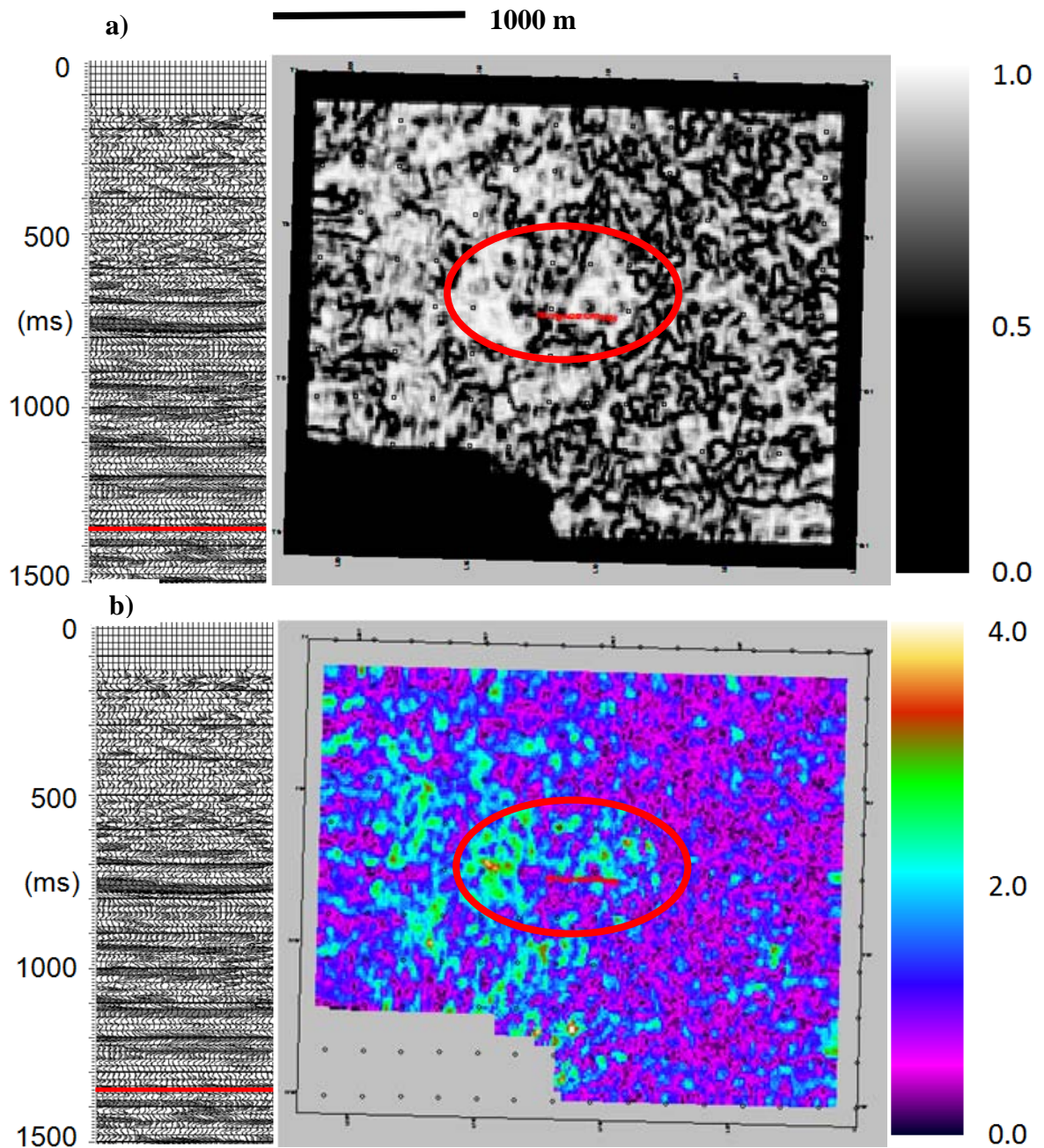


**Figure 4.9 – Baseline PS semblance (a) and amplitude envelope (b) time slices just below the top of the Souris River Formation (1350 ms) shows the presence of a high semblance, high amplitude envelope anomaly in the same stratigraphic location as the zone of high fracture density from Figure 4.3.**

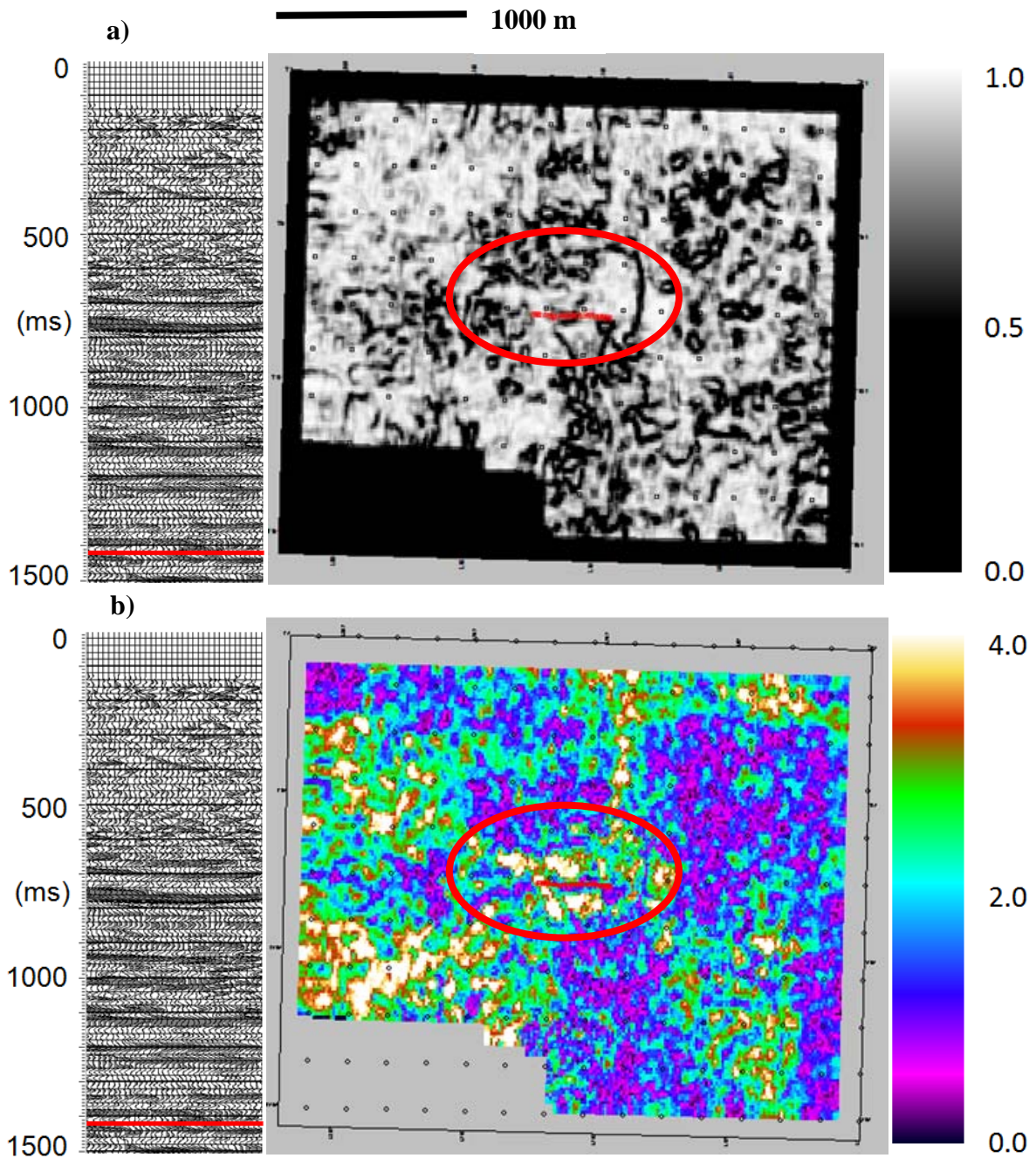


**Figure 4.10 – Baseline PS semblance (a) and amplitude envelope (b) time slices at the top of the Prairie Evaporite Formation (1426 ms) shows the presence of a high semblance, high amplitude envelope anomaly in the same stratigraphic location as the zone of high fracture density from Figure 4.5. The amplitude envelope slice also displays high value anomalies associated with areas with a higher density of mining operations.**

### ***4.2.3 Time-Lapse Seismic Attribute Analysis***

#### **4.2.3.1 PP Seismic Attribute Analysis**

The semblance and amplitude envelope attributes were also calculated for the monitor PP full azimuth stack volume over the same interval as the baseline volume. Comparing the baseline and monitor attributes allows interpreters to determine where change has occurred in the subsurface. The visual comparison of the semblance and amplitude envelope seismic attributes calculated from the monitor volume (Figure 4.13) to those from the baseline volume (Figure 4.6) yields little difference between the volumes. By subtracting the monitor volume from the baseline volume a new difference volume was created. Next, semblance and amplitude envelope were calculated for the difference volume.

Figure 4.14 shows the semblance (a) and amplitude envelope (b) attributes for the differenced seismic volume through the Prairie Evaporite Formation at 792 ms. These slices clearly show some of the mine workings visible in the semblance slices from the baseline (Figure 4.6) and monitor (Figure 4.13) volumes in the southeast of the survey area (red box in Figure 4.13 and Figure 4.14). The semblance time slice also shows mine rooms to the north of the central anomaly (green box in Figure 4.13 and Figure 4.14) which were not as clearly visible in the semblance time slices at 792 ms calculated from the original baseline and monitor volumes.

In Figure 4.15, the semblance and amplitude envelope difference time slices show that there was little difference between the baseline and monitor semblance and amplitude envelopes at this level (836 ms). The semblance difference slice does not show any information corresponding to the low amplitude, low velocity anomaly, but the amplitude

envelope difference slice shows a high amplitude envelope difference at the southeast edge of the anomaly. At this level, two reef complexes were interpreted in Figure 4.7, these reef complexes are not visible in the semblance and amplitude envelope attributes from the difference volume, which indicates that their properties did not change over the course of the two surveys, as is to be expected.

At the Winnipegosis Formation (848 ms) (Figure 4.16) the amplitude envelope slice through the difference volume shows a high amplitude envelope value through the centre of the dataset where the low amplitude, low velocity anomaly exists. The semblance time slice does not show any anomalies in the centre of the study area. It does show areas of high correlation between baseline and monitor volumes to the northwest and an area of low correlation in the southeast of the survey area.

#### 4.2.3.2 PS Seismic Attribute Analysis

The PS seismic attributes differ significantly between vintages both visually, and especially, once the difference volume between the baseline and monitor volumes is calculated and the semblance and amplitude envelope attributes are extracted.

Through the visual inspection of the semblance and amplitude envelope time slices, there appears to be very little difference at the top of the Souris River Formation. The top of the Prairie Evaporite Formation shows significant differences in low semblance anomaly trends through the central low velocity anomaly, where the amplitude envelope time slices remain relatively unchanged between the baseline (Figure 4.10) and monitor (Figure 4.17) surveys.

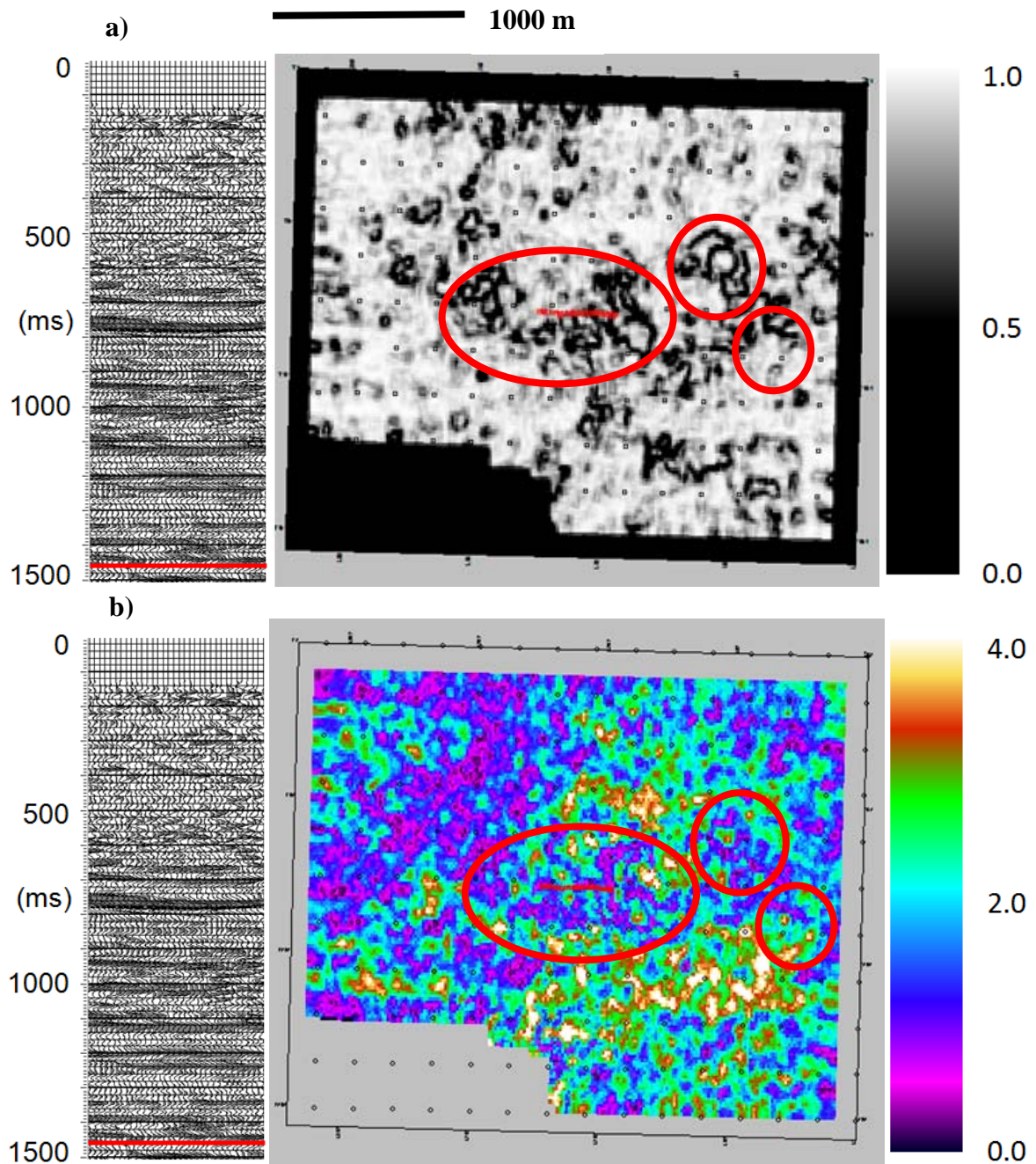


**Figure 4.11 – Baseline PS semblance (a) and amplitude envelope (b) time slices through the Prairie Evaporite Formation (1474 ms) does not show the same amplitude envelope anomalies seen at the top of the Prairie Evaporite Formation (red ellipse). The semblance time slice shows one of the two carbonate reefs in the Winnipegosis Formation, but both carbonate reefs are not visible in the amplitude envelope time slice (two red circles).**

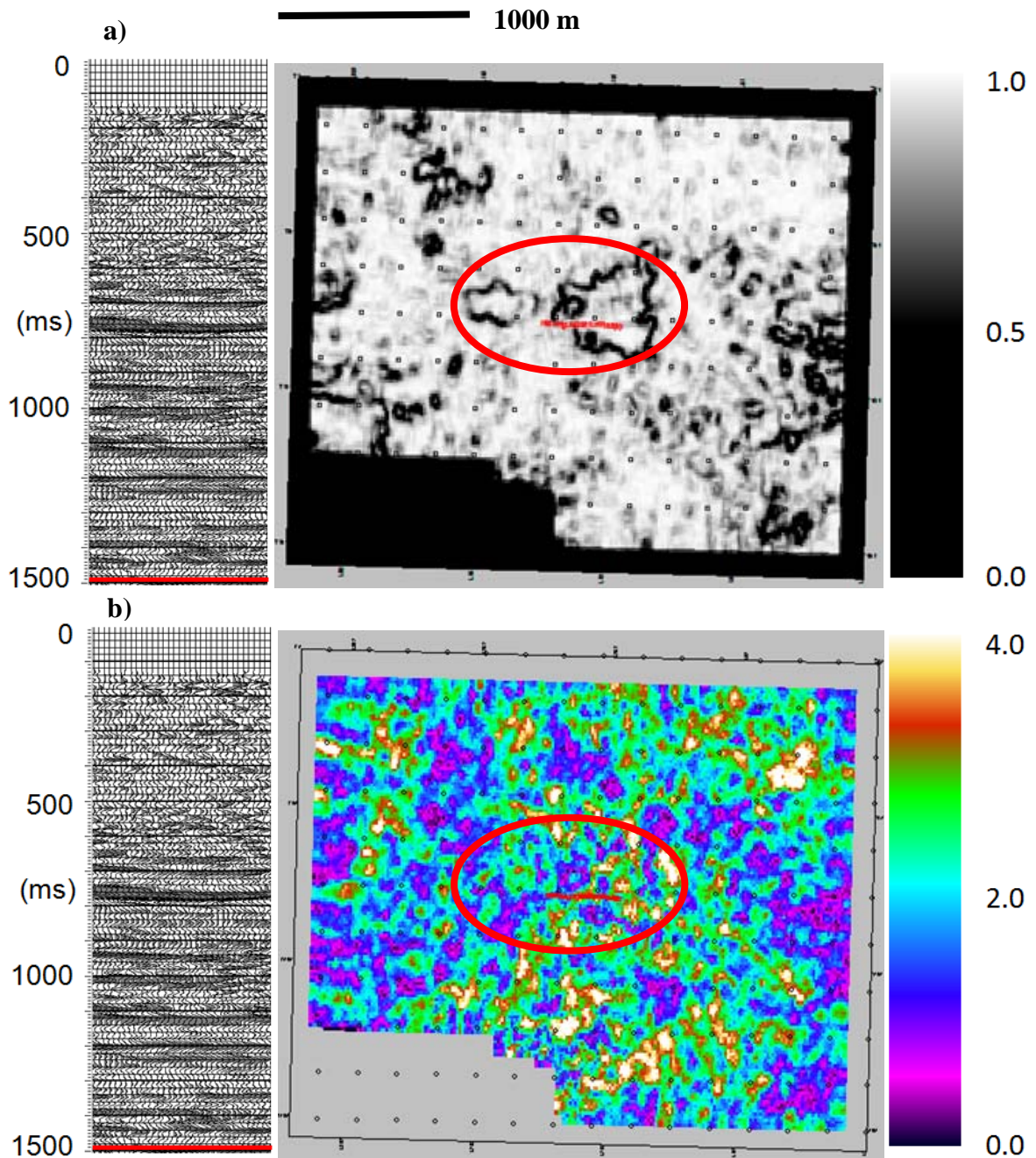


**Figure 4.12 – Baseline PS semblance (a) and amplitude envelope (b) time slices at the top of the Winnipegosis Formation (1496 ms). The semblance time slice shows the presence of a high semblance, high amplitude envelope anomaly previously interpreted as a zone of high fracture density seen in the above figures. The amplitude envelope time slice does not show the same anomaly.**

Time slices through the middle of the Prairie Evaporite Formation (1474 ms) show an overall reduction in semblance, and it is also more difficult to determine the location of two reef complexes in the monitor survey (Figure 4.18) which were clearly visible in the baseline volume (Figure 4.11).

The largest visible difference between the baseline and monitor PS volumes comes at the top of the Winnipegosis Formation (1496 ms). The size of the central semblance anomaly in the monitor volume (Figure 4.19) covers a larger areal extent than that of the baseline survey (Figure 4.12). The western most edge of the anomaly also shows a more accentuated low semblance feature which has grown over time. The amplitude envelope time slice from the monitor volumes (Figure 4.19) also shows an anomaly with a high amplitude envelope value which corresponds to the low velocity anomaly in the centre of the study area, as was not present in the baseline survey (Figure 4.12).

The semblance and amplitude envelope attributes calculated from the radial component difference volume provide the ability to quantitatively measure the changes which occur between the two vintages of PS volumes. In general, the amplitude envelope contains higher values than expected as the amplitude envelope calculated from the PP difference volume had significantly lower values than the amplitude envelope volumes from the two vintages.

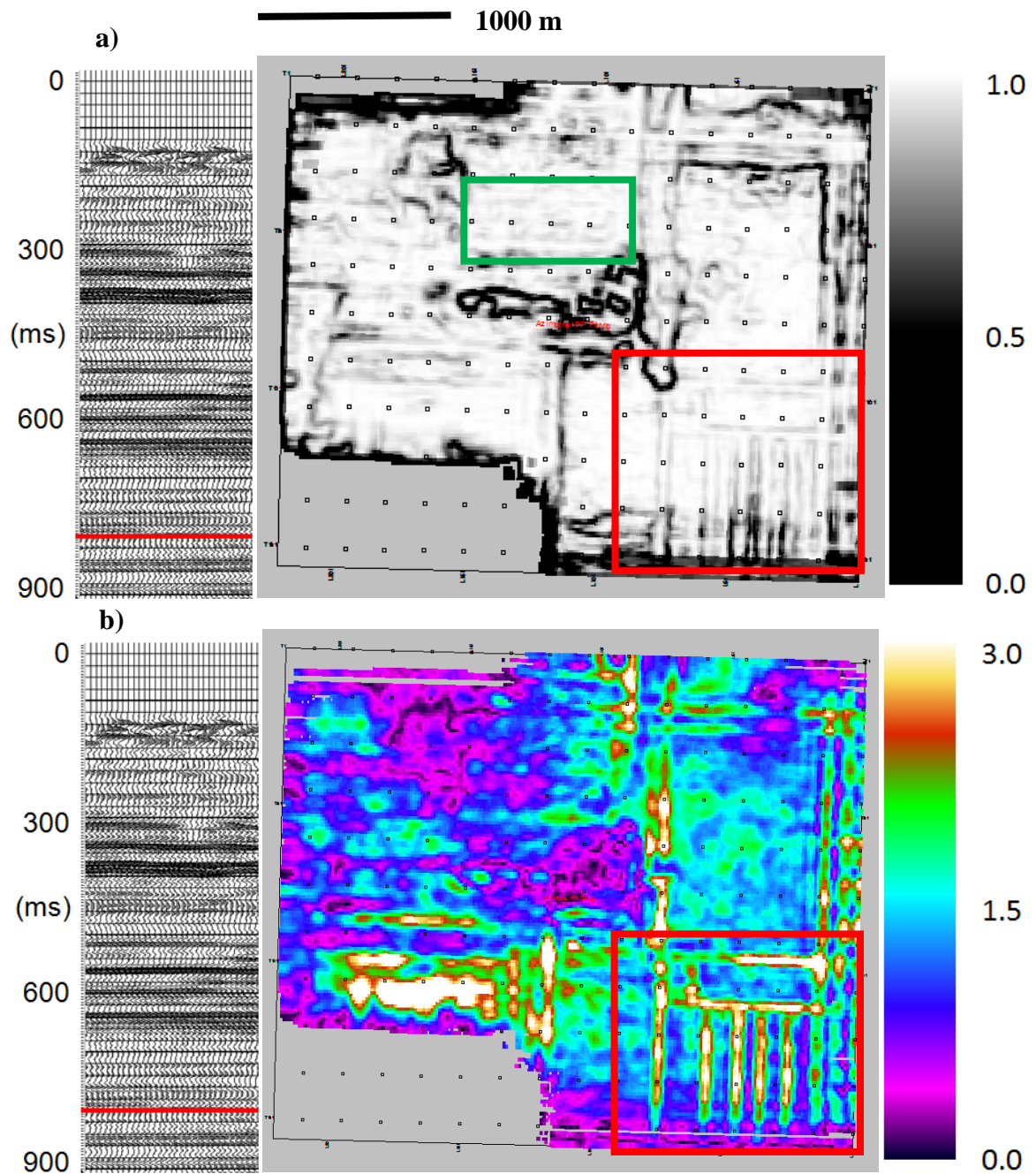


**Figure 4.13 – Monitor PP semblance (a) and amplitude envelope (b) time slices through the Prairie Evaporite Formation (792 ms) clearly show the mine rooms. In the centre of the slice through the amplitude envelope volume, there is a low value anomaly which is significantly lower than that of the rest of the area. There is little difference between the anomaly in the baseline and monitor volumes. The mine workings to the southeast (red box) are highlighted in both vintages where the mine workings to the north (green box) do not show mine workings in the semblance volume.**

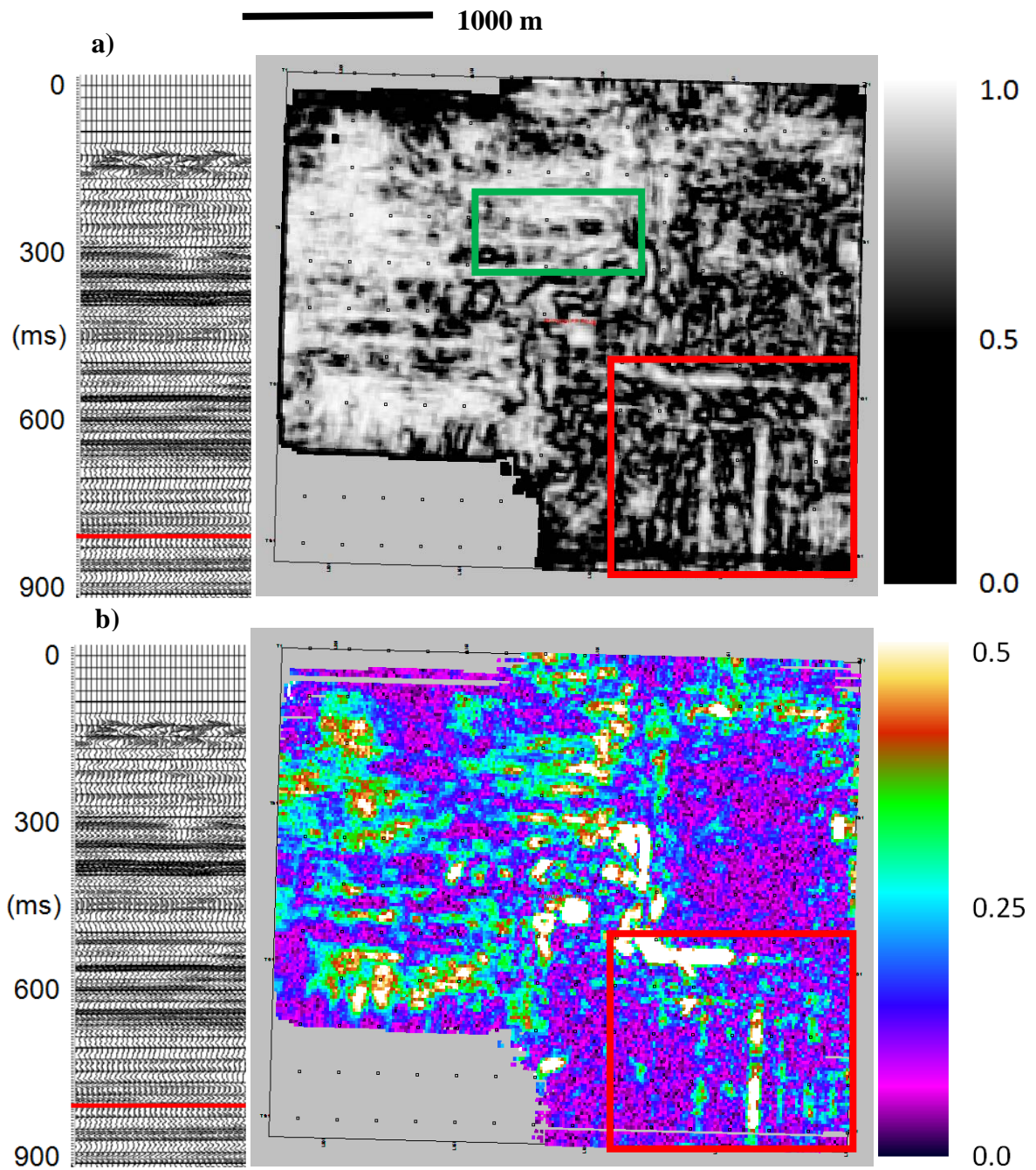


**Figure 4.14 –Semblance (a) and amplitude envelope (b) difference between the PP baseline-monitor surveys at the top of the Prairie Evaporite Formation (792 ms). The red box highlights the time-lapse difference between the semblance and amplitude envelope volumes. The green box highlights mine workings which were not visible in either semblance vintage.**

The time slices through the Prairie Evaporite Formation at 1474 ms (Figure 4.20) outline the carbonate mound feature to the east of the survey area very well (green triangle), while the central low velocity anomaly presents itself as an area of chaotic low semblance. The amplitude envelope time slice does not show any significant anomalies which exhibit a particular trend with respect to the anomalies of interest although, low amplitude envelope values do appear to correspond to areas of lowest semblance.

At the top of the Winnipegosis Formation, the semblance and amplitude envelope time slices through the radial difference volume (Figure 4.21) show an anomaly associated with the low velocity anomaly through the centre of the study area (red ellipses). The semblance anomaly is highlighted by low semblance values surrounded, where the amplitude envelope anomaly is isolated to the eastern edge of the semblance anomaly and is made up of high amplitude envelope values.

### **4.3 Summary**

The use of seismic attributes has become a staple in the seismic interpreter's toolbox since attributes were proven to be an effective way to quantify the location of gas, major fault systems and sedimentary structures using seismic data. In this chapter, amplitude envelope, an attribute derived from complex seismic trace analysis, and semblance were used to attempt to further investigate a low velocity anomaly in the centre of the study area.

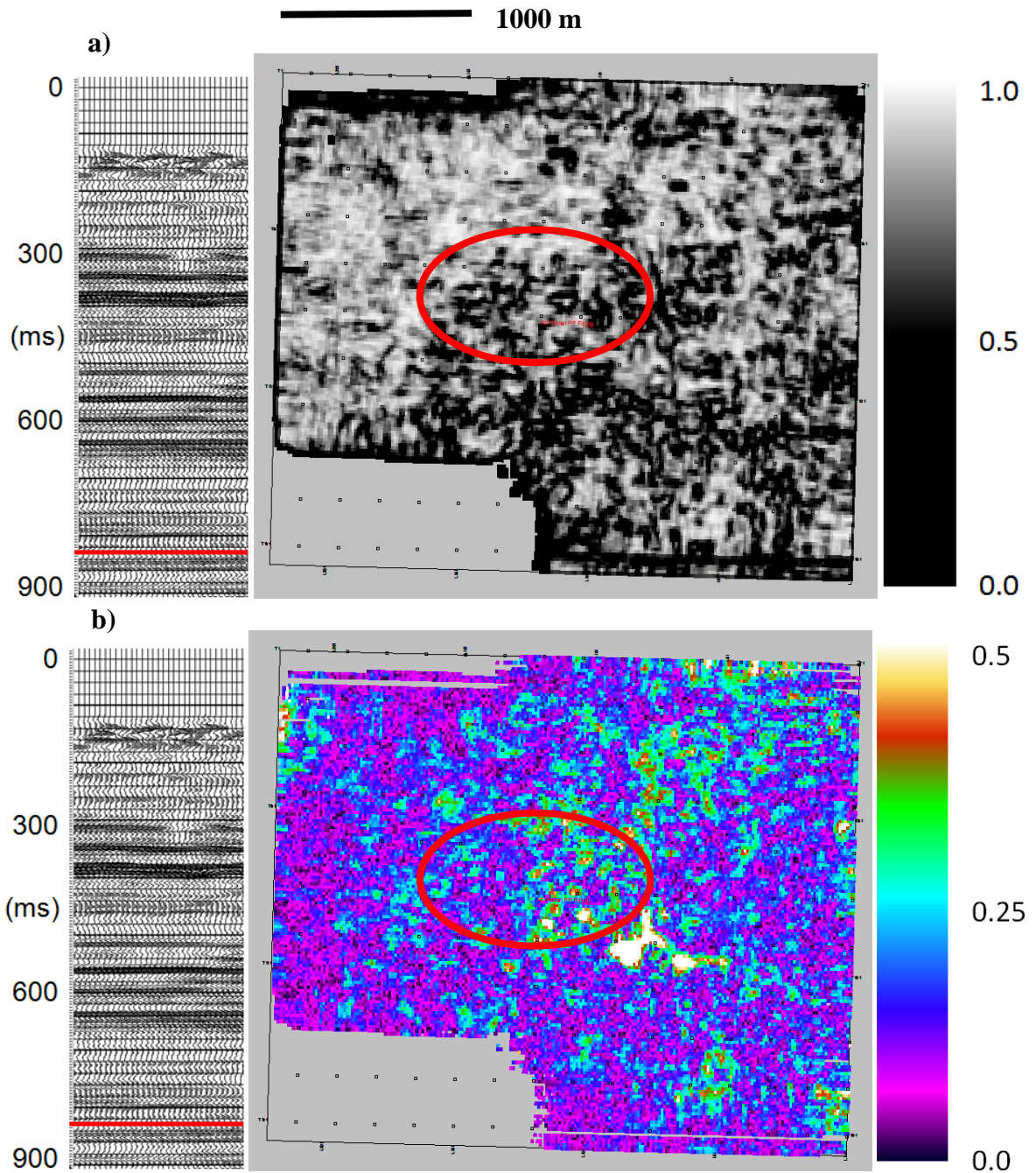


**Figure 4.15 – Semblance (a) and amplitude envelope (b) difference between the PP baseline-monitor surveys through the Prairie Evaporite Formation (836 ms). The red ellipse encompasses the area where the low amplitude, low velocity is found in the true semblance and amplitude envelope volumes. Note there is very little time-lapse difference in this area at this level, however, the amplitude envelope shows a high difference value to the southeast of the area.**

The time slices through the PP semblance volume shows an area of low coherence at 720 ms, just below the top of the Souris River Formation. This area of low coherence corresponds to the area of high  $V_p/V_s$  in this area, as outlined in the previous chapter, and was interpreted to be an area of intensely fractured carbonates. The amplitude envelope time slice at the same level shows a low amplitude anomaly in the same location with the same shape of the low semblance anomaly. This feature extends down through the Dawson Bay Formation and the Prairie Evaporite Formation where it become more difficult to interpret once below the mine level. At the top of the Winnipegosis Formation (848 ms PP time) the northern and western edges of the anomaly is visible in the semblance volume, but the southern and eastern edges are difficult to delineate due to the presence of an interpreted carbonate mound structure.

In the PS semblance volume, it is generally possible to pick out the same anomaly through the same stratigraphic intervals although it is difficult through the Prairie Evaporite Formation, just as in the PP semblance volume. The amplitude envelope is much less helpful in the PS case since it is not possible to delineate the anomaly at any level. This is likely due to the lower signal-to-noise of the PS volume. The semblance time slices through the top of the Prairie Evaporite Formation, the middle of the Prairie Evaporite Formation and the top of the Winnipegosis Formation show the low velocity anomaly in the centre of the study area. The time slice through the middle of the Prairie Evaporite Formation also shows one of the two reef complexes. The amplitude envelope time slice at the top of the Prairie Evaporite Formation has high values where the mining operations are located, however because of the low signal-to-noise ratio of the PS data the mine rooms were not as clearly resolved as in the PP volume.

Time-lapse analysis of the PP attribute volumes showed that there was very little difference in the semblance and amplitude envelope values when visually inspected. Analysis of the same attributes calculated from the difference volume showed that there were quantitative differences between the baseline and monitor volumes. Specifically, the differenced amplitude envelope and semblance attributes were able to delineate areas of the mine workings at the top of the Prairie Evaporite Formation which is likely the result of changes in the subsurface due to the ongoing mining operation.

The time-lapse analysis of the PS seismic attribute volumes visually showed a large difference between the two vintages at the top of the Winnipegosis Formation. The semblance anomaly was significantly larger in the monitor volume with a more developed, secondary anomaly to the west. The monitor amplitude envelope volume exhibited values which were significantly larger than those of the baseline volume in the vicinity of the central low velocity anomaly.

These results lead to the conclusion that the fracturing propagates upwards from an unknown source to the Souris River Formation. The source of the fracturing is thought to be either the Dawson Bay Formation or the mine workings in the area, but it is difficult to pinpoint exactly where the fracturing originates because the velocity anomaly in the seismic volumes extend through the Winnipegosis Formation.

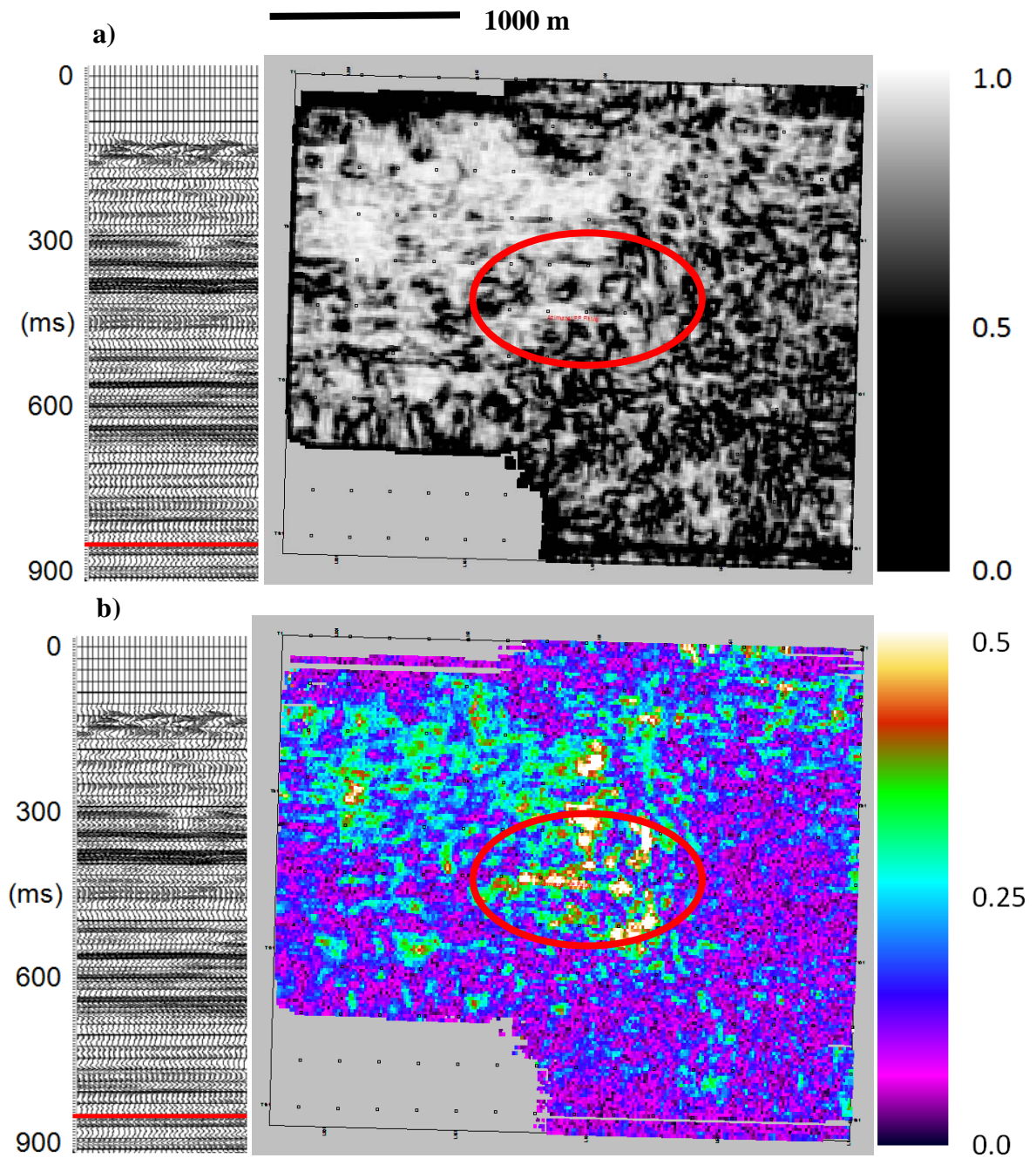


**Figure 4.16 – Semblance (a) and amplitude envelope (b) difference between the PP baseline-monitor surveys at the top of the Winnipegosis Formation (848 ms). The red ellipse shows the area where a low amplitude, low velocity anomaly was interpreted. There is little difference between vintages in the semblance time slice, where the amplitude envelope shows a high value difference between the baseline and monitor volumes.**

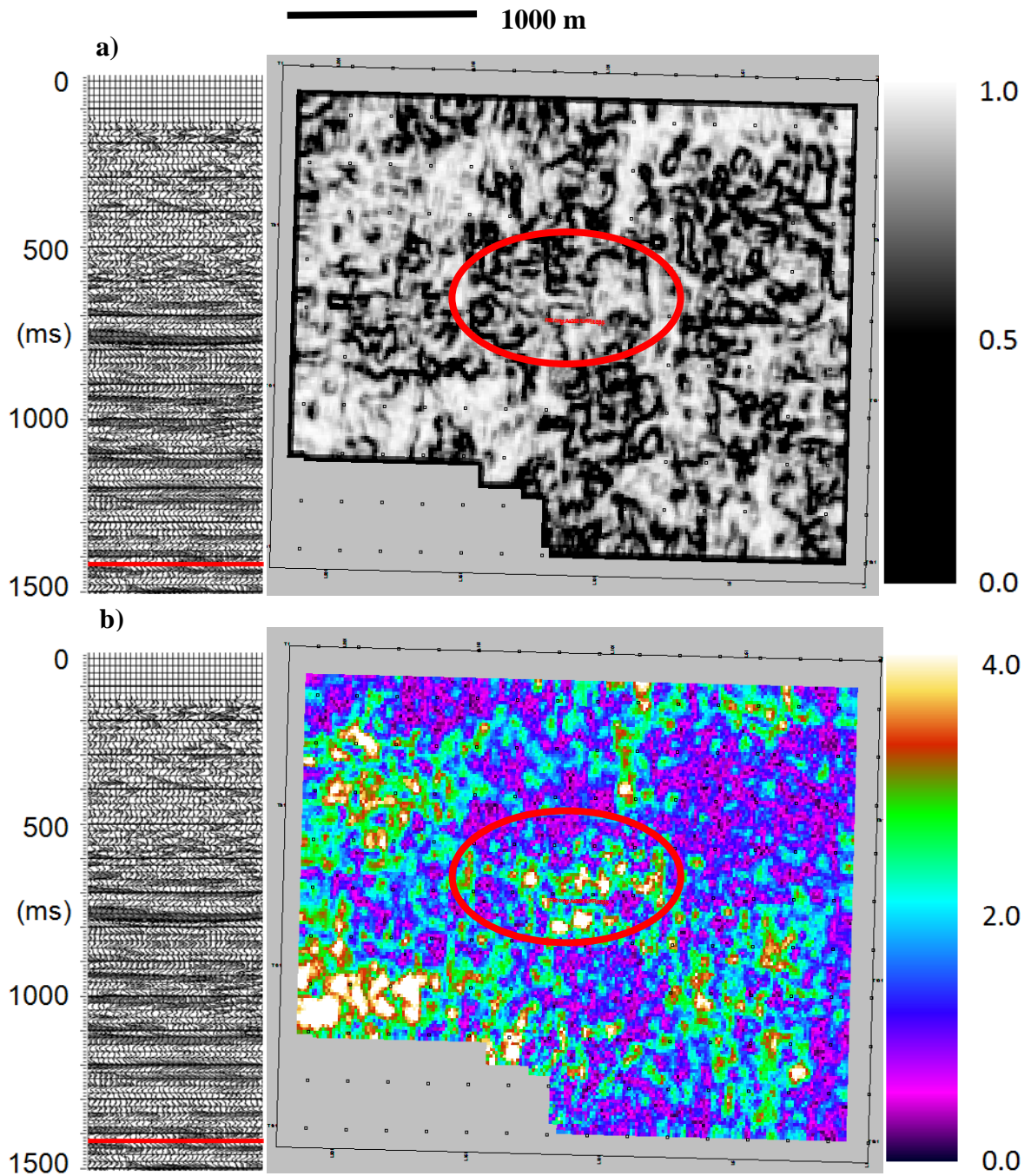


**Figure 4.17 – Monitor PS semblance (a) and amplitude envelope (b) time slices through the top of the Prairie Evaporite Formation (1426 ms). The red ellipse encompasses the area where a low velocity anomaly was interpreted. There is a small semblance anomaly, and a high amplitude envelope value associated with this anomaly at this level. The amplitude envelope slice also highlights the mine trends which are located in the areas of high values (amplitude envelope of 3.0-4.0).**

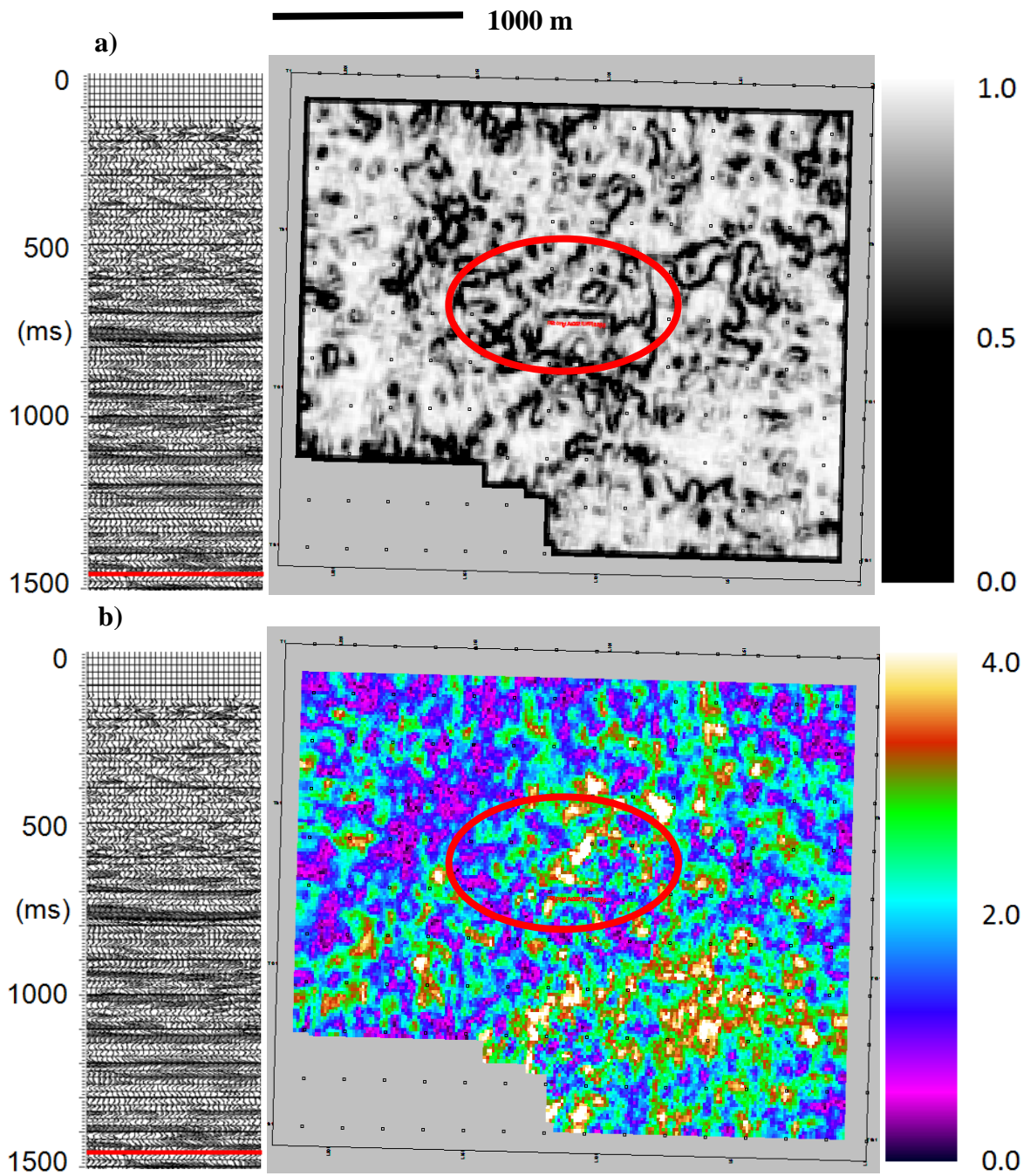


**Figure 4.18 – Monitor PS semblance (a) and amplitude envelope (b) time slices through the Prairie Evaporite Formation (1474 ms). The red ellipse shows the area where the previously interpreted low velocity anomaly is located. The semblance and amplitude envelope time slices at this level do not have an anomaly associated with this anomaly. The semblance time slice does not image the reef complexes which were seen in the baseline time slice at this level (Figure 4.11).**

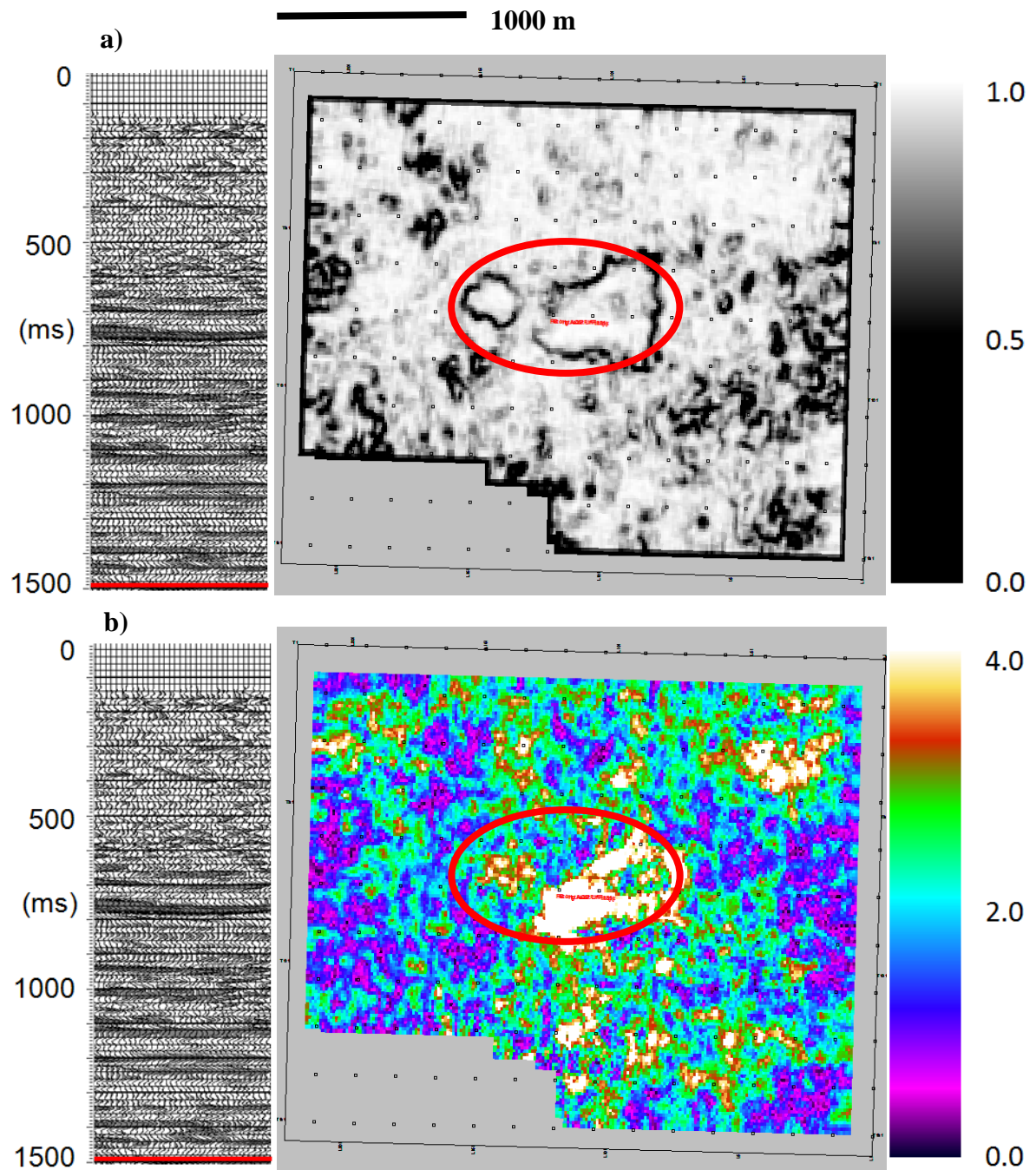


**Figure 4.19 – Monitor PS semblance (a) and amplitude envelope (b) at the top of the Winnipegosis Formation (1496 ms). The monitor semblance time slice shows an increase in size of the low velocity anomaly seen in Figure 4.12. The amplitude envelope time slice has a significantly increased value through the central low velocity anomaly (value of 4.0) which is not present in the baseline time slice at this level.**

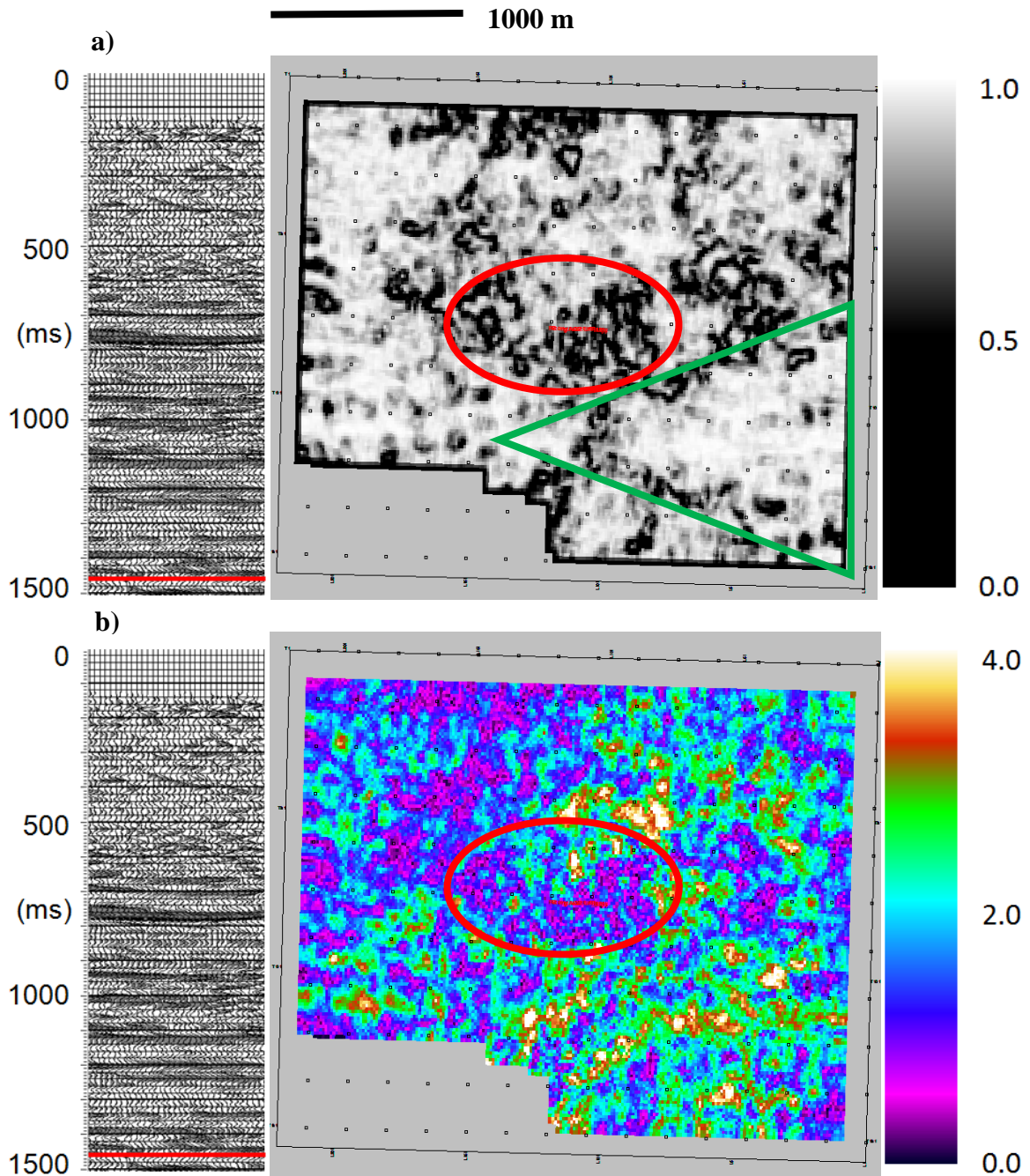


**Figure 4.20 – Semblance (a) and amplitude envelope (b) difference between the PS baseline-monitor surveys through the Prairie Evaporite Formation (1474 ms). The semblance time slice shows a low semblance where the low velocity anomaly is located in the centre of the study area (red ellipse) and the carbonate mound feature previously interpreted to be present in the southeast of the study area (green triangle). The amplitude envelope time slice has a low value anomaly associated with the low velocity anomaly in the centre of the study area.**

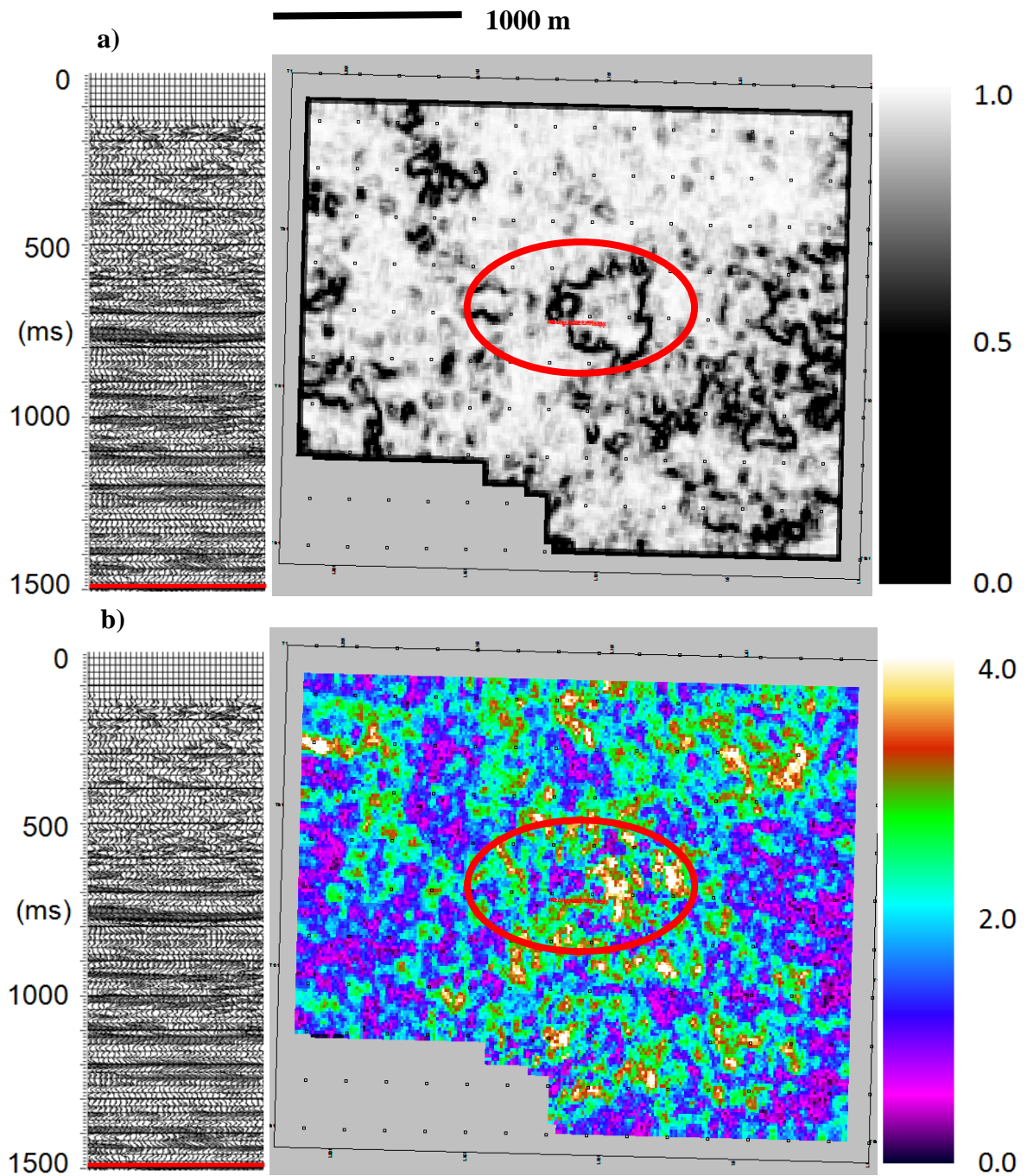


**Figure 4.21 – Semblance (a) and amplitude envelope (b) difference between the PS baseline-monitor surveys at the top of the Winnipegosis Formation (1496 ms). The semblance difference shows the same low velocity anomaly in the centre of the study area where the amplitude envelope has a high value anomaly to the east of the same low velocity anomaly (red ellipse).**

## Chapter Five: **DISCUSSION AND CONCLUSIONS**

### **5.1 Discussion**

The combination of travel-time,  $V_p/V_s$  and seismic attribute analysis has allowed for the characterization of a low velocity, low amplitude seismic anomaly in the central part of the study area. Chapter 2 focused on travel-time analysis of four major horizons and this was interpreted to determine the extent of fracture-induced seismic anisotropy within the Devonian Dawson Bay Formation. The fractures in the study area are subvertical in nature, and reduce seismic velocity when a seismic wave travels across the fracture planes. Detection of preferentially oriented fractures was achieved by taking the difference between horizons picked on azimuthally sectorized seismic volumes. The largest travel-time differences between horizons were seen in volumes which were made up of orthogonal azimuths, and therefore showed the general orientation of preferentially oriented fracture networks through the area. The resolution of the azimuthal volumes, however, was limited due to the 45 degree aperture of reciprocal source-receiver ray paths used to produce these sectorized volumes. Using the PP azimuthally sectorized seismic volumes, the travel-time difference method detected the influence of mine workings in the southeast of the study area within the Prairie Evaporite Formation. The trend of the mining operations are oriented from north to south, and the travel-time differences were detected, as is to be expected, when the 0°&180° and 90°&270° sectorized volumes were differenced. Differencing the Winnipegosis Formation horizons shows travel-time anomalies which correspond to fractures which are interpreted to be oriented parallel to the edge of the mining operations in the centre of the study area. These fractures are thought to be the result of subsurface stress changes brought on by mining operations, which explains their high density and

preferential orientation, and are seen in the 0°-180°-90°-270° travel-time difference plot. The 45°-225°-135°-315° travel-time difference plot at the Winnipegosis level also exhibits travel-time differences in the centre of the study area, where the low amplitude, low velocity anomaly is present. Determining that large travel-time differences exist in both orientations means that within the low amplitude, low velocity anomaly in the centre of the dataset high density fracturing is not limited to a narrow set of azimuths. The PS travel-time difference plots do not show significant azimuthal anisotropy, but this is likely because the PS horizons were difficult to pick due to the higher noise level associated with the PS seismic volumes and thus the differencing method suffers from reduced temporal resolution.

The registration of the PP and PS volumes allowed for the generation of the interval Vp/Vs attribute. The well tie process made it possible to correlate a seismic event with a geological interface in PP seismic volumes, but in the PS volume the selection of a seismic pick representing the same geological interface was more difficult due to the difference in bandwidth between the PP and PS volumes. The placement of the PP and PS horizons to represent the same geological interface is a critical part of the well tie process, and slight errors in horizon placement can have a large impact on the quality of the Vp/Vs attribute which is produced through the registration process. In chapter 3 I showed that an error in PS horizon placement as small as 7 ms can change the Vp/Vs by as much as 0.3, which is a 15 percent change in the base Vp/Vs value of 2.0. Such errors should be evident in the horizon matching process and acceptable values of interval Vp/Vs should be determined before starting the registration process. Confidence in the PP and PS synthetic well ties, and applying slight bulk shifts to several of the PS horizons resulted in a high quality registration with Vp/Vs values within the appropriate range for carbonates. The regions

where the  $V_p/V_s$  exceeded the acceptable limits were isolated to the low velocity, low amplitude anomaly in the centre of the dataset. The area of anomalously high  $V_p/V_s$  values was determined to be located within the Dawson Bay Formation, above the Prairie Evaporite Formation, and was interpreted to be the result of randomly oriented vertical fractures, since there was no distinctive azimuthal trend determined in this region. The time-lapse analysis of the  $V_p/V_s$  attributes showed an increase in  $V_p/V_s$  between the baseline and monitor surveys as well as an area where a high  $V_p/V_s$  anomaly appeared to the west of the original anomaly.

Seismic attributes were used to define the spatial extent of the low velocity anomaly through the generation of two volume attributes, semblance and amplitude envelope, for the PP and PS full azimuth volumes. The PP amplitude envelope and semblance volumes show the outline of the low velocity anomaly at time slices through 720 ms, which is just below the top of the Souris River Formation and which propagates to the bottom of the section. The semblance anomaly is present because the area of low velocity increases the travel-times associated with the events at and below the layer where fractures reduce the seismic velocity, whereas outside the area of low velocity the travel-times remain unchanged. The amplitude envelope anomaly is more difficult to interpret, as there could be many causes for such a reduction in seismic amplitudes. The PS attribute analysis yielded uncertain results because there was no amplitude envelope anomaly identified in the PS dataset. This is likely because S-waves respond differently than P-waves to the lithology or fluid which is creating the amplitude reduction in the PP volume.

The PS attribute analysis results coincided with those of the PP volumes whereby the semblance volumes showed the low velocity anomaly present just below the Souris

River Formation at 1350 ms (PS time) and remained present consistently down through the Winnipegosis Formation (1496 ms). The amplitude envelope attribute on the other hand did not exhibit an anomaly in the centre of the study area where the low amplitude, low velocity anomaly is present in the PP amplitude envelope volume. I have interpreted this to mean that S-waves are unaffected by the physical property which is creating the amplitude anomaly in the PP volumes, likely the presence of water or gas. The resolution of the PS seismic attributes was significantly less than that of the PP seismic attributes because of an increased signal-to-noise ratio, making the PS seismic attribute less useful than the PP seismic attributes when it comes to resolving geologic features.

Time-lapse analysis of the PP seismic attributes shows little visual difference between seismic vintages. However, when the attribute analysis is applied to the difference volume, there are several large differences in both the semblance and amplitude envelope volumes. One of the major differences is in the semblance and amplitude envelope slice through the mine level, just below the top of the Prairie Evaporite Formation. The high amplitude envelope value suggests that there were alterations to specific mine rooms in the southeast of the study area between the two vintages. The semblance attribute images several smaller mine rooms to the north of the low amplitude, low velocity anomaly which were difficult to resolve in the two semblance volumes calculated from the two seismic vintages. At the top of the Winnipegosis Formation (848 ms PP time) the amplitude envelope shows high difference values through the low amplitude, low velocity anomaly in the centre of the study area. This difference implies that there was a reduction of amplitude envelope between the two vintages suggesting that the geological property creating the low amplitude anomaly is getting larger.

The time-lapse analysis of the PS seismic attributes showed a significant increase in areal extent of the low velocity anomaly in the centre of the study area at the top of the Winnipegosis Formation compared to the baseline volume and was most easily quantifiable using the semblance attribute. The amplitude envelope through the low velocity anomaly in the centre of the study area showed a much larger amplitude envelope value in the monitor survey than in the baseline survey which was also visible in the amplitude envelope of the difference volume. The difference volume had two major contributions: it showed the low velocity anomaly in the centre of the dataset in both the semblance and amplitude envelope volumes through the Prairie Evaporite Formation (1474 ms) to the top of the Winnipegosis Formation (1496 ms), and it was able to delineate the carbonate mound in the southeast of the Prairie Evaporite Formation (1474 ms). This means that the low velocity anomaly, interpreted to be the result of subsurface fracturing, was changing in size and it is likely that fracture density was increasing over the duration of the time-lapse seismic study.

## **5.2 Conclusions**

The objective of this thesis was to assess the extent of fracture-induced anisotropy in the subsurface using a multicomponent, time-lapse seismic dataset, through the use of travel-time analysis of PP and PS horizons as well as  $V_p/V_s$  and seismic attribute analysis. The main conclusions of this case study are:

- Travel-time analysis showed travel-time differences on the order of 8 ms which have been interpreted to be the result of HTI created by high density, preferentially oriented fractures running parallel to the mining trend. The

anisotropy is identified on the Prairie Evaporite and Winnipegosis difference plots, and in the central region of the study area.

- Travel-time difference plots from the PS volumes did not elucidate evidence for azimuthal anisotropy. The lack of large travel-time differences are thought to be due to the increased level of noise in the PS volumes compared to the PP volumes.
- The lower frequency content in the PS volumes means picking seismic events on peaks or troughs might not correspond to the same geological interface as its PP counterpart. Picking the closest coherent seismic reflector and applying a bulk shift to the horizons corrected this issue.
- Neglecting to apply a bulk shift, or applying an incorrect bulk shift to the PS horizons significantly affects the quality of Vp/Vs analysis. An error of 7 ms is enough to change the Vp/Vs by 0.3, which corresponds to 15 percent of the background Vp/Vs in the study area.
- Vp/Vs is within the acceptable range for carbonates. High values of Vp/Vs are found in the Dawson Bay Formation and correspond to the low velocity, low amplitude anomaly in the centre of the dataset. The magnitude of the high Vp/Vs anomaly increases between the baseline and monitor surveys and this was interpreted to be the result of increased fracture density. The high magnitude Vp/Vs anomaly does not extend past the top of the Dawson Bay Formation in the Vp/Vs volume.

- Semblance and amplitude envelope analysis of the baseline full azimuth PP volume shows a low velocity, low amplitude anomaly at 720 ms, just below the top of the Souris River Formation.
- PS attribute analysis shows the low velocity anomaly in the semblance attribute at 1350 ms which is just below the top of the Souris River Formation. The amplitude envelope attribute from the PS volume does not show an amplitude anomaly in the centre of the study area where the amplitude anomaly is present in the PP amplitude envelope volume. This indicates that fluid in the fractures is creating the amplitude anomaly seen in the PP volume since fluids do not affect the amplitudes of S-waves.
- PS signal-to-noise ratio was significantly less than PP signal-to-noise ratio making resolving geological features using PS seismic attributes very difficult.
- Time-lapse analysis of the semblance and amplitude envelope attributes shows that the central low velocity, low amplitude anomaly has grown over time which is likely due to an increase in fracture density.
- Combining the fracture assessment from  $V_p/V_s$  analysis and seismic attribute analysis leads to the conclusion that fracturing begins in the Dawson Bay Formation and extends vertically upwards to the top of the Souris River Formation.

## REFERENCES

- Al Dulaijan, K., Owusu, J., & Weber, D. (2012). Azimuthal Anisotropy Analysis of Walkaround Vertical Seismic Profiling: A Case Study from Saudi Arabia. *Geophysical Prospecting*, 1082-1094.
- Alford, R., (1986). Shear Data in the presence of Azimuthal Anisotropy: Dilley, Texas. *SEG Annual Meeting Extended Abstracts*. 476-479.
- Anstey, N. (2005). Attributes in Color: The Early Years. *CSEG Recorder*, 12-15.
- Bahorich, M., & Farmer, S. (1995). 3-D Seismic Discontinuity for Faults and Stratigraphic Features: The Coherence Cube. *The Leading Edge*, 1053-1058.
- Balch, A. (1971). Color Sonograms: A New Dimension in Seismic Data Interpretation. *Geophysics*, 1074-1098.
- Barnes, A. (2007). A Tutorial on Complex Seismic Trace Analysis. *Geophysics*, W33-W43.
- Boyd, J. (2012, 03 12). Personal Communication.
- Braun, W. K., & Mathison, J. E. (1986). Mid-Givetian Events in Western Canada: The Dawson Bay - Watt Mountain - "Slave Point" Interlude. *34(4)*.
- Brown, A. (2004). *Interpretation of Three-Dimensional Seismic Data*. Tulsa, OK: Society of Exploration Geophysicists.
- Cen, X. C., & Hersi, S. (2006). Sedimentology, Microfacies Analysis, and Depositional Setting of the Late Devonian Duperow Formation, Southeastern Saskatchewan. *Summary of Investigations 2006, Saskatchewan Geological Survey*.
- Chopra, S. (2002). Coherence Cube and Beyond. *First Break*, 27-33.

- Chopra, S., & Marfurt, K. (2007). Seismic Attributes fo Fault/Fracture Characterization. *CSPG CSEG Convention Extended Abstracts*.
- Chopra, S., & Marfurt, K. (2007). *Seismic Attributes for Prospect Identification and Reservoir Characterization*. Tulsa, OK: Society of Exploration Geophysicists.
- Christopher, J. (1962). The Three Forks Group (Upper Devonian-Kinderhookian) of Southern Saskatchewan. *Three Forks-Belt Mountains Area and Symposium: The Devonian System of Montana and Adjacent Areas*, 67-76.
- Crampin, S. (1981). A Review of Wave Motion in Anisotropic and Cracked Elastic-Media. *Wave Motion*, 343-391.
- Crampin, S. (1985). Evaluation of Anisotropy by Shear-Wave Splitting. *Geophysics*, 142-152.
- Crampin, S., & Lovell, J. (1991). A decade of shear-wave splitting in the Earth's crust: what does it mean? what can we make of it? and what should we do next? *Geophysical Journal International*, 387-407.
- Crampin, S., Lynn, H., & Booth, D. (1989). Shear-Wave VSP's: A Powerful New Tool for Fracture and Reservoir Description. *Journal of Petroleum Technology*, 283-288.
- De Mille, G., Shouldice, J. R., & Nelson, H. W. (1964). Collapse Structures Related to Evaporites of the Prairie Formation, Saskatchewan. *Geological Society of America Bulletin*, 307-316.
- Delbecq, F., Downton, J., & Letizia, M. (2013). A Math-Free Look at Azimuthal Surface Seismic Techniques. *CSEG Recorder*, 20-31.
- Douglas, R. J. (1970). *Geology and Economic Minerals of Canada*. Ottawa: Geological Survey of Canada.

- Dunn, C. E. (1982). *Devonian Dawson Bay Formation in the Saskatoon Potash Mining District, Saskatchewan*. Saskatchewan: Saskatchewan Energy and Mines.
- Edgecombe, R. (2011). Personal Communication.
- Elkibbi, M., & Rial, J. (2003). Shear-wave splitting: an efficient tool to detect 3D fracture patterns at the Geysers, CA. *28th Workshop on Geothermal Reservoir Engineering*.
- Erickson, E. L., Miller, D. E., & Waters, K. H. (1968). Shear-wave Recording using Continuous Signal Methods Part II - Later Experimentation. *Geophysics*, 240-254.
- Fertig, J., & Krajewski, P. (1989). Acquisition and Processing of Pure and Converted Shear Waves Generated by Compressional Wave Sources. *Surveys in Geophysics*, 103-132.
- Fuzesy, L. (1982). Petrology of Potash Ore in the Esterhazy Member of the Middle Devonian Prairie Evaporite in Southeastern Saskatchewan. *Proceedings of the 4th International Williston Basin Symposium*, (pp. 67-73).
- Gardner, G. H., & Harris, M. H. (1968). Velocity and Attenuation of Elastic Waves in Sands. *SPWLA 9th Annual Logging Symposium*.
- Gendzwill, D. J. (1978). Winnipegosis Mounds and Prairie Evaporite Formation of Saskatchewan - Seismic Study. *The American Association of Petroleum Geologists Bulletin*, 73-86.
- Gray, D., & Head, K. (2000). Fracture Detection in the Manderson Field: A 3D AVAZ Case History. *SEG Annual Meeting Extended Abstracts*.
- Gray, D., Boerner, S., Todorovic-Marinic, D., & Zheng, Y. (2003). Analyzing Fractures from Seismic for Improved Drilling Success. *World Oil*.

- Gray, D., Roberts, G., & Head, K. (2002). Recent Advances in Determination of Fracture Strike and Crack Density from P-wave Seismic Data. *The Leading Edge*, 280-285.
- Grimm, R., Lynn, H., Bates, C., Phillips, D., Simon, K., & Beckham, W. (1999). Detection and Analysis of Naturally Fractured Gas Reservoirs: Multi-azimuth Seismic Surveys in the Wind River Basin, Wyoming. *Geophysics*, 1277-1292.
- Gu, C. (1998). *Depositional Environments and Diagenesis of the Devonian Dawson Bay Formation in Saskatchewan and Northwestern Manitoba*. Regina: The University of Saskatchewan.
- Guevara-Ochoa, S., & Cary, P. (2006). Converted Wave Applied to Fracture Detection in the Catatumbo Area, Colombia. *Ciencia, Tecnologia y Futuro*, 57-72.
- Halabura, S. (1982). Depositional environments of the Upper Devonian Birdbear Formation, Saskatchewan. *4th International Williston Basin Symposium*, 113-124.
- Hardage, B. A., DeAngelo, M., & Murray, P. (2003). Defining P-wave and S-wave stratal surfaces with nine-component VSPs. *The Leading Edge*, 720-729.
- Hardage, B., DeAngelo, M. V., Murray, P., & Sava, D. (2011). *Multicomponent Seismic Technology*. Tulsa, OK: Society of Exploration Geophysicists.
- Helbig, K., & Thomsen, L. (2005). 75-plus years of anisotropy in exploration and reservoir seismics: A historical review of concepts and methods. *Geophysics*, 9-23.
- Horne, S. (2003). Fracture Characterization from Walkaround VSPs. *Geophysical Prospecting*, 493-499.
- Hudson, J. (1981). Wave Speeds and Attenuation of Elastic Waves in Material Containing Cracks. *Geophysical Journal of the Royal Astronomical Society*, 133-150.

- Hustrulid, W. A., & Bullock, R. L. (2001). *Underground Mining Methods: Engineering Fundamentals and International Case Studies*. Society for Mining Metallurgy and Exploration.
- Jenner, E. (2002). Azimuthal AVO: Methodology and Data Examples. *The Leading Edge*, 782-786.
- Kent, D. M. (1984). Depositional Setting of Mississippian Strata in Southeastern Saskatchewan: A Conceptual Model for Hydrocarbon Accumulation. *Oil and Gas in Saskatchewan*, 19-30.
- Lawton, D. (2011). *Seismic Imaging of Complex Geology in Thrust Belts*. GOPH 699.11 Lecture, Calgary.
- Li, X. (1999). Fracture Detection using Azimuthal Variation of P-wave Moveout from Orthogonal Seismic Survey Lines. *Geophysics*, 1193-1201.
- Lines, L. a. (2004). Fundamentals of Geophysical Interpretation. In L. a. Lines, *Geophysical Monograph Series: Number 13* (pp. 201-217). Tulsa, Ok: The Society of Exploration Geophysicists.
- Lodbell, F. K. (1982). Lithology and Depositional Environment of Ashern Formation (Middle Devonian), North Dakota. *66*(5).
- Lynn, H. B., Beckham, W., Simon, K., Bates, C. R., Layman, M., & Jones, M. (1999). P-wave and S-wave azimuthal anisotropy at a naturally fractured gas reservoir, Bluebell-Altamont Field, Utah. *Geophysics*, 1312-1328.
- Lynn, H., Simon, M., Bates, R., & Van Dok, R. (1996). Azimuthal Anisotropy in P-wave 3D (multiazimuth) data). *The Leading Edge*.

- Marfurt, K., Kirlin, R., Farmer, S., & Bahorich, M. (1998). 3-D Seismic Attributes using a Semblance-Based Coherency Algorithm. *Geophysics*, 1150-1165.
- Mavko, G. (2005, 03 26). *Conceptual Overview of Rock and Fluid Factors that Impact Seismic Velocity and Impedance*. Retrieved 11 11, 2012, from Stanford Rock Physics Laboratory:  
<https://pangea.stanford.edu/courses/gp262/Notes/8.SeismicVelocity.pdf>
- McCollum, B., & Snell, F. A. (1932). Asymmetry of Sound Velocity in Stratified Formation. *Journal of Applied Physics*, 72-83.
- Mossop, G. D., & Shetsen, I. (1993). *Geological Atlas of the Western Canada Sedimentary Basin*. Canadian Society of Petroleum Geologists/Alberta Research Council.
- Neves, F., Al-Marzoug, A., Kim, J., & Nebrija, E. (2003). Fracture Characterization of Deep Tight Gas Sands using Azimuthal Velocity and AVO Seismic Data in Saudi Arabia. *The Leading Edge*, 469-475.
- O'Connell, R., & Budiansky, B. (1974). Seismic Velocities in Dry and Saturated Cracked Solids. *Journal of Geophysical Research*, 79(35), 5412-5426.
- Palaz, I., & Marfurt, K. J. (1997). *Carbonate Seismology*. Tulsa, OK: Society of Exploration Geophysicists.
- Park, R. (2005). *Foundations of Structural Geology*. Routledge, Abingdon, England: Chapman & Hill.
- Perez, M., Grechka, V., & Michelena, R. (1999). Fracture Detection in a Carbonate Reservoir using a Variety of Seismic Methods. *Geophysics*, 1266-1276.
- Pickett, G. (1963). Acoustic Character Logs and Their Applications in Formation Evaluation. *Journal of Petroleum Technology*, 659-667.

- Rice, R. B., Allen, S. J., Grant, O. J., Hodgson, R. N., Larson, D. E., Lindsey, J. P., . . .
- Roberts, J. (1981). Developments in Exploration Geophysics: 1975-1980. *Geophysics*, 1088-1099.
- Ricker, N., & Lynn, R. D. (1950). Composite Reflections. *Geophysics*, 30-49.
- Roberts, G., Wombell, R., Gray, D., Al-Shamsi, A., Suwaina, O., Ajlani, G., . . . Al Kaabi, M. (2001). Fracture Orientation Estimation from Azimuthal AVO, Offshore Abu Dhabi. *SEG Annual Meeting Extended Abstracts*.
- Rudzki, M. (1898). Uder die Gestalt Elastischer Wellen in Gesteinen IV Studie aus der Theorie der Erdbebenwellen. *Bulletin of the Academy of Sciences Cracow*, 376-384.
- Ruger, A. (1997). P-wave Reflection Coefficients for Transversely Isotropic Models with Vertical and Horizontal Axis of Symmetry. *Geophysics*, 713-722.
- Sadri, M. a. (2009). NMO correction in anisotropic media using ray velocity. *Geophysical Journal International*, 1781-1786.
- Sandanayake, N., & Bale, R. (2011). Applications of Shear-wave Splitting Analysis to Fracture Characterization for a Shaunavon Tight Oil Reservoir. *CSPG CSEG CWLS Convention Extended Abstracts*.
- Saskatchewan Ministry of Energy and Resources. (2011, January 11). Retrieved September 19, 2012, from Government of Saskatchewan - Energy and Resources:  
[www.er.gov.sk.ca/stratchart](http://www.er.gov.sk.ca/stratchart)
- Sayers, C., & Ebrom, D. (1997). Seismic Traveltime Analysis for Azimuthally Anisotropic Media: Theory and Experiment. *Geophysics*, 1570-1582.

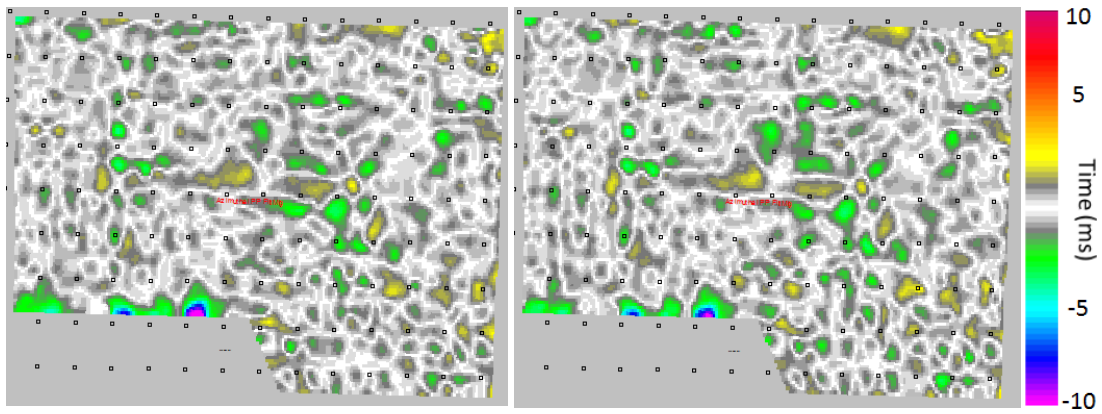
- Shearer, P., & Orcutt, J. (1985). Anisotropy in the Oceanic Lithosphere - Theory and Observations from the Ngendei Seismic Reflection Experiment in the South-West Pacific. *Geophysical Journal of the Royal Astronomical Society*, 493-526.
- Sheriff, R. (2011). *Encyclopedic Dictionary of Applied Geophysics*. Tulsa, OK: Society of Exploration Geophysicists.
- Stewart, R. (2002). Converted-wave seismic exploration: Methods. *Geophysics*, Vol. 67, No. 5, 1348-1363.
- Stewart, R., Gaiser, J., Brown, R. J., & Lawton, D. (2003). Converted-wave Seismic Exploration: Applications. *Geophysics*, 40-57.
- Taner, M., Koehler, F., & Sheriff, R. (1979). Complex Seismic Trace Analysis. *Geophysics*, 1041-1063.
- Tatham, R. (1982). Vp/Vs and Lithology. *Geophysics*, 336-344.
- Tatham, R. H., & Stoffa, P. L. (1976). Vp/Vs - A Potential Hydrocarbon Indicator. *Geophysics*, 837-849.
- Tatham, R., & McCormack, M. D. (1991). *Multicomponent Seismology in Petroleum Exploration*. Tulsa, OK: Society of Exploration Geophysicists.
- Telford, W. G. (1990). *Applied Geophysics - Second Edition*. New York, New York, USA: Cambridge University Press.
- Tessmer, G., & Behle, A. (1988). Common Reflection Point Data-stacking technique for converted waves. *Geophysical Prospecting*, 671-688.
- Thomsen, L. (1986). Weak Elastic Anisotropy. *Geophysics*, 1954-1966.
- Thomsen, L. (2002). *Understanding Seismic Anisotropy in Exploration and Exploitation*. Tulsa, OK: Society of Exploration Geophysicists.

- Tsvankin, I. (1997). Reflection Moveout and Parameter Estimation for Horizontal Transverse Isotropy. *Geophysics*, 614-629.
- Uhrig, L. F., & Van Melle, F. A. (1955). Velocity Anisotropy in Stratified Media. *Geophysics*, 774-779.
- Van Dok, R., & Gaiser, J. (2001). Stratigraphic Description of the Morrow Formation Using Mode-Converted Shear Waves: Interpretation Tools and Techniques for Three Land Surveys. *The Leading Edge*, 1042-1047.
- Vetter, U., & Minster, J.-B. (1981). Pn Velocity Anisotropy in Southern California. *Bulletin of the Seismological Society of America*, 1511-1530.
- Wang, J., & Zheng, Y. (2007). VVAZ vs. AVAZ: Practical Implementation and Comparison of Two Fracture Detection Methods. *SEG Annual Meeting*, 189-193.
- Warren, J. K. (2006). *Evaporites: Sediments, Resources and Hydrocarbons*. Berlin: Springer.
- Waters, K. (1978). *Reflection Seismology*. New York: Wiley and Sons.
- Winterstein, D. & Meadows, M.,. (1991) Shear-Wave Polarization and Subsurface Stress Directions at Lost Hills Field. *Geophysics*. 1331-1348
- Worsley, N. F. (1979). The Potash-bearing Members of the Devonian Prairie Evaporite of Southeastern Saskatchewan, South of the Mining Area. *Economic Geology*, 74, 377-388.
- Yilmaz, O. (2001). *Seismic Data Analysis: Processing, Inversion, and Interpretation of Seismic Data*. Tulsa, OK: Society of Exploration Geophysicists.

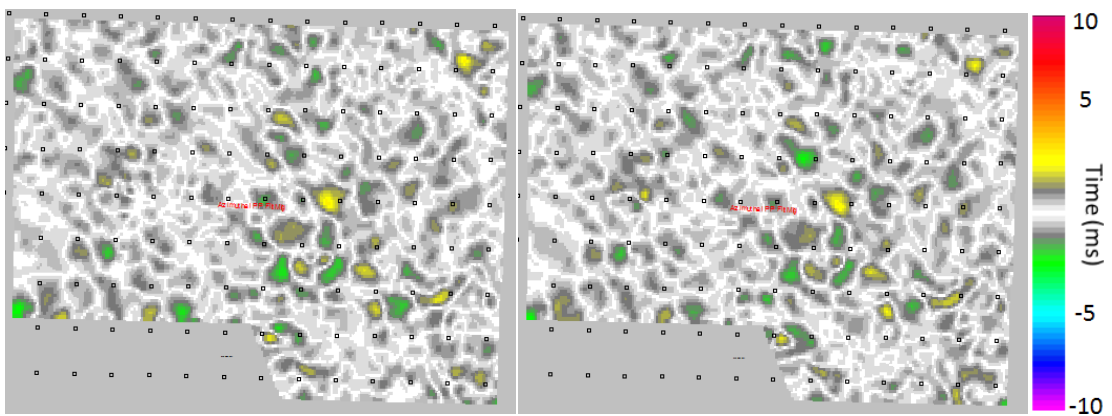
Zhang, Z. (2010). *Assessing attenuation, fractures, and anisotropy using logs, vertical seismic profile, and three-component seismic data: heavy oilfield and potash mining examples*. Calgary: The University of Calgary.

Zheng, Y., Wang, J., & Perz, M. (2008). Pitfalls and Tips for Seismic Fracture Analysis. *SEG Annual Meeting*, 1531-1535.

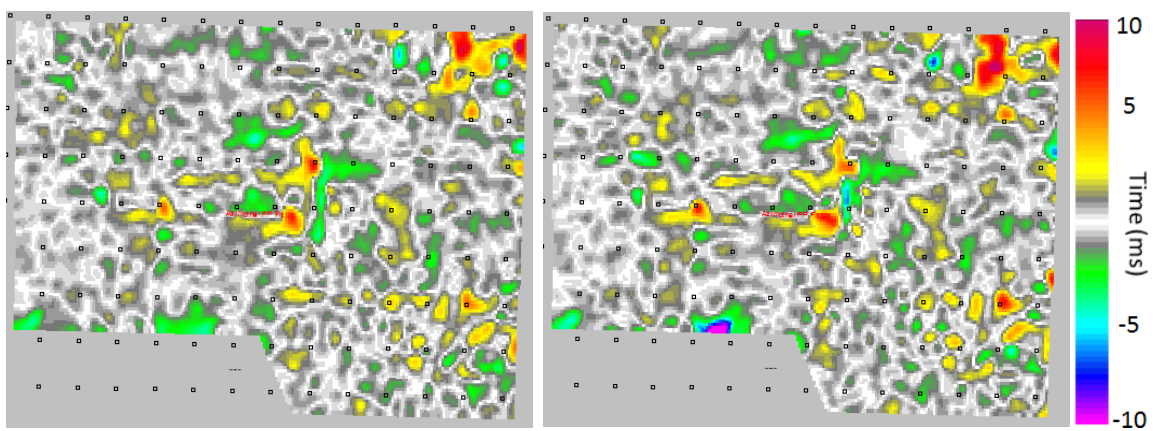
## APPENDIX A: ADDITIONAL RESULTS FOR TRAVEL-TIME ANALYSIS



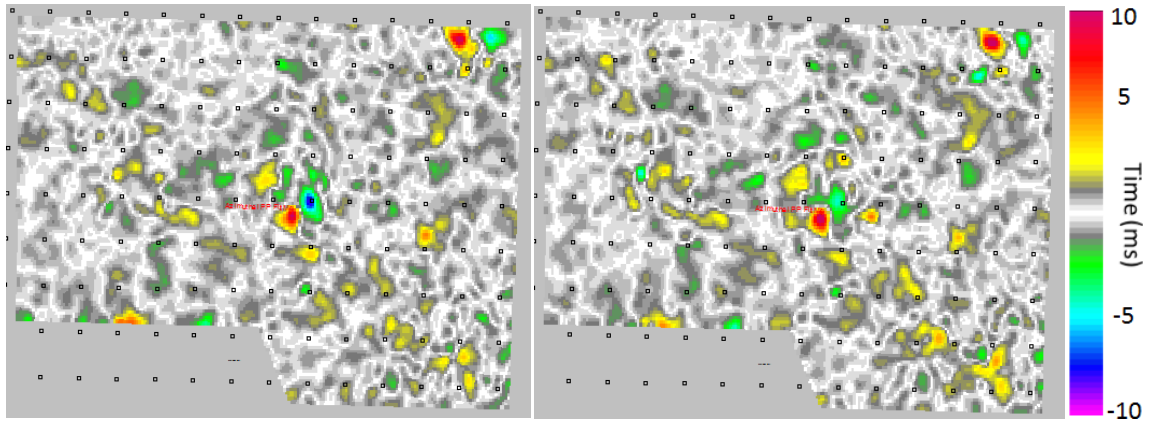
**A. 1 – The baseline (left) and monitor (right) PP, A-C azimuth PP time difference plots for the Birdbear Formation.**



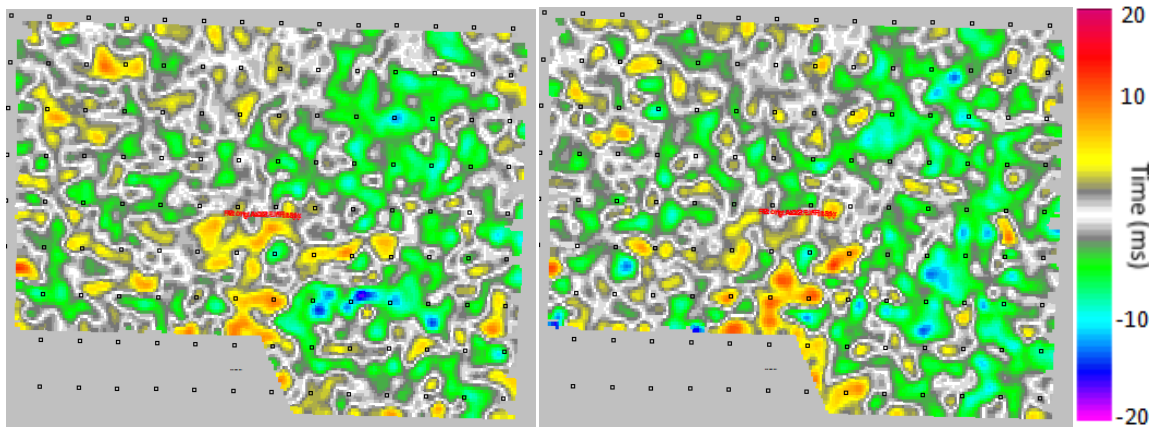
**A. 2 – The baseline (left) and monitor (right) PP, B-D azimuth PP time difference plots for the Birdbear Formation.**



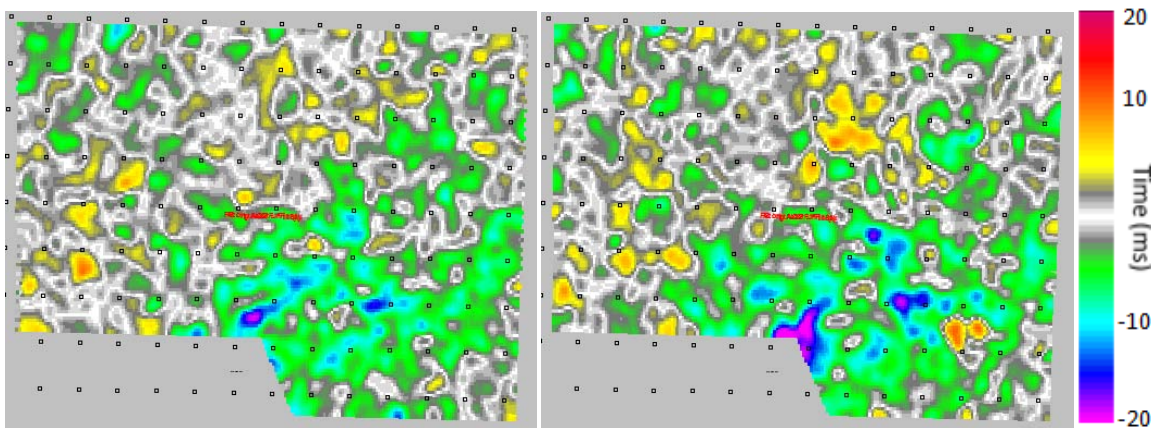
**A. 3 – The baseline (left) and monitor (right) PP, A-C azimuth PP time difference plots for the Dawson Bay Formation.**



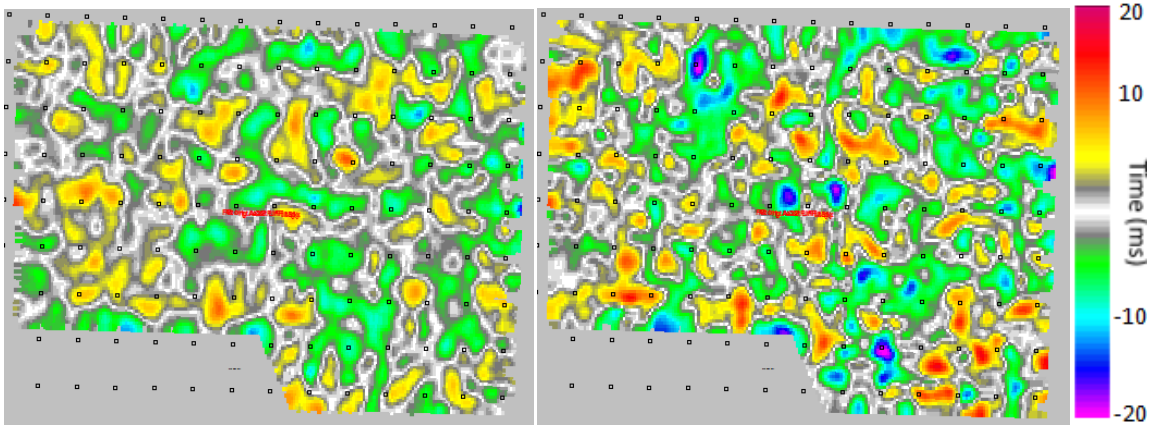
**A. 4 – The baseline (left) and monitor (right) PP, B-D azimuth PP time difference plots for the Dawson Bay Formation.**



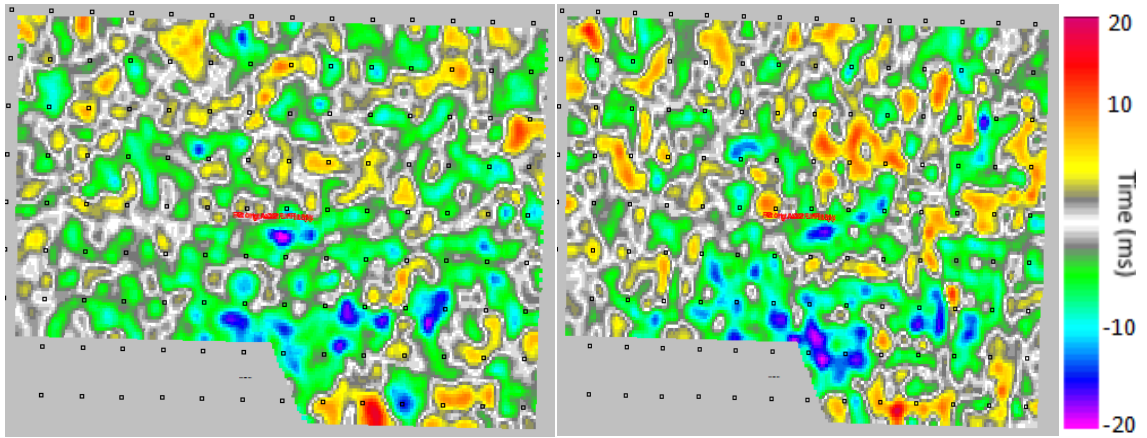
**A. 5 – The baseline (left) and monitor (right) PS, A-C azimuth PS time difference plots for the Birdbear Formation.**



**A. 6 – The baseline (left) and monitor (right) PS, B-D azimuth PS time difference plots for the Birdbear Formation.**



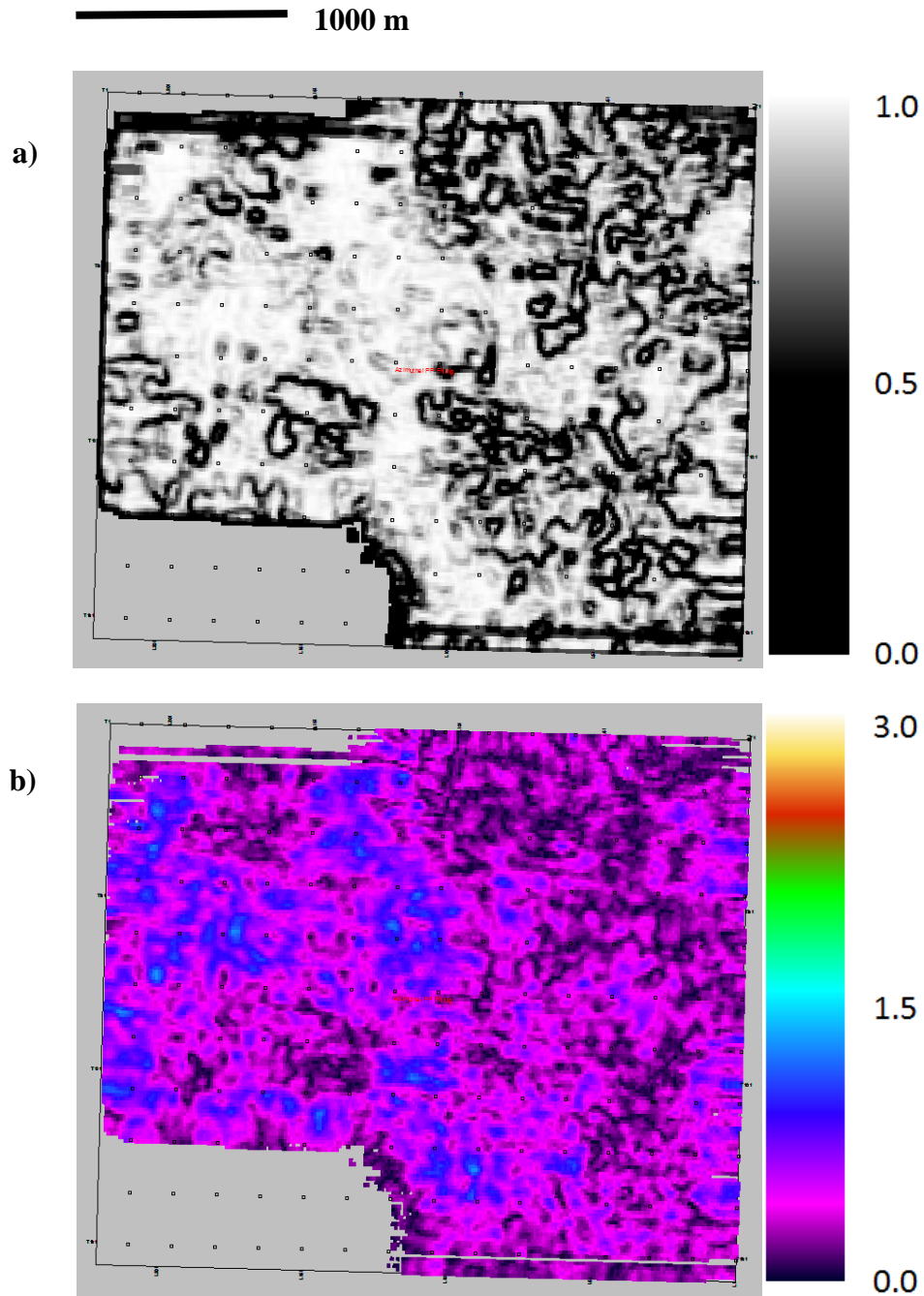
**A. 7 – The baseline (left) and monitor (right) PS, A-C azimuth PS time difference plots for the Dawson Bay Formation.**



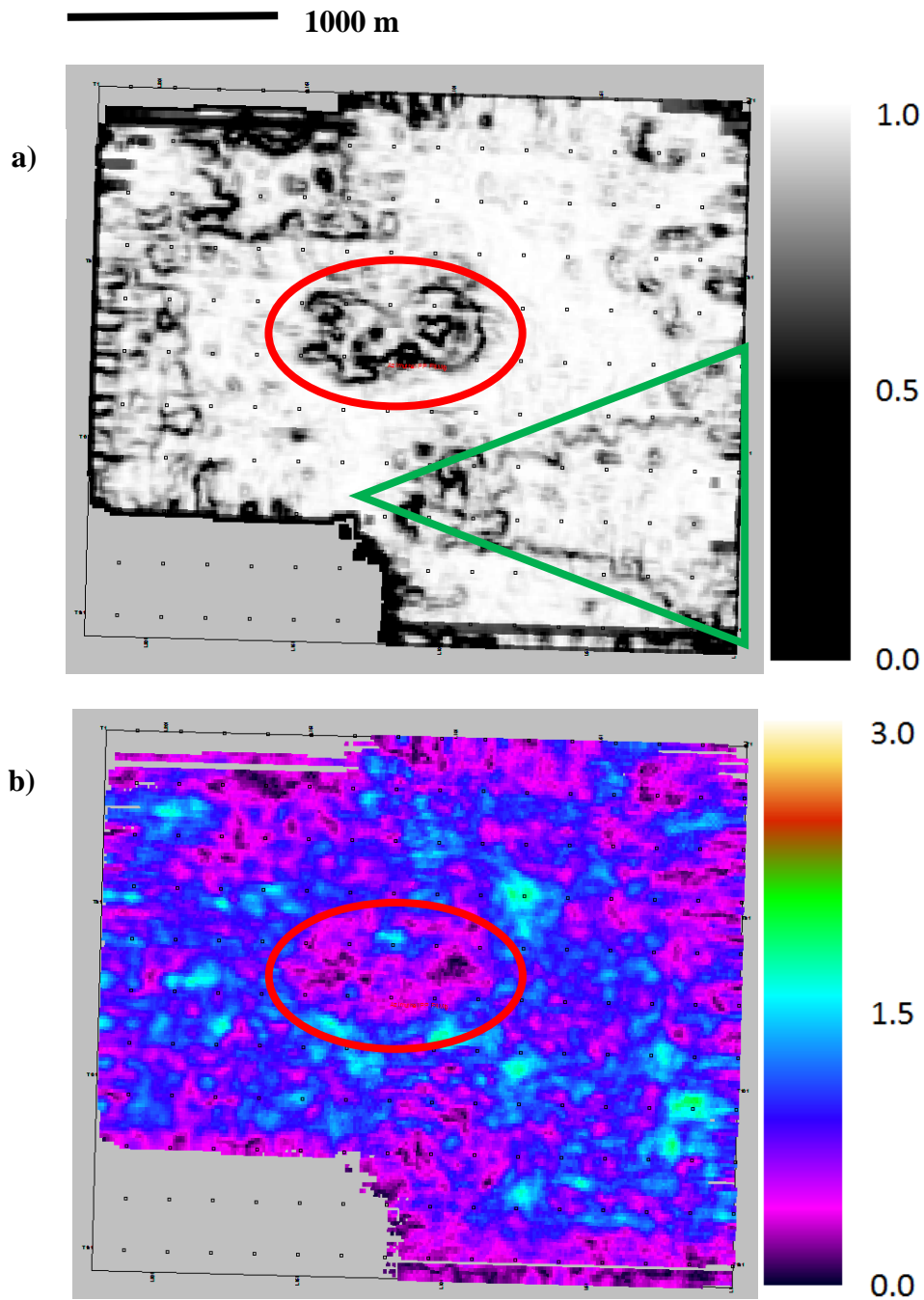
**A. 8 – The baseline (left) and monitor (right) PS, B-D azimuth PS time difference plots for the Dawson Bay Formation.**

## APPENDIX B: ADDITIONAL RESULTS FOR SEISMIC ATTRIBUTE ANALYSIS

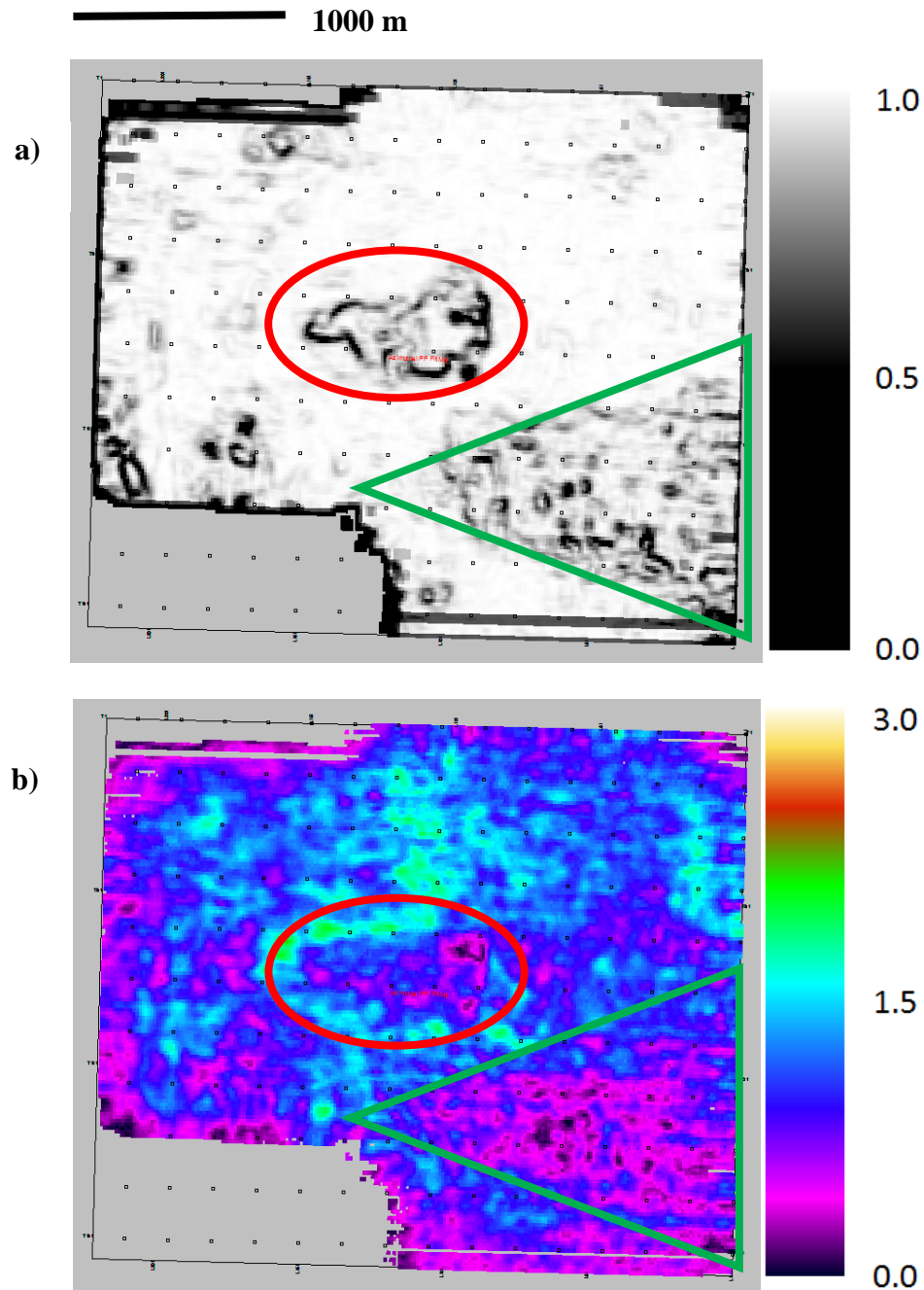
### B.1. Monitor PP Seismic Attribute Interpretation



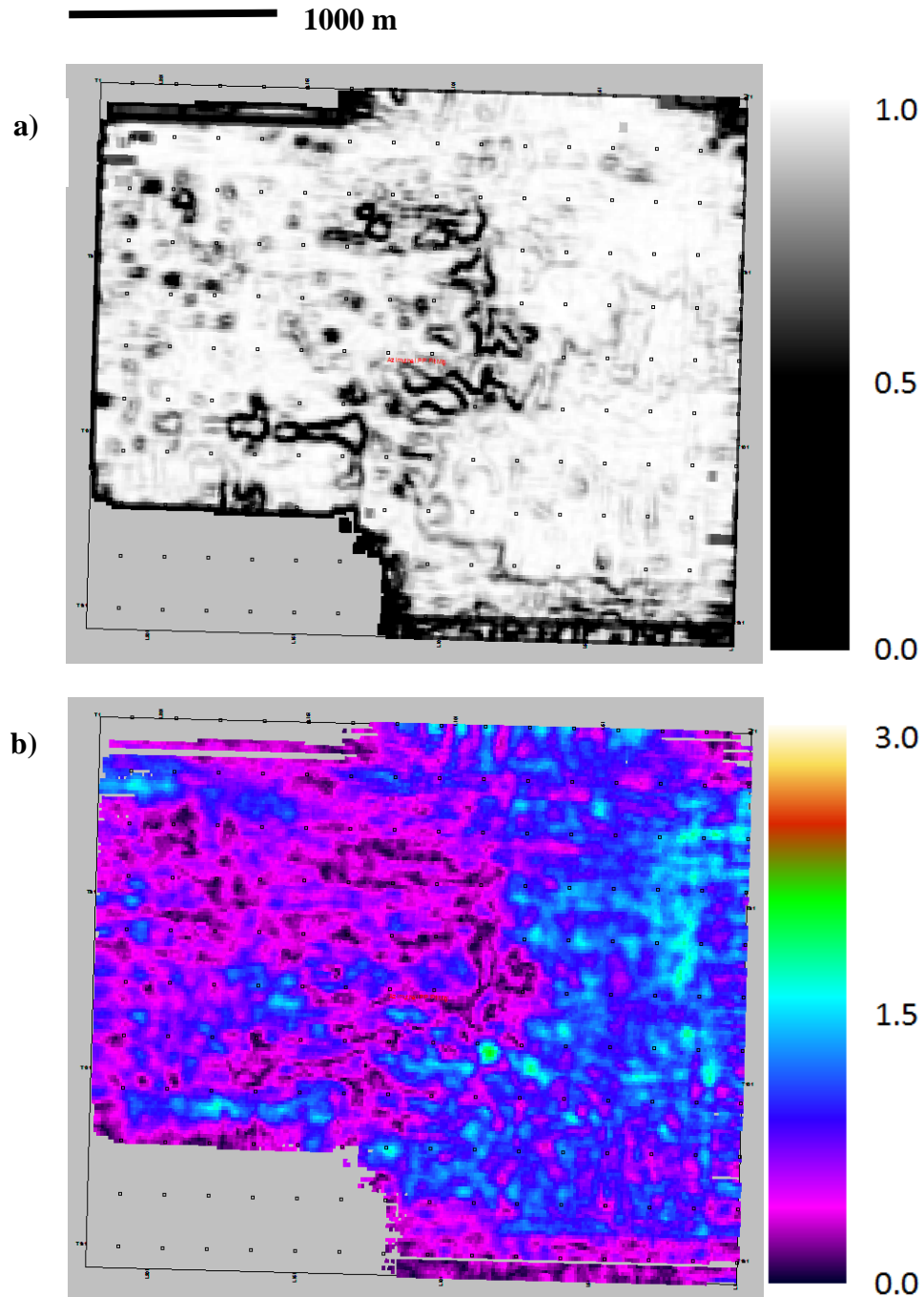
**B. 1 – Monitor PP semblance (a) and amplitude envelope (b) at the top of the Souris River Formation (710 ms).**



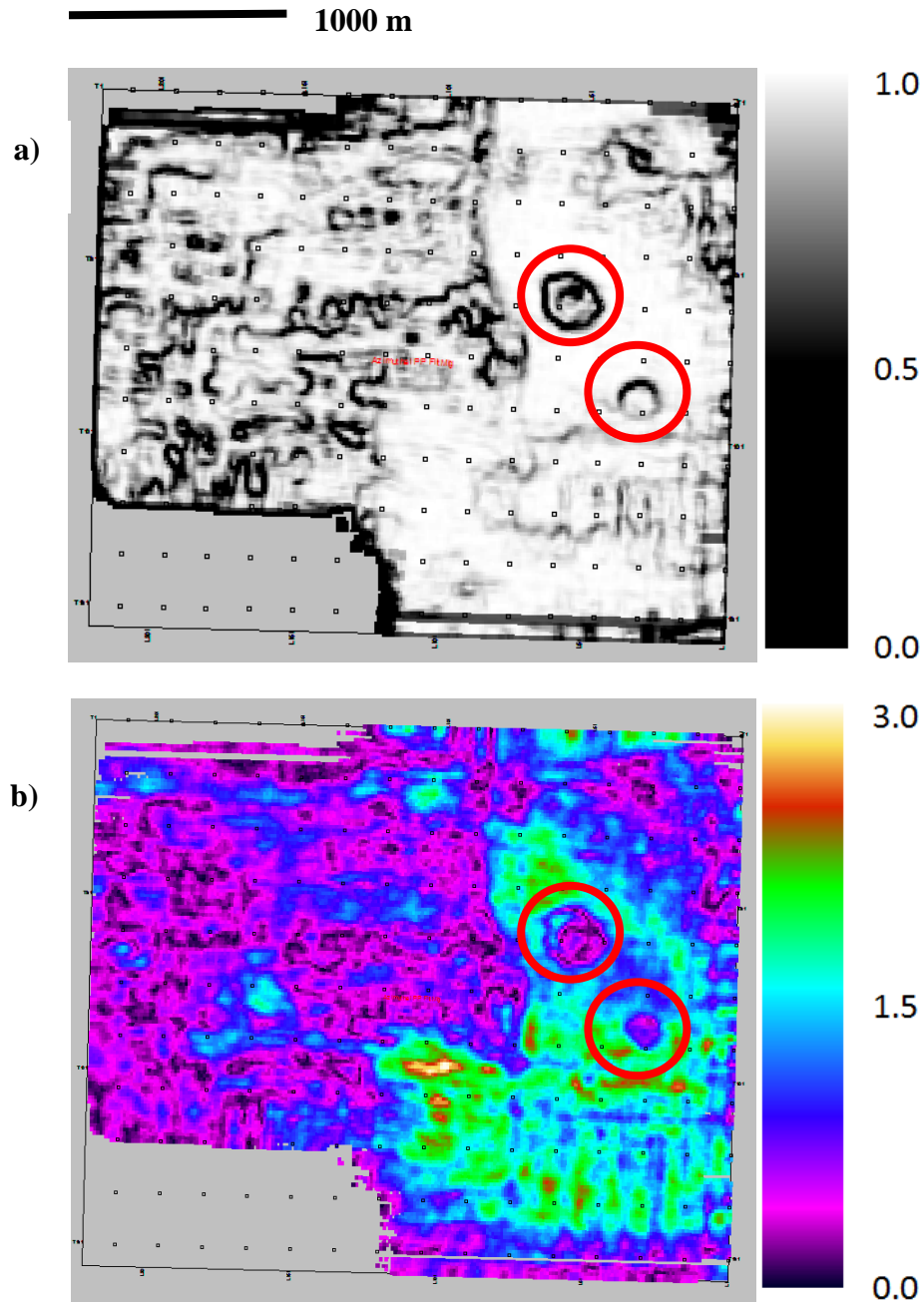
**B. 2 – Monitor PP semblance (a) and amplitude envelope (b) just below the top of the Souris River Formation (720 ms). The red ellipse shows the area where the low amplitude, low velocity anomaly has been interpreted to be located. The green triangle highlights the area where a carbonate mound has been interpreted.**



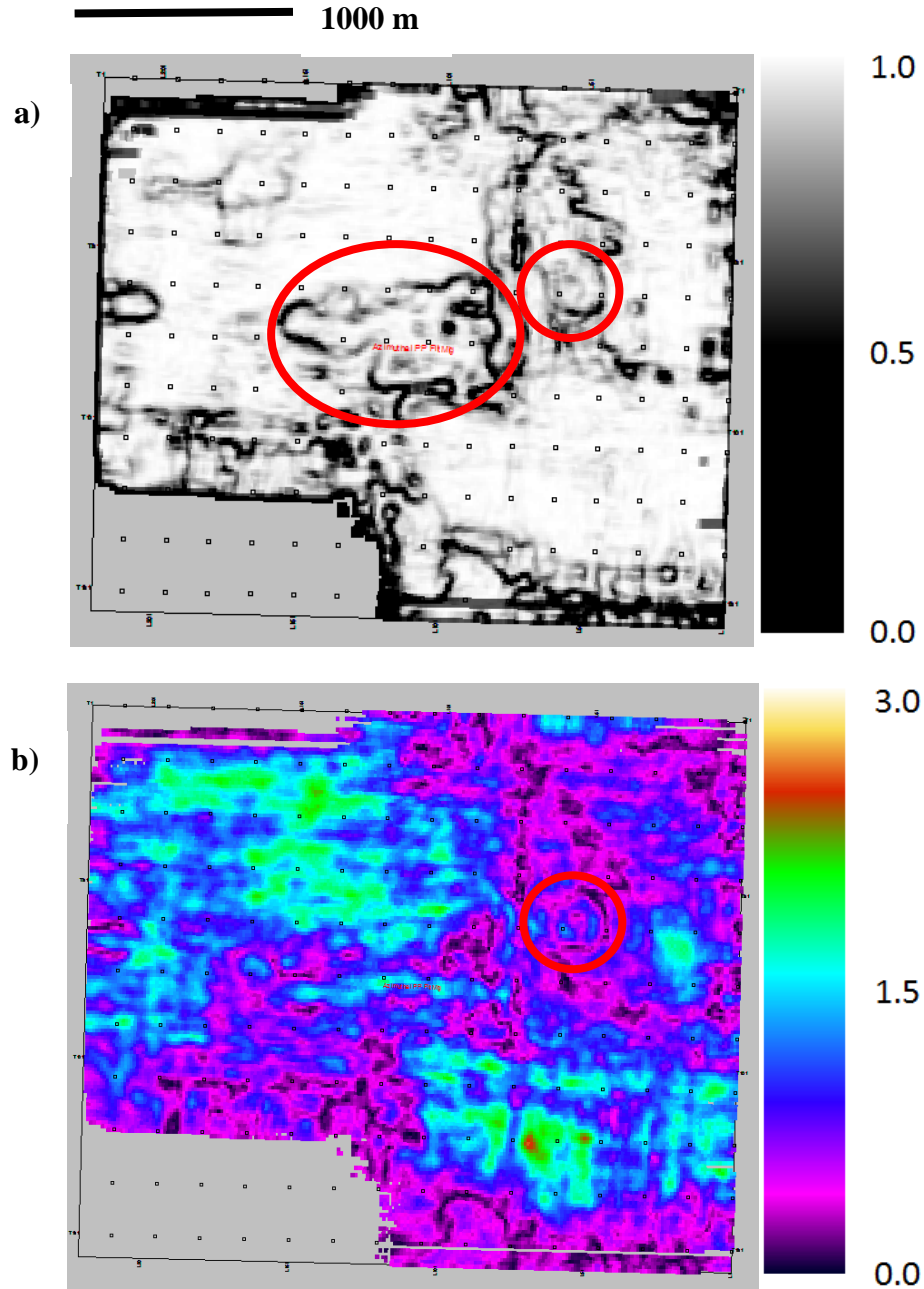
**B. 3 – Monitor PP semblance (a) and amplitude envelope (b) just above the top of the Dawson Bay Formation (748 ms). The semblance and amplitude envelope time slices show anomalies in the area of the low velocity anomaly (red ellipses) and where the carbonate mound is located (green triangle).**



**B. 4 – Monitor PP semblance (a) and amplitude envelope (b) time slices at the top of the Prairie Evaporite Formation (774 ms). No significant anomalies can be seen on either of these slices.**

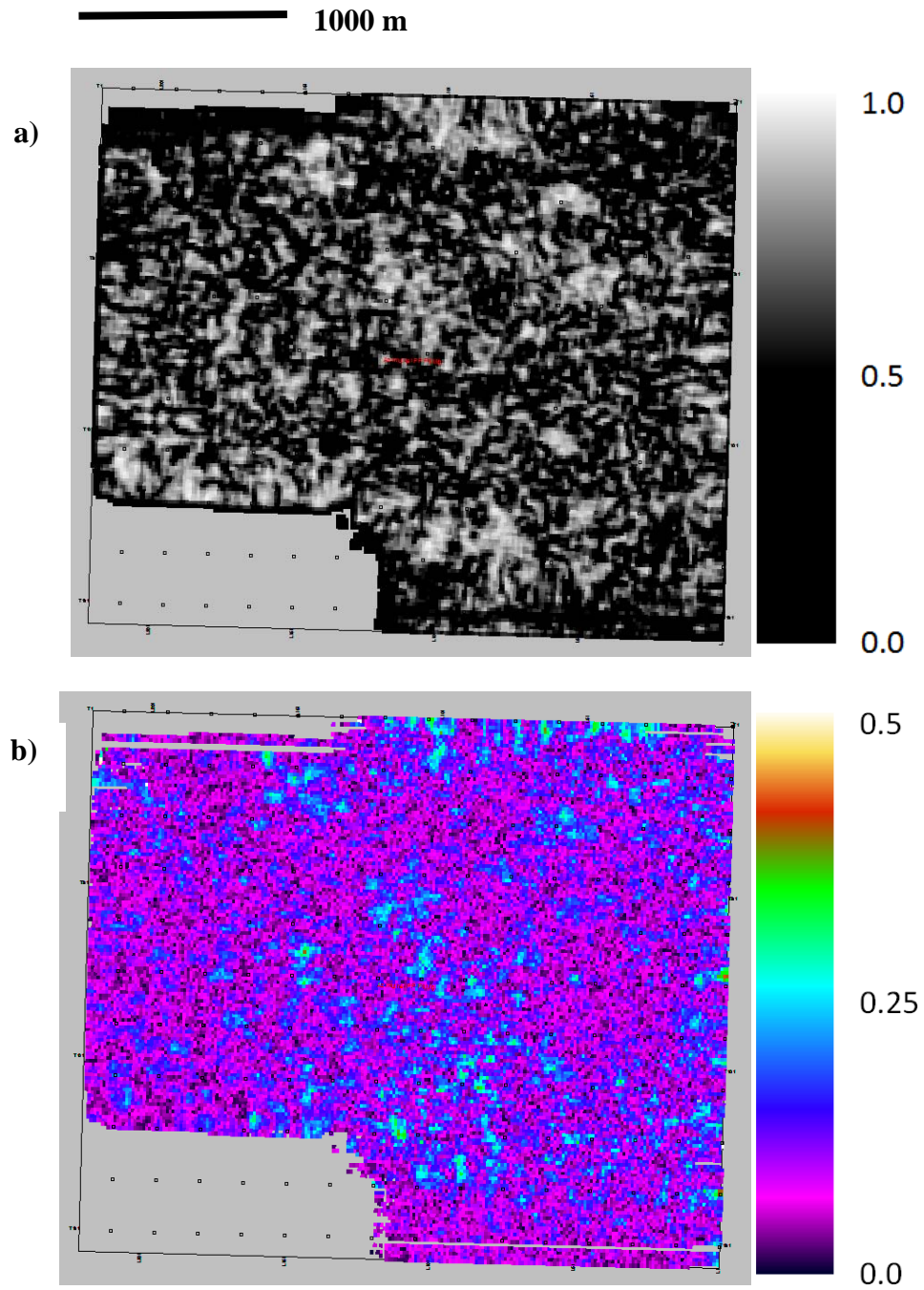


**B. 5 – Monitor PP semblance (a) and amplitude envelope (b) time slices through the Prairie Evaporite Formation (836 ms). The two reef complexes (red circles) are clearly visible in both the semblance and amplitude envelope time slices and the carbonate mound is highlighted in the amplitude envelope time slice with values between 1.0 and 3.0.**

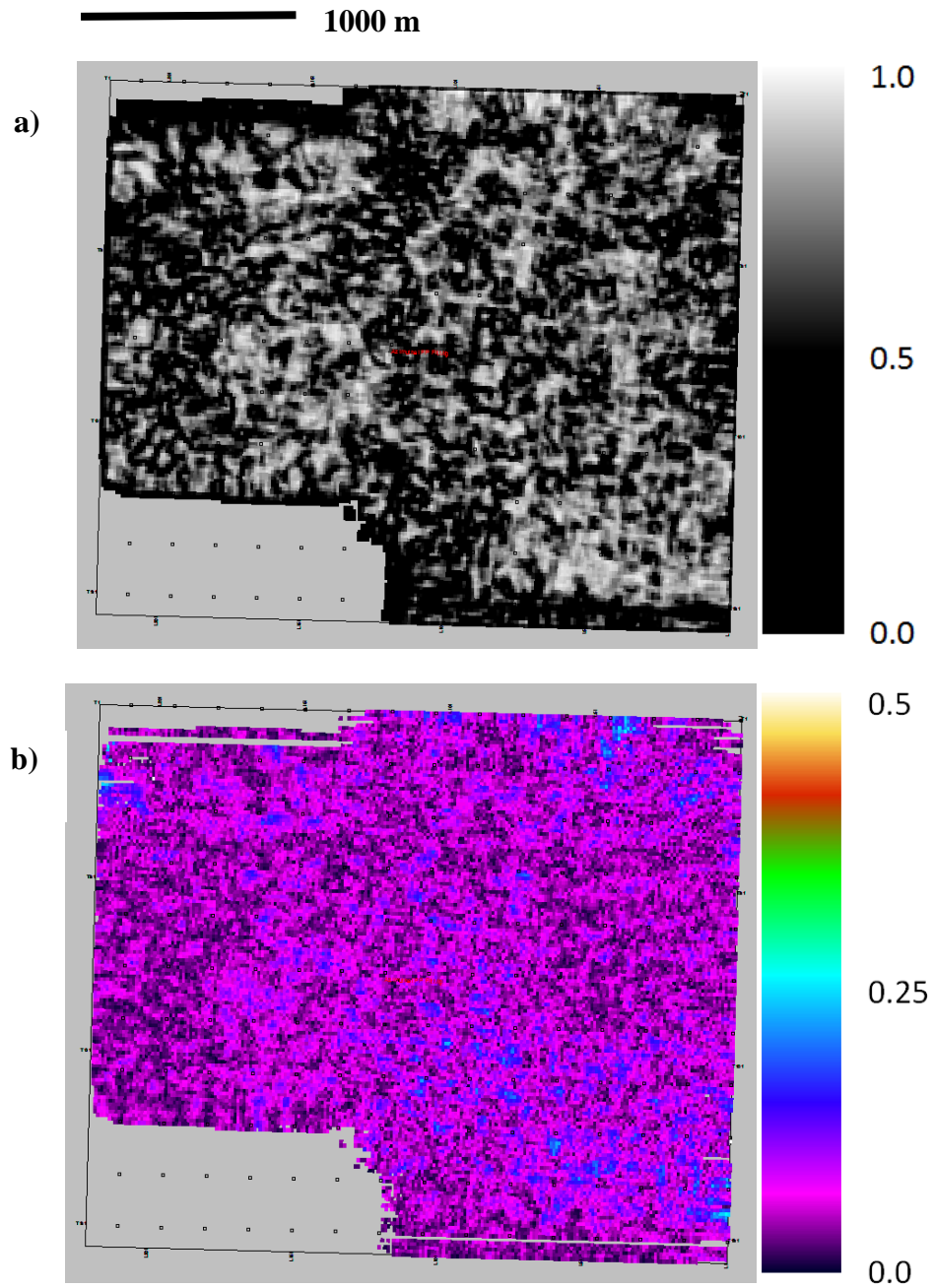


**B. 6 – Monitor PP semblance (a) and amplitude envelope (b) time slices through the top of the Winniepegosis Formation (848 ms). The semblance and amplitude envelope time slices indicate that the northern reef complex is still present at the level, however, the second is not visible. In the semblance time slice, the low amplitude, low velocity anomaly in the centre of the study area is also visible (red ellipse).**

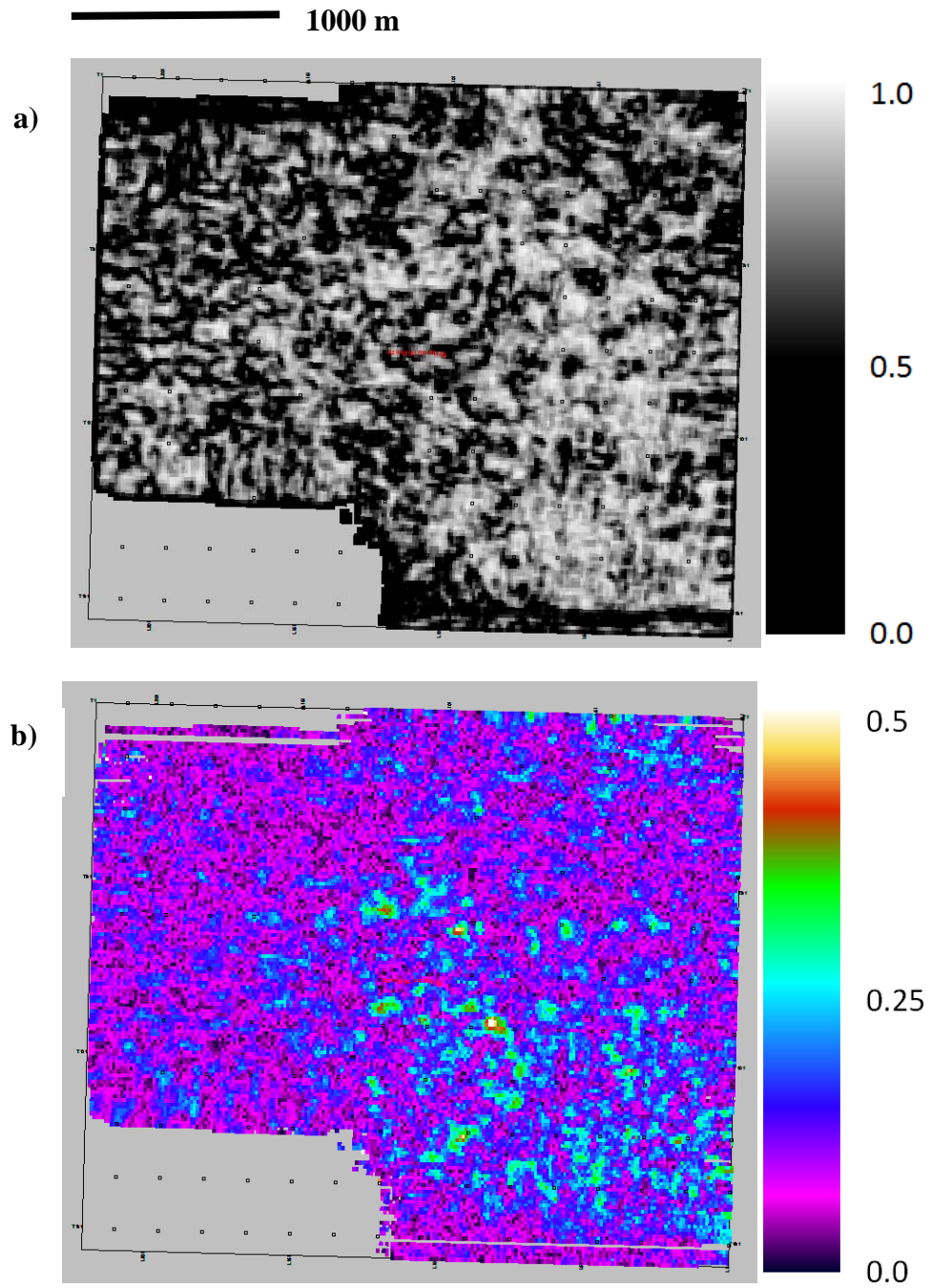
## B.2. Time-Lapse PP Seismic Attribute Difference Analysis



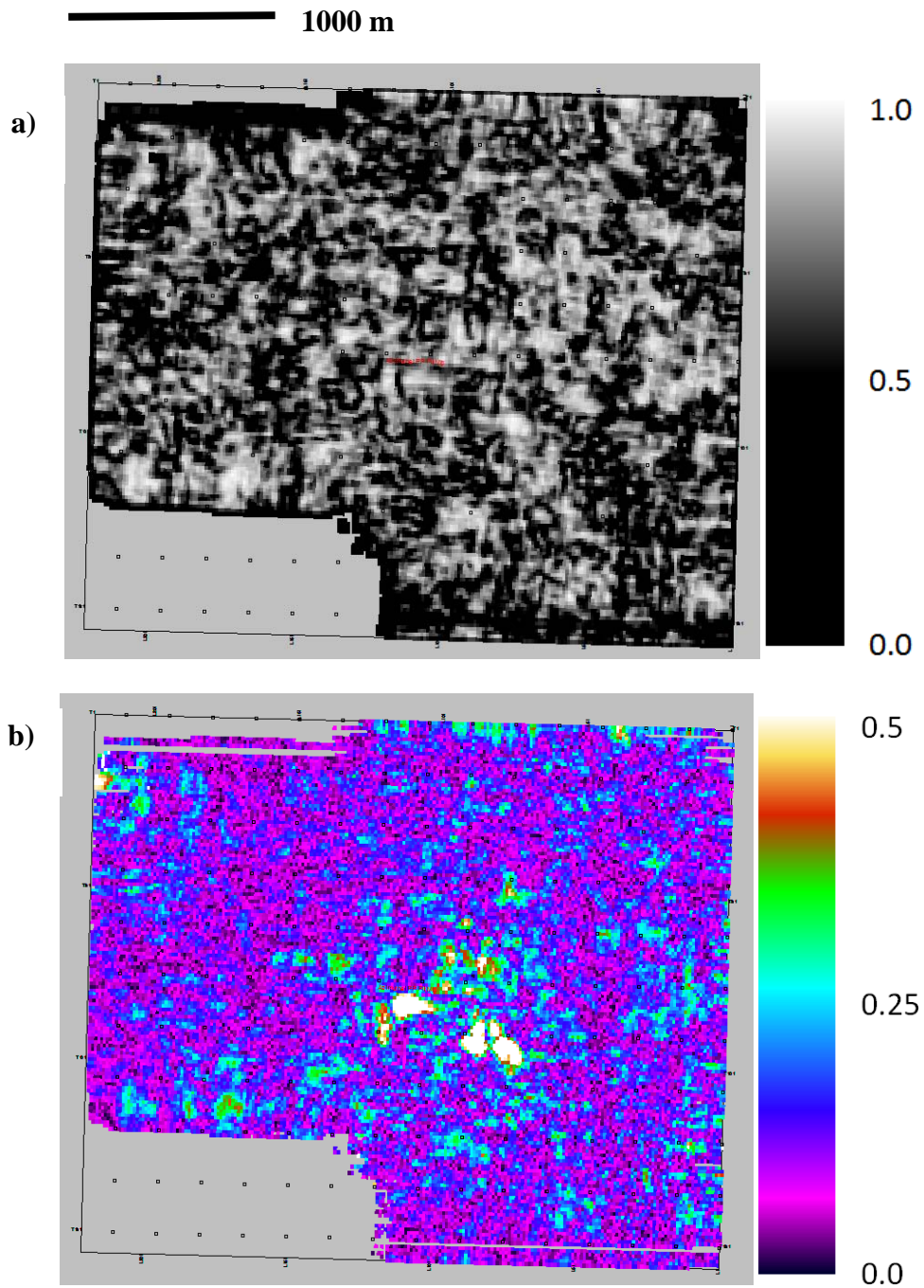
**B. 7 – Semblance (a) and amplitude envelope (b) difference of the PP baseline-monitor surveys at the top of the Souris River Formation (710 ms).**



**B. 8 – Semblance (a) and amplitude envelope (b) difference of the PP baseline-monitor surveys just below the top of the Souris River Formation (720 ms).**

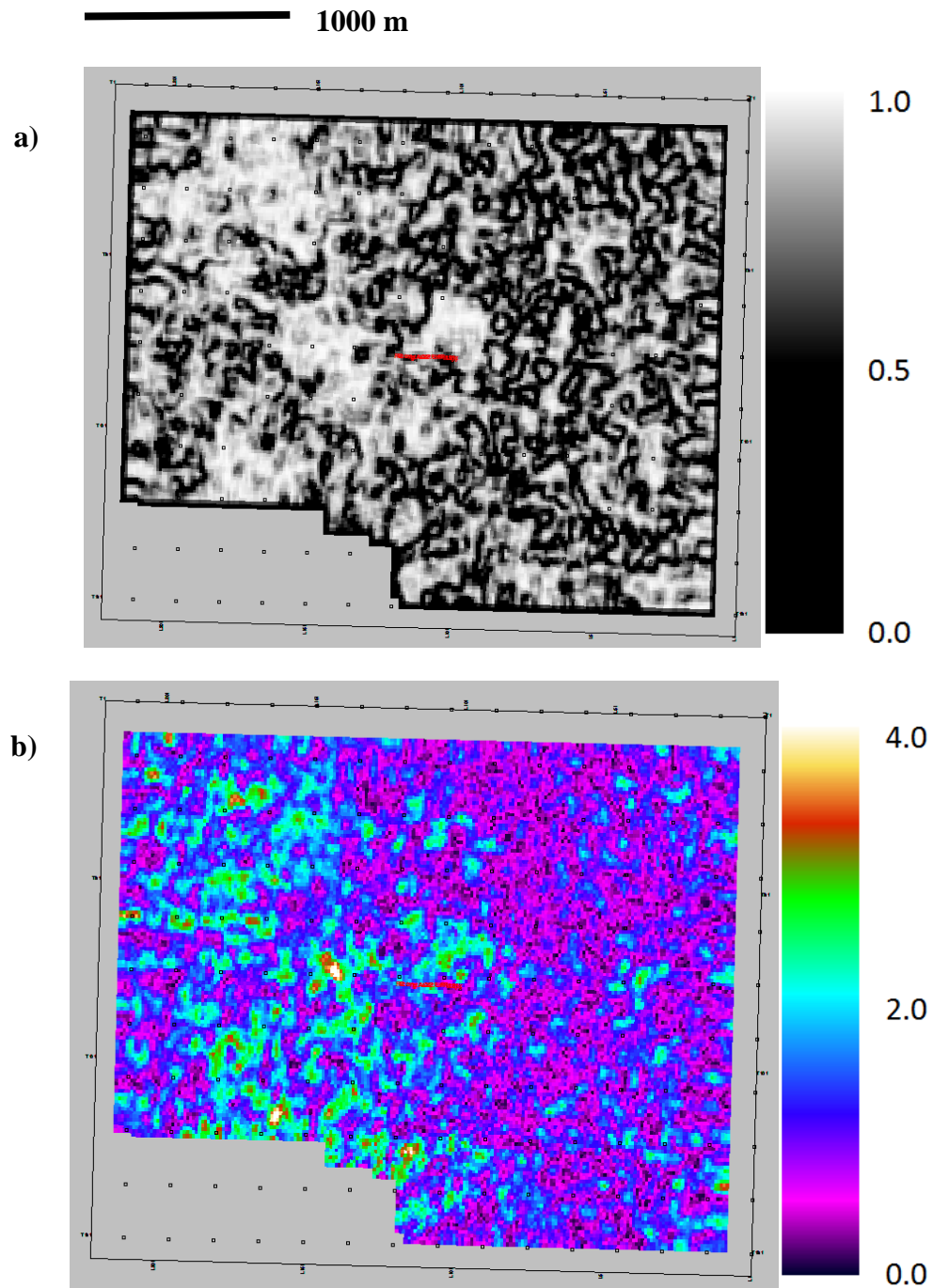


**B. 9 – Semblance (a) and amplitude envelope (b) difference of the PP baseline-monitor surveys at the top of the Dawson Bay Formation (748 ms).**



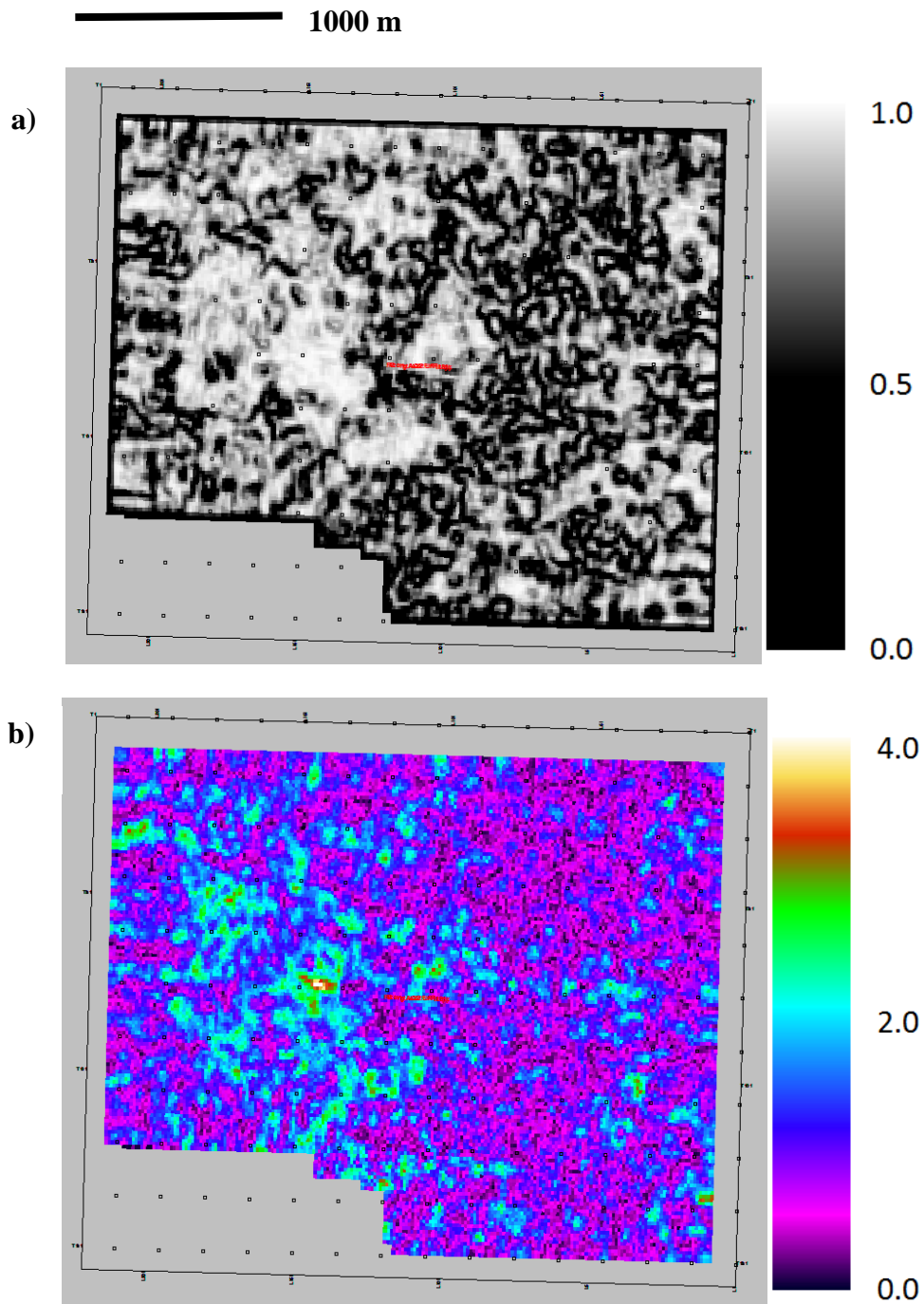
**B. 10 – Semblance (a) and amplitude envelope (b) difference of the PP baseline-monitor surveys at the top of the Prairie Evaporite Formation (774 ms).**

### B.3. Monitor PS Seismic Attribute Interpretation

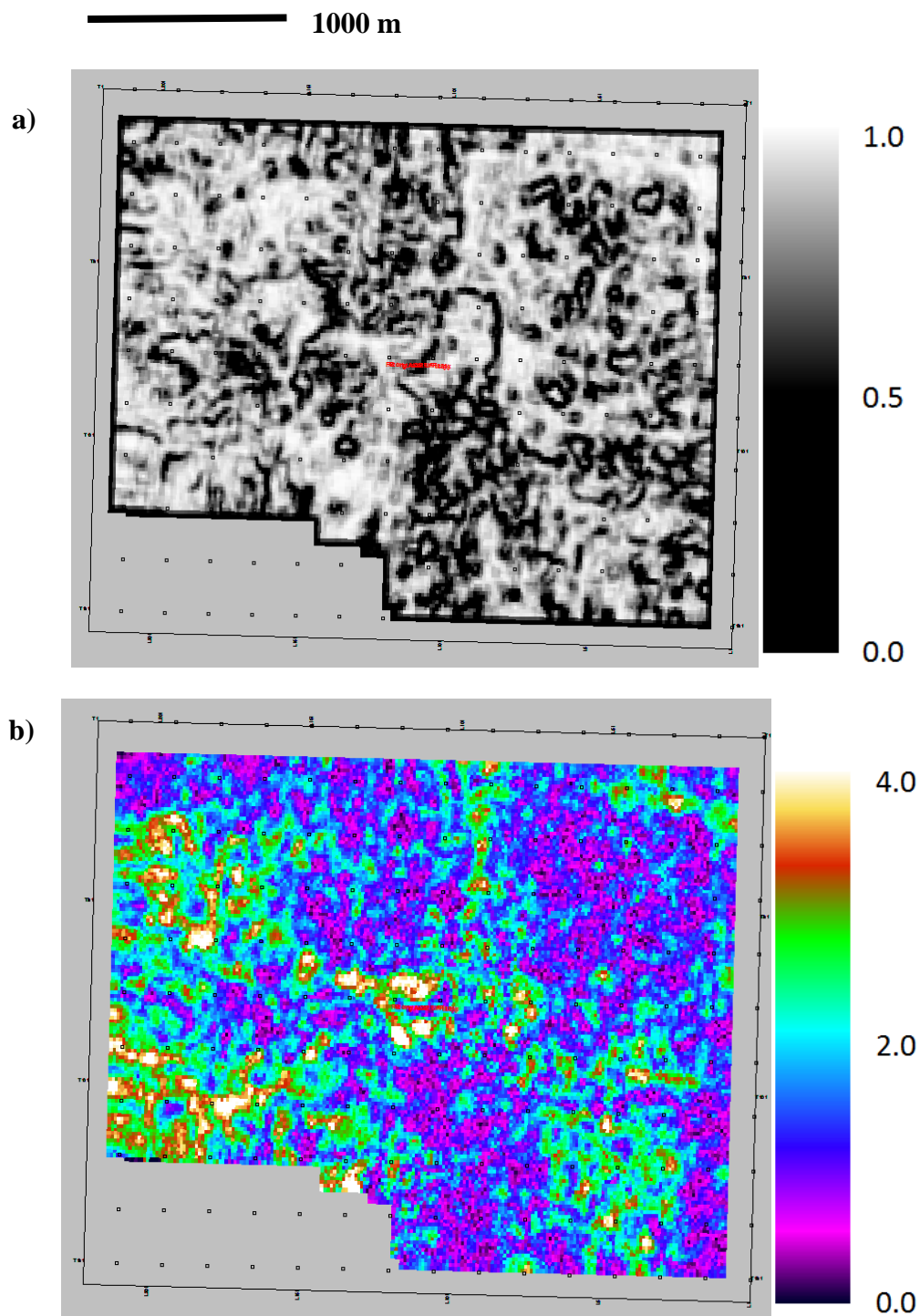


**B. 11 – Monitor PS semblance (a) and amplitude envelope (b) time slices just below the top of the Souris River Formation (1350 ms).**

#### B.4. Time-Lapse PS Seismic Attribute Difference Analysis



**B. 12 – Semblance (a) and amplitude envelope (b) difference of the PS baseline-monitor surveys through the Souris River Formation (1350 ms).**



**B. 13 – Semblance (a) and amplitude envelope (b) difference of the PS baseline-monitor surveys through the Prairie Evaporite Formation (1426 ms).**